Control of Electron and Ion Energy Distributions in Inductively Coupled Plasmas Using Pulsed Power and dc Biases For Fabrication of Microelectronics

by

Michael David Logue

A dissertation submitted in partial fulfillment
of the requirements for the degree of
Doctor of Philosophy
(Electrical Engineering)
in the University of Michigan
2014

Doctoral Committee:

Professor Mark J. Kushner, Chair
Professor Iain D. Boyd
Associate Professor John E. Foster
Professor Brian E. Gilchrist
Associate Professor Pei-Cheng Ku

DEDICATION

This dissertation is dedicated first and foremost to God my father in Heaven and my Lord and Savior Jesus Christ. This thesis, my entire Ph.D. journey, is a testament to God's grace. There were many times I did not think this thesis would be written and many struggles along the way. It has been my faith, love, and trust of God and His grace, mercy, and dedication to me that has seen me through. I also dedicate this document to my mother, Linda Logue, who passed away in my senior year of high school, but always stressed the importance of education and worked so hard to instill in me the values and drive needed to be successful.

ACKNOWLEDGEMENTS

When I got to the University of Michigan in the fall of 2005, I quickly formed a group of friends of fellow graduate students, all of us excited to get our Ph.D. We thought we would be out of here in 5 years and would not really have too many issues. Fast forward 9 years later and I am one of the last to finish, but despite the long and sometimes painful journey, I am finishing. The first acknowledgement must go to God for seeing me through this journey. He has always shown up for me when I was at my lowest. It has been during the process of getting my Ph.D., the hardships I have endured, but also the friendships and personal growth that I have obtained that my faith has been tested and affirmed. I promised God that if He got me through this journey that it would be a testament to Him and that I would acknowledge Him first, which is what I am doing now.

Everything that has happened in getting to this point has all been worth it, because God answered my prayers and connected me with the love of my life, my girlfriend of the past three years and now my fiancée, Alana Maydene Wooley LeBron. Her love and support and its impact on me during the last three years of this journey cannot be measured or overstated. She is my rock and I am blessed beyond all measure to have her in my life.

This work could not have been done without the excellent mentorship and support of my advisor Dr. Mark Kushner. He has been instrumental in my development as a scientist. He is one of the biggest blessings in my life. After my first two advisors did not work out, I truly did not know if I was cut out to get a Ph.D. and my confidence in myself was at an all-time low. Through the mentorship and support of Dr. Kushner my outlook on my path and myself as a

researcher and as a person has grown tremendously. He is a teacher. It is not just in his job title but it is part of who he is as a person. He has taught me so much during my time with him. His work ethic and professionalism are truly inspirational and he is readily available for advice. I will be forever grateful for his presence in my life.

I also have been blessed to have an incredibly supportive family that has encouraged my learning and fostered in me the belief that I could achieve anything I put my mind to. There are too many family members to name them all but I do want to acknowledge a few specifically. I want to acknowledge my mother, Linda Logue, who passed away before she could see me get this degree but who will always be with me in spirit. There is nothing like a mother's love, and I can truly say that my mother's love for me was probably bigger than even I realized but she did her best to show me every day. It was truly a blessing to have her in my life. My father, Samuel Logue, has always had absolute faith in me and I could not be the man I am today without his love, support, and guidance. If I really need his support, I can always count on him to have my back. I am incredibly lucky to have him in my life.

My sister, Dr. Melissa Logue, has always been a source of inspiration to me. She is and always will be the first Dr. Logue. She has supported me and protected me in ways I will forever be grateful for. She has taken on the protective mother role after my mother passed away and she is one of the most important people in my life. I also would like to thank my cousin Clinton Johnson for being like a brother to me and sharing a passion for science and technology with me. He has been a sounding board and a source of guidance and support that has helped me to grow tremendously. I would also like to acknowledge Rev. Yolanda Whiten and the rest of the Whiten family that have become like a second family here in Michigan. They have supported me tremendously and I am truly blessed God put them in my life.

I want to thank my dissertation committee: Professor Brian Gilchrist, Professor John Foster, Professor Pei-Cheng Ku, and Professor Iain Boyd for agreeing to serve on my committee and providing valuable feedback on my work. I would also like to thank my collaborators at the University of Houston, in particular Professor Demetre Economou, Professor Vincent Donnelly, Hyungjoo Shin, and Weiye Zhu, whose work has been a source of validation for much of the results and insights presented in this dissertation. The experimental work and images in chapters 4 and 6 come from them. I would like to thank my funding sources: the Department of Energy Office of Fusion Energy Science, the Semiconductor Research Corporation, and the National Science Foundation. I would also like to thank my professor's at Villanova: Dr. Robert Caverly, Dr. Pritpal Singh, Dr. Frank Mercede, and Professor Edward Dougherty that supported me during both my time there and here at Michigan. When I was having trouble here at Michigan I contacted them for advice and they were incredibly supportive. They helped me to decide to stay at Michigan for my Ph.D. and I am incredibly grateful to them. I also want to thank the administrative staff here at Michigan, in particular Beth Stalnaker, Julia Falkovitch-Chain, and Michelle Chapman and the staff at Villanova that kept me in the loop about things happening on campus, and helped me to navigate all of the administrative hurdles that go on behind the scenes but that have to be done.

The friendships I have cultivated during my time in Michigan are things that I will treasure for a lifetime. Before coming here, I had friendships but none at the truly deep, life-long level that I found here. These friendships have sustained me during my time at Michigan and been an incredible source of growth for me personally. I was very introverted, at least to my peers, before coming here. My friendships have helped develop me into the man I am today. In

particular my bible study group, the Men of Valor or MOV, has been an incredible support network and source of personal growth for me.

I am also extremely grateful to my current and former labmates: Yang Yang, Juline Shoeb, Mingmei Wang, Seth Norberg, Sang-Heon Song, Peng Tian, Wei Tian, Yiting Zhang, Dr. Zhongmin Xiong and Dr. Natalia Babaeva for being such a supportive group both professionally and personally. I also would not have joined my advisor's group without the advice of Professor Herbert Winful here at Michigan and I am very grateful to him.

TABLE OF CONTENTS

LIST OF FIGURES

ABSTRACT

In order to meet present and upcoming challenges to reduce feature sizes below 22 nm, advanced plasma etching techniques are required, necessitating tighter control over plasma properties and etch characteristics. Better control of the electron energy distribution (EED) and the ion energy distribution (IED) are two ways to achieve this goal. The EED controls plasma properties such as electron temperature (T_e) and plasma density, as well as the rates of electron impact reactions that generate reactive species from feedstock gasses. Ions enable very directional etches with near vertical sidewall profiles. Ions are accelerated vertically toward the substrate through sheaths. The greater the potential drop across the sheath, the greater the ion acceleration and the greater the energy with which it bombards a substrate. IED control is an important factor in controlling etch profiles and reducing plasma induced damage.

Two potential methods to control EEDs and IEDs in inductively coupled plasmas (ICPs) are discussed using results from a 2-D hybrid model, the Hybrid Plasma Equipment Model (HPEM). These methods involve the use of pulsed ICP power and dc biases on electrodes in contact with the plasma. Modifications are made to the HPEM to enable more accurate EED calculations in systems with multiple ICP sources as well as more accurate IED calculations in systems with pulsed ICPs and/or pulsed dc biases. Pulsed plasmas provide a way to obtain EEDs on a temporal as well as a time averaged basis that might not be accessible with continuous wave (cw) excitation. The shape of the EED controls the rates of generation (source functions) of reactive species in the gas phase, which impacts wafer etch performance. The use of pulsed power in an ICP in Ar/N_2 gas to control EEDs and source functions is discussed. The single step

electron impact source functions of three plasma species: $N_2(v = 1)$, $N_2(A)$, and Ar^+, with threshold energies of 1.3, 6.17, and 16 eV, respectively, are chosen to represent low, mid, and high threshold energy processes. Pulsing of the ICP power modulates the tail of the EED by lifting the tail in the activeglow and lowering the tail in the afterglow. This significantly modulates the source functions for $N_2(A)$ and Ar^+ over the pulse period.

The use of dc biases shifts the plasma potential with respect to ground or changes the potential dropped across the substrate sheath, in order to control substrate IEDs. In ICPs, plasma generation comes from the ICP. Ion acceleration can be controlled by an applied bias on the substrate or a boundary electrode (BE). That is the basis for the boundary electrode ICP system (BE-ICP). The use of a dc bias on a BE at the top of a cylindrical ICP, operated in cw and pulsed formats, to control IEDs to a grounded substrate is discussed.

Applying a positive dc bias shifts the plasma potential and thus the peaks in the IED by approximately the applied bias. Applying the dc bias in the afterglow of a pulsed ICP enables the narrow afterglow IED peak to be shifted to an energy determined by the bias. A narrow IED peak is desirable because it allows for increased etch selectivity between materials that have similar ion threshold energies for etching.

The etch rate for most ion assisted etching processes generally increases with increasing ion bombardment energy but comes at the cost of increased plasma induced damage to the substrate. This damage is typically greater and less easy to repair for heavier ions, which are closer in mass to the substrate atoms. Lighter ions have shorter sheath transit times and thus are accelerated to higher energies faster than heavier ions. Accelerating lighter ions to higher energies than heavier ions could ideally reduce the impact of plasma induced damage, while still maintaining high throughput.

An investigation into the use of short dc bias pulses on the substrate in a planar ICP, with a pulse on period between the sheath transit time of a pair of heavy and light ions is discussed. Most etching gas mixtures contain multiple ionic species. As such, Ar/H_2 and Xe/H_2 are used because these systems contain multiple ionic species, with large mass differences between the heaviest and lightest ions. If the pulse on period of the pulsed dc bias is between the sheath transit times of the heaviest and lightest ions in the system, then the heavier ions are not able to convert the full sheath potential during the bias on period into kinetic energy for ion bombardment. This is reflected as an energy separation in the IED peak during the bias on period, referred to as the selectivity between a pair of ions, for the lightest and heaviest ions.

Remote and tandem systems have the benefit of decoupling control of the EED in a primary system from control of the operating conditions of that system. This has the potential to allow for greatly enhanced customization of the EED. The ability of a tandem ICP system, with a biasable BE on the top and a grounded grid separating the two ICPs, to control EEDs in the lower ICP is discussed. When the lower ICP is pulsed with the top ICP on in cw format, the tail of the EED in the lower ICP region is lifted in the afterglow and T_e increases. The flux of high energy electrons from the upper ICP increases the average electron energy in the lower ICP, thereby lifting the tail of the EED and increasing the electron temperature. This effect is enhanced if a large positive bias is applied to the BE under these conditions.

Chapter 1 Introduction

Plasmas play a key role in the fabrication of microelectronics.[1] Plasmas are used extensively in the semiconductor manufacturing industry for processes such as plasma material etching, deposition, and stripping of photoresist. Plasma etching has allowed for patterns to be transferred from a mask to a substrate accurately and with small deviation from the pattern critical dimensions. This has enabled microelectronics to be fabricated with smaller feature sizes. As the desired feature sizes for future microelectronics shrinks below 22nm, control of plasma characteristics becomes increasingly important.[2] Control of these plasma characteristics depend largely on control of the kinetics of the plasma.

There are several methods used to control plasma kinetics, including pulsed power and biases on electrodes in contact with the plasma.[2] These methods are used to control, among other things, the electron energy distribution (EED) as well as the ion energy distribution (IED) in the plasma and at the substrate. Electrode biases can affect bulk plasma properties in cases where the bias power is comparable to or greater than the source power. Since there are many process parameters, such as power, pressure, flow rate, gas chemistry, excitation frequency, etc., that can be used to control the EED and IED, experimental investigations of the effect different operating conditions have on the EED and IED could be costly and time consuming. Computational modeling is a method by which these investigations can be performed, ideally on a less expensive and more efficient basis. Modeling also allows for the comparison with experiments and the investigation of mechanisms that could potentially explain observed behavior.

In this thesis, results of computational investigations in the control of the EED and IED in inductively coupled plasmas (ICPs) using pulsed ICP power and dc biases are discussed. The investigations of this thesis are designed to develop insights and scaling laws to improve plasma processing applications such as plasma etching. There are four major research contributions of this thesis. First, this thesis provides insights into how the threshold energy of a process impacts the ability of pulsing to in turn affect the reaction rate of that process. Second, this thesis contributes to the understanding of how the EED and source functions can vary spatially with pulsing on both a temporal and time averaged basis. Having this understanding can lead to more optimally designed systems for better etch characteristics such as etch uniformity for example. Third, the investigation of the use of dc biases in ICPs to control IEDs is also a major contribution of this thesis. With validation from experiments it is shown that dc biases on boundary electrodes allow the ion energy and the ion flux, determined largely by the plasma density, to be controlled largely independently. This has the potential to lead to better control the rate of etching versus deposition on a wafer as well as enhanced selectivity when etching. Fourth, the work of this thesis contributes to the understanding of the ability of tandem source systems to achieve EED customization. Tandem sources are a promising area of research in the drive to customize the EED in a plasma etch process.

In this chapter a brief general overview of plasmas and plasma etching is given. Control of plasma kinetics, specifically the EED and IED, in the context of improving plasma etch processes and the use of computational modeling as a means to investigate this control are also discussed.

1.1 Plasmas in Our World

Plasmas are ionized gases containing neutral species, free electrons, and positive and negative ions, which on the average are electrically neutral. Plasmas can either be fully or partially ionized. In partially ionized plasma, the density ratio of charged particles to the total density of atoms and molecules is less than 1. Plasmas can also operate in local thermodynamic equilibrium (LTE) or non-LTE conditions. In non-LTE plasmas, the temperature of electrons (T_e) is much higher than the temperature of ions (T_i), which is higher than the temperature of the neutral background gas (T_{gas}). In LTE plasmas, collisional processes are the dominant processes which govern transitions and reactions in the plasma as opposed to radiative processes.[3] There must be a detailed balance between each forward and reverse collisional process. Further, the local gradients of plasma properties (e.g., temperature, density) must be sufficiently small that the diffusion time of a particle is much greater than its equilibration time.[3] These conditions lead to the temperatures of electrons, ions, and neutral species in the plasma being in equilibrium locally around a specific position in the plasma.[3] The equilibrium temperature can vary spatially in the plasma.[3]

Plasmas can be bounded or unbounded. Bounded plasmas are plasmas confined in containers in which the plasma interacts with the walls of the container through transition regions called sheaths. Unbounded plasmas are not confined in these containers. In bounded plasma there is a faster rate of loss of electrons compared to ions to the bounding wall surfaces of the plasma due to the differences in their thermal speeds. This creates a thin, positively charged layer at the boundaries of the plasma, called the sheath, which acts as a transition region between the plasma and wall surfaces. As more electrons are depleted near the boundary of the plasma and as the sheath width expands, the positive space charge creates an electric field pointing

toward the walls bounding the plasma. This electric field increases the flux of ions to the walls while decreasing the flux of electrons. Eventually the sheath width reaches an equilibrium point where the electric field created from the positive charge in the sheath is large enough to balance the flux of ions and electrons to the walls.

Many consider plasmas as a fourth state of matter.[1] They can be created naturally or artificially. When matter changes temperature it can undergo a change of state, changing from a solid at very low temperatures to a plasma at very high temperatures. Very high and very low are relative in this case, as the temperature required for a change of state is material dependent. Most visible matter in the universe, which includes matter like stars, exists in a plasma state and are naturally occurring plasma in thermal equilibrium conditions.[1] Artificially generated plasmas are usually electrically driven and are used for a variety of applications, from lighting[4] to material processing[5-46] to even medical applications[47-48]. In each of these applications plasmas have unique properties, which enable capabilities that would often be difficult or impossible to achieve by other means. In lighting applications, a unique property of plasmas in compact fluorescent bulbs is the ability to more efficiently couple input energy into radiative processes compared to traditional incandescent bulbs. In material processing, plasmas properties allow materials to be deposited on surfaces at lower temperatures than traditional thermal processes and enable highly anisotropic etching at a size and scale that would be unattainable through most other methods.

In these applications energy is coupled into the plasma through electrostatic and electromagnetic fields, which accelerate charged particles and thereby increase their kinetic energy. That kinetic energy is imparted into neutral species through collisions. Charged species are able to gain energy from electric fields between collisions and thus are at higher temperatures

than the background neutral gas. Because of the large differences in mass, electrons do not lose much energy during elastic collisions with relatively heavy particles such as ions and neutrals. Due to this, as well as their much lighter mass, electrons are able to be accelerated between collisions to much higher kinetic energies and thus much greater temperatures than heavy particles such as ions and neutrals. Because of the relatively high temperature electrons can reach, electrons are much more likely to be able to gain enough energy to participate in excitation, ionization, and dissociation reactions when colliding with atoms and molecules.[1] All of these processes have a minimum energy required to generate the reaction product species, which is referred to as the threshold energy of the reaction.

Plasma species such as electrons, ions, and neutrals are distributed in energy within the plasma. For electrons and ions this is referred to as the electron energy distribution and ion energy distribution, respectively. These may also be referred to as the electron energy distribution function (EEDF) and ion energy distribution function (IEDF). These distributions represent the densities of either electrons or ions at a particular energy. The rate of reaction for generation of a particular plasma species with a particular threshold energy is directly related to the density and energy of the reactant species. This is why control of the electron and ion energy distributions is so important, as these distributions play a critical role in the reaction rates of both gas phase and surface processes.

1.2 Plasma Etching

One of the applications where the importance of EED and IED control is most clearly demonstrated is in materials processing and in particular in the area of plasma material etching for the semiconductor manufacturing industry. Etching of materials using plasmas is referred to as plasma etching and is considered a dry-etch process as opposed to a wet etch process, which is

a chemical etch process where a material is etched isotropically by a liquid. Plasma etching has been used for decades in the semiconductor manufacturing industry to transfer patterns defined on a mask to underlying layers of material.[2] The types of plasmas used for etching in the semiconductor industry are typically bounded, partially ionized, non-LTE plasmas operated at low pressures (<100s mTorr).

There are four main types of etching processes in plasma etching.[1] There is chemical etching in which neutral species react with surfaces forming a volatile product.[1] This process etches isotropically and is very selective. Selectivity in the semiconductor manufacturing industry is generally defined as the ratio between the etch rates of the desired material to be etched and either the underlying layer or the material being used as a mask.[26] There is physical etching, often referred to as sputtering, in which atoms are ejected from surfaces through energetic ion bombardment.[1] This process is anisotropic and non-selective. There is ion enhanced energy-driven etching, in which ions enhance etching by increasing the chemical etch reaction rate.[1] It is an anisotropic, selective (though not as selective as chemical etching) process that combines chemical and physical etching synergistically. Finally there is ion enhanced inhibitor etching, in which inhibitor molecules absorb or deposit onto a surface, which inhibits etching at locations where there is not energetic ion bombardment to remove the inhibitor molecules.[1] Like ion enhanced energy-driven etching, the process is anisotropic and selective, though not as selective as chemical etching.

Silicon etch rate in the first three regimes is shown in Fig. 1.1 demonstrating the synergistic effect in the ion enhanced etching regime. Operating in this regime allows for the high throughput needed to meet high demand in the semiconductor manufacturing industry. Using plasma etching, surface properties of materials can be modified using reactive species

(electrons, ions, radicals) created in the gas phase.[2] Reaction rates for the production of these reactive species in the gas phase are governed by plasma properties such as the species' densities and electron temperature (T_e) and surface reaction rates are governed by the flux and energy of these reactive species hitting the surface.[2]

As the demand for smaller feature sizes grows, the requirements for many process parameters becomes more and more challenging to meet.[2] Increased selectivity, critical dimension control, reduced plasma damage, and higher throughput are just some of the process challenges that need to be addressed to meet the demand for smaller feature sizes.[2] Some of the critical factors that affect our ability to meet these challenges include plasma uniformity, vertical versus lateral etch rates, feature profile control, and plasma induced damage.[2] Fulfillment of the noted challenges would be greatly aided by methods for independent control of plasma properties.[2] Some of the plasma parameters that are desired to be controlled, as well as some of the plasma etching process characteristics that are affected by these plasma parameters, are shown in Fig. 1.2. Better control of many of the mentioned plasma properties can be achieved through better control of the EED and IED, which govern many of the properties associated with the plasma.

1.3 Plasma Kinetics

The generation of reactive species in the plasma gas phase is largely driven through electron impact reactions with neutral atoms and molecules. Energetic electrons are able to participate in reaction processes such as excitation, ionization, and dissociation as long as the electron energy is above the threshold energy of the reaction. This is why the shape of the EED is so important, as the rate coefficient for these electron impact processes are determined by the EED as seen from the following equation,

$$k = \int_0^\infty f(\varepsilon)\left(\frac{2\varepsilon}{m}\right)^{1/2}\sigma(\varepsilon)d\varepsilon\,, \tag{1.3.1}$$

where k is the reaction rate coefficient, $f(\varepsilon)$ is the electron energy distribution, m is the electron mass, ε is the electron energy, and $\sigma(\varepsilon)$ is the cross section of a particular electron impact process at energy ε. This reaction rate coefficient, along with the density of the reactant species can then be used to calculate the rate of reaction, R, for a particular reaction process. For example, the rate of reaction for the electron impact process: $e + A = B$, is as follows,

$$R_1 = k_1[e][A], \tag{1.3.2}$$

where R_1 is the rate of reaction for this process, k_1 is the reaction rate coefficient for this process, $[e]$ is the density of electrons, and $[A]$ is the density of some atomic or molecular species. The rate of reaction for the electron impact process: $e + B = C$ would be,

$$R_2 = k_2[e][B], \tag{1.3.3}$$

where R_2 is the rate of reaction for this process, k_2 is the reaction rate coefficient for this process, $[e]$ is the density of electrons, and $[B]$ is the density of some atomic or molecular species. In equations 1.3.2 and 1.3.3, [e] represents the total electron density; however for reactions with a positive threshold energy only electrons above that energy can participate in the reaction. This is accounted for in the rate coefficient, which is a function of the EED.

The rates of reaction for the reaction processes are then used to determine the rate of change of the density of a plasma species; this is also called the source function of a plasma species. The source function of a plasma species is equal to the sum of the rates of reaction involving that species. If a reaction produces that species, its rate of reaction is a positive term in the sum, while if a reaction consumes that species, its rate of reaction is a negative term in the

sum. This is illustrated in the following equation calculating the source function of plasma species B,

$$S[B] = \frac{d[B]}{dt} = R_1 - R_2, \qquad (1.3.4)$$

where $S[B]$ is the source function for plasma species B. From equation 1.3.4, it can be seen that the density of reactive species created through electron impact processes, as well as molecular reactions that involve electron impact generated species, is strongly impacted by the EED. Of note, while the source function calculation of equation 1.3.4 only contains rates of reaction from electron impact processes, there may be other reactions involving only atoms and molecules or even photons, which change the density of a plasma species with time and would need to be included in determining the true source function of a plasma species.

Most of the electric power dissipated into the plasma is dissipated through the electrons.[26] It is this power that acts as the major source term for the electron energy, while electron impact processes such as excitation, ionization, dissociation, as well as thermal diffusion to the plasma boundaries are the major loss terms. By solving an energy balance equation for the rate of change of the electron temperature, the steady state electron temperature can be found. Control of plasma properties such as the EED and electron temperature, which is defined to be two-thirds the average electron energy as calculated from the EED, can be achieved through shifting of the balance point between source and loss mechanisms. Since the EED is largely responsible for the time rate of change of the density of reactive species in the plasma, the flux, energy, and surface reaction rates of many of the neutral reactive species hitting a surface are influenced by the EED.

A similar statement can be made about IEDs. Ions bring energy to a surface through collisional energy transfer with a surface. Since ions are on similar mass scales with the atoms

of the surface they impinge on, they are able to efficiently transfer energy and momentum to the surface. The ions are able to impart enough energy to assist surface chemical reaction processes and/or induce sputtering.[26] Thus the flux and energy of ionic species, as well as surface reaction rates for all species, are a function of the IED. The IED plays a major role in determining things such as etch profile[10, 41], vertical versus lateral etch rate[15], and plasma induced damage[42], which are important factors in plasma etching applications. The effect of ion energy control on vertical versus lateral etch rates and feature profile control is illustrated in Fig. 1.3. It can be seen that choosing the appropriate energy allows for a large increase in the vertical versus lateral etch rate and a more vertical feature profile. The effect of the choice of ion energy (IED control) and the ion to neutral flux ratio (EED and IED control) on changes in the silicon ion-assisted etching yield is demonstrated in Fig. 1.4, with a larger yield as ion energy increases and a lower yield as the ion to neutral ratio increases. The effect of energetic ions bombarding a silicon substrate on creating defect states that affect its electrical characteristics is demonstrated in Fig. 1.5, with higher energy ions creating a greater density of defect states.

The kinetic energy imparted to a surface through ion bombardment is largely determined by the electric potential drop across the sheath as well as the mean free path of the ions in question. Since plasmas are quasi-neutral the electric field outside the sheath region in the bulk plasma is very small and ions travel in plasmas largely at thermal speeds. When an ion enters the sheath, the electric field created from the potential gradient in the sheath, accelerates the ion and increases its kinetic energy. If the ion can traverse the entire sheath without undergoing a collision, the ion will gain kinetic energy approximately equivalent to the average sheath potential during its transit across the sheath. This is why the ratio of ion transit time to rf period is so important when applying an rf bias to a substrate.

The mean free path refers to the average distance an ion can travel before undergoing a collision. Collisions with other heavy particles, in particular charge exchange collisions, can have a large impact on the energy of ions hitting a surface. In a charge exchange collision, an ion collides with a neutral atom or molecule and an electron from the neutral is transferred to the ion. Thus the original ion becomes a neutral and the original neutral becomes an ion. This process can be either resonant, i.e. between a neutral and its own ionized form, or nonresonant, i.e. between a neutral and the ionized form of a different neutral.[1] In the case of resonant exchange only the respective states of the species are changed, but not their kinetic energy.[1]

For a nonresonant transfer, the difference in the ionization potentials of the neutral forms of the reactants is shared between the resulting ion and neutral as kinetic energy.[1] Since the kinetic energy of the originally neutral species is generally low, or approximately equal to the thermal kinetic energy of the background gas, and the kinetic energy the original ion gained in the sheath is not transferred, if a charge exchange collision happens within the sheath the new ion will not be able to convert the full potential energy of the sheath into kinetic energy. This leads to a change in the IED with an increase in the ratio of ions hitting the surface at energies less than the sheath potential to ions hitting at an energy approximately equal to the sheath potential.

1.4 Pulsed Power and dc Biases in ICPs

For the last few decades, high-density plasmas have been used to meet some of the previously mentioned plasma etching challenges.[2] High-density plasmas can be generated by a number of methods, but the method this work focuses on is that of the inductively coupled plasma (ICP). In an ICP, radio-frequency (rf) power is coupled to the plasma through a dielectric window, eliminating the need for an electrode in direct contact with the plasma such as

in the case of a capacitively coupled plasma (CCP).[2] Using this inductive method of power transfer, high plasma densities with relatively low sheath voltages can be achieved.[2] There has been extensive work on controlling both EEDs and IEDs in ICPs. Methods investigated for EED control in ICPs include gas mixture [49, 51-52], gas pressure [49, 53], source power [49-53], source power pulsing, [54-56] and tandem sources [57]. Methods investigated for IED control include, gas pressure [19, 58], electrode biasing [7, 60-64], and pulsing [2, 16-17, 63-64] of the source power and/or the electrode bias.

In this work, the use of source power pulsing, remote sources, and dc biases to modify the EED in an ICP system is investigated. The use of pulsed source power and dc biases in both continuous and pulsed formats to modify IEDs in ICP systems is also investigated. When talking about pulsing of a power source, whether the ICP power or the bias power, what is meant is that the power source is turned on for a designated amount of time and then turned off for another designated amount of time. One pulse is equivalent to one cycle through the on and off states. The total time spent going through 1 on/off cycle is the pulse period. The inverse of the pulse period is the pulse repetition frequency (PRF), which is the number of pulses that occur per unit of time. The ratio of the pulse width to the total pulse period is defined as the duty cycle of the pulse.

It was mentioned previously that in steady state the source and loss terms must balance. In a pulsed plasma, either the source or loss terms may dominate at different times during the pulse, only their average over the cycle must be zero. Duty cycle determines the proportional effect of source and loss terms on the time averaged EED. This potentially allows for modification of the time averaged EED, IED, and source functions of reactive species, as well as the time averaged flux of reactive species to a substrate. The time averaged IED hitting a

substrate can be further modified through the application of a bias on the substrate. The bias can be applied in a continuous or pulsed format. The bias modifies the sheath potential seen by ions heading to the substrate. For a pulsed bias, the time averaged IED can be modified significantly by the duty cycle of the pulsed bias, as well whether the bias is pulsed synchronously versus asynchronously to the ICP source power.

EEDs and IEDs in pulsed ICPs have been investigated extensively using a variety of methods. Two common methods to experimentally measure EEDs and IEDs are through the use of Langmuir probes[64-66] and retarding field energy analyzers (RFEAs)[60, 64] respectively. A Langmuir probe is essentially a metal probe inserted into a plasma and biased to obtain an I-V curve for a particular point within the plasma.[1] Through analysis of the I-V curve obtained by the probe, plasma parameters such as plasma potential, electron and ion density, electron temperature, and the EED can be obtained. A RFEA is an apparatus with a series of grids biased at different voltages, which selectively allows ions to pass through the grids to a collector plate at the bottom of the RFEA, while repelling electrons from the plasma and suppressing secondary electron emission from the collector plate.[67] The I-V curve obtained by the collector plate is then analyzed to get the IED. Another method for investigating plasma properties such as EEDs and IEDs in ICPs is the use of computational modeling.

1.5 Plasma Modeling

As the need for better control over plasma properties has increased, so has the need to better understand the effect of different operating parameters. Plasma properties can be affected by many factors, such as choice of gas mixture, pressure, and continuous versus pulsed operation of source power and bias. The wide array of control parameters leads to a wide operating space for plasma processing systems. A way to narrow down the choice of control parameters to

achieve a certain level of performance and to gain a deeper understanding of the physics affecting plasma properties is needed. Computational modeling of plasma systems is one way to achieve this and offers some advantages over experimental methods. Modeling of plasma systems allows for a large range of operating conditions to be investigated without the cost of building, modifying, or running a chamber to test each operating condition. Modeling of plasma systems can help to validate experimental results or identify mechanisms that lead to experimental data that deviates from desired and/or expected results. Modeling of a plasma processing system can also be extremely useful when optimizing or designing future processes.[68] It can save valuable time and financial resources, eliminating operating conditions and designs that would not be able to achieve desired performance characteristics.

There are three main methods used to model plasma processing systems: fluid, kinetic, and hybrid. In fluid simulations, each species in the plasma is described by its density, average energy, and average velocity.[69] These values are obtained by solving equations for conservation of density, energy, and momentum for each species. Maxwell's equations are also solved in conjunction with the fluid equations to obtain self-consistent electromagnetic and electrostatic fields.[69] Fluid models have the advantage of speed, but are limited in that an assumption must be made of the velocity distribution of a plasma species.[69] In kinetic simulations, typically a particle-in-cell Monte Carlo collision (PIC-MCC) method is used.[69] In PIC-MCC simulations, the plasma species kinetics are modeled by using computer particles or super-particles, with each super-particle representing a certain number of particles of the plasma species.[69] Super-particle transport is calculated by solving fundamental equations of motion, and collisions are handled using Monte Carlo methods. The advantage of this method is that statistical processes are modeled in more detail than in fluid simulations. The main limitation of

this method is computation time. The computation time is proportional to the number of super-particles, so ideally the number should be kept low; however, a sufficient number of super-particles are needed to provide a sufficient representation of energetic particles and reduce statistical noise.[69] Finally hybrid models combine both fluid and kinetic approaches, in that most plasma species are treated as fluids while some are treated kinetically as particles. Typically electrons are treated kinetically, while neutrals and ions are treated as fluids. The results of this thesis, as discussed in Chapters 3-6, are based on a 2-D hybrid modeling platform called the Hybrid Plasma Equipment Model or HPEM. The ability of the HPEM to model plasma processing systems and compute plasma properties is demonstrated in Fig. 1.6.

1.6 Control of Plasma Etch Parameters Through Control of EEDs and IEDs

There are several plasma etch parameters, intended to enhance control of the performance of wafer etch processes. Some of the plasma etch parameters where better control is desired are shown in Fig. 1.2 and include: neutral to ion flux ratio, dissociation rate, and electron temperature. These parameters can affect wafer etch performance in the areas of: etching versus deposition, vertical versus lateral etching, feature sidewall passivation, and critical dimension control.[2] Each of the mentioned parameters can be controlled through control of the EED. One possible method for controlling the EED and all three of the mentioned parameters is the use of pulsed power. Through the use of pulsed power in an ICP system, the shape of the EED can be tailored to control the rate coefficients of electron impact processes such as excitation, ionization, and dissociation. Pulsing of the power allows for the source and loss terms that affect the source functions of plasma species, to be unbalanced at different times during the pulse as long as they are balanced over the entire pulse.

In molecular gas mixtures, which are the type of mixtures typically used for plasma etching, there are a variety of electron impact processes that occur at a range of threshold energies. For a given gas mixture ratio, the EED will have the most impact on the source functions of plasma species as we know from eqs. 1.3.1 – 1.3.4. The use of pulsed power in a planar ICP system to control the EED and thus the source functions in an Ar/N_2 gas mixture is investigated using the HPEM. The effect of duty cycle on the source functions of plasma species generated by low, medium, and high threshold energy processes is modeled at multiple pressures. The goal of this study is to gain a better understanding of the ability of pulsed power to affect the rates of these processes. The ability of pulsed power to affect the temporal behavior of EEDs and source functions has a direct impact on the ability to control the neutral to ion flux ratio, dissociation rate, and electron temperature in plasma etching systems.

Another mechanism to control EEDs in a system is through the use of a secondary source.[57] The injection of electrons from a secondary source region into the primary source region can be used to tailor the EED in the primary source region. This has been investigated in a tandem ICP (T-ICP) system, with Ar as the background gas, in which the secondary ICP source is upstream from the primary source and the source regions are separated by a biasable grid. A boundary electrode is also used to affect the process parameters in the system. This tandem ICP system can be used to affect the EED, neutral to ion flux ratio, dissociation rate, and electron temperature in plasma etch processes. The focus of the investigation is on the ability of the secondary source of the T-ICP to control electron temperature and EEDs in the main source region.

Another plasma etch property where better control is desired is the ion flux to ion energy ratio. This parameter can affect wafer etch performance in the areas of: etching versus

deposition, vertical versus lateral etching, plasma induced damage, and selectivity. The ion flux to ion energy can be controlled by controlling the IED through the use of dc and rf biases on electrodes to control the IED independently of ion density. This independent control of energy and density allows a largely independent control of the ion flux and ion energy hitting a surface.

The use of dc biases on a boundary electrode in a cylindrical ICP system to control IEDs is modeled. This is a model of the system and many of the experimental conditions found in Shin et al. [64]. The applied dc biases are used to shift the plasma potential with respect to grounded surfaces and shift the energy of the IED peaks to those surfaces. As long as the bias power is small compared to the ICP power, the IED hitting a grounded surface can be shifted in energy without significantly affecting the ion density and flux. It has been shown that applying a pulsed dc bias in the afterglow of a pulsed ICP leads to a very narrow IED peak centered at approximately the bias value.[64] Having an IED with a narrow energy width and tunable peak energy can allow for increased selectivity between an etch layer and its underlying etch stop layer. If the underlying layer has a higher ion threshold energy for etching than the etch layer, a narrow width IED peak centered at an energy between the etching thresholds of the two layers could lead to a very high etch selectivity between those layers. There is also the potential for reduced plasma induced damage as the IED peak energy could be downshifted to a lower value when nearing the etch stop layer. The higher the potential dropped across the sheath the greater the energy the ion bombards the surface with and the more vertically oriented its trajectory. By applying a dc bias and shifting the plasma potential, the potential dropped across the sheath is increased and the vertical versus lateral etch rate can be controlled. Depending on the gas chemistry and ion energy, there can be either etching or deposition at the surface. For fixed gas

chemistry, dc bias control over the IED allows control over the etching versus deposition behavior.

Biases are most often applied to the substrate in plasma etching reactors. Applying a negative potential on the substrate increases the voltage drop across the sheath and accelerates positive ions to the substrate. For a fixed potential gradient and thus electric field, the ion acceleration is mass dependent. If a dc bias is applied for a short enough time period in a system with multiple ionic species, the high energy IED peaks of the ions can be separated in energy based on their mass. This allows for selective control of IED shape based on mass, with lighter ions having IEDs that extend to higher energies. This selective control of the IEDs in systems with multiple ionic species, which are often used in plasma etching systems, creates a mechanism for selective control of the ion energy to flux ratio for individual ions. The effect of short duration dc bias pulses on a substrate in a planer ICP system is modeled. IEDs are calculated under a variety of duty cycles, PRFs, and pressures.

1.7 Summary

This thesis is organized as follows:

In Chapter 2, the modeling algorithms for the Hybrid Plasma Equipment Model are discussed in detail with special emphasis on the modifications made to the model to enable accurate simulations for Chapters 4-6.

In Chapter 3, a parametric study of source power pulsing on EEDF's and source functions in a planar Ar/N_2 ICP system at different pressures and duty cycles is discussed. It is found that time averaged EEDFs are not affected by the discharge power but have a strong dependence on pressure. The time averaged source functions do not change significantly as a

function of duty cycle and the source function ratio between two processes cannot be modified by more than a factor of 2 using pulsed power alone.

In Chapter 4, IED control on grounded surfaces using dc biases on a boundary electrode in a cylindrical Ar ICP is discussed. The ICP as well as the dc bias is operated in continuous and pulsed formats. It is found that applying positive dc bias shifts the plasma potential and the peak of the IED onto a grounded surface by a value approximately equal to the applied bias voltage. The applied dc bias does not affect plasma properties such as plasma density and electron temperature due to low dc power deposition compared to the ICP power deposition. When the ICP is operated in a continuous format the IED is single peaked, while the IED is multi peaked when the ICP power is pulsed. Applying a pulsed dc bias in the afterglow of a pulsed ICP creates a very narrow IED peak at approximately the dc bias energy and allows for very narrow IED peaks, with the energy of the peak tunable based on the dc bias value. The content of this chapter is taken almost entirely from work that has been submitted to Logue et al. [70].

In Chapter 5, the use of pulsed dc biases on a substrate electrode in a planar ICP to selectively control the IEDs of different ions based on their mass is discussed. $Ar/H_2$and Xe/H_2 gas chemistries are investigated. The pulsed dc bias creates multi peaked IEDs with the highest energy peak coming from ion transit through the sheath during the time the dc bias is on. It is found that when the length of time the dc bias is on exceeds the sheath transit time of an ion, the highest energy IED peak for that ion is approximately equal to the bias energy independent of mass. When the dc bias length is shorter than the sheath transit time of an ion, then the highest energy IED peak of that ion is shifted to lower energy. The sheath transit time of an ion is increased as a function of its mass and thus the highest energy IED peak of heavier ions can be shifted to a lower energy compared to the highest energy IED peak of lighter ions.

In Chapter 6, control of the EED in a cylindrical ICP through the use of a secondary cylindrical ICP source in tandem with the main ICP, as well as dc biases on a boundary electrode is discussed. The gas chemistry used is Ar. It is found that the secondary ICP, with no bias on the boundary electrode, has little to no effect on the EED in the main ICP when the main ICP is on. Applying a dc bias on the boundary electrode does have some effect on the EED in the main ICP, particularly when the secondary ICP source is close to the primary source. The secondary ICP source does affect T_e and the EED in the afterglow period when the main ICP is pulsed. It is found that high energy electrons from the top ICP are able to raise T_e late in the afterglow of the pulse and lift the tail of the EED in the afterglow compared to the case when the secondary ICP is off.

In Chapter 7, a summary of the research discussed in the previous chapters is given. The validation and impact of the results of this thesis are then discussed. When possible, direct comparisons to experimental data are used for validation. The chapter concludes with a discussion of future work that could be performed to expand on the work of this thesis.

1.8 Figures

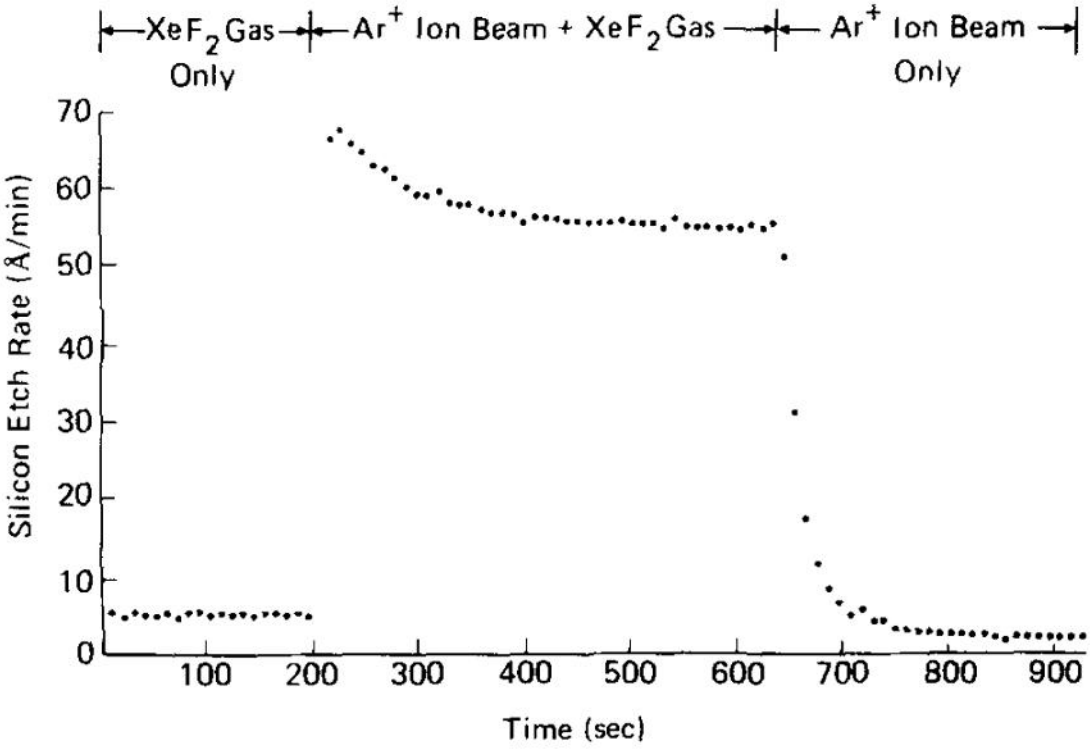

Figure 1.1 Silicon etch rate for three different etching mechanisms (chemical, ion-enhanced, and physical). Chemical etching is demonstrated by the etch rate with XeF_2 gas only. Ion-enhanced etching is demonstrated by the etch rate with Ar^+ ion beam + XeF_2 gas. Physical etching is demonstrated by the etch rate with Ar^+ ion beam only.[14]

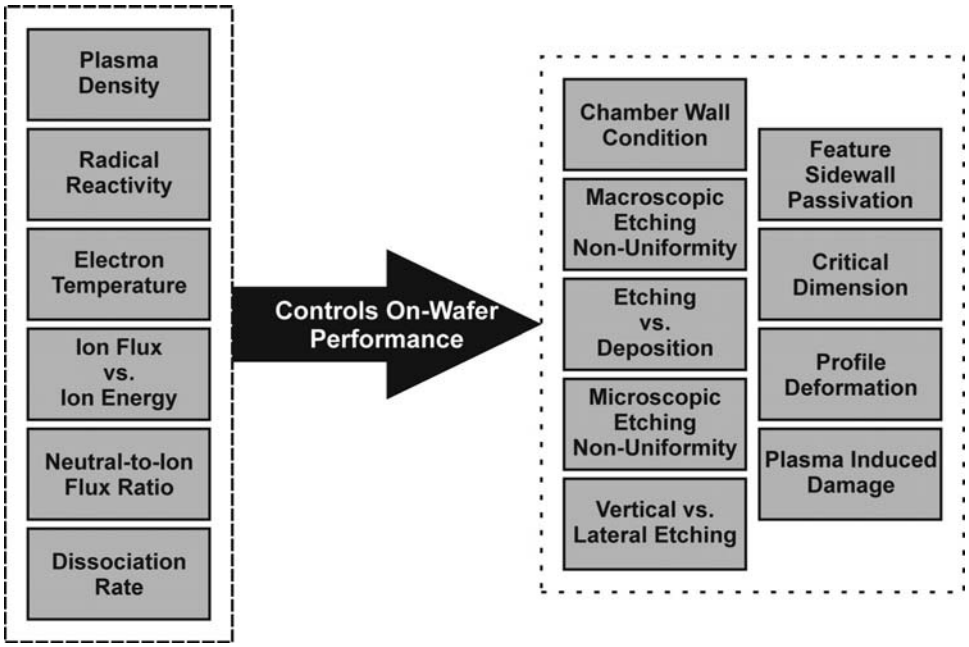

Figure 1.2 Process parameters and etch process characteristics where better control is needed for advanced plasma etch processes.[2]

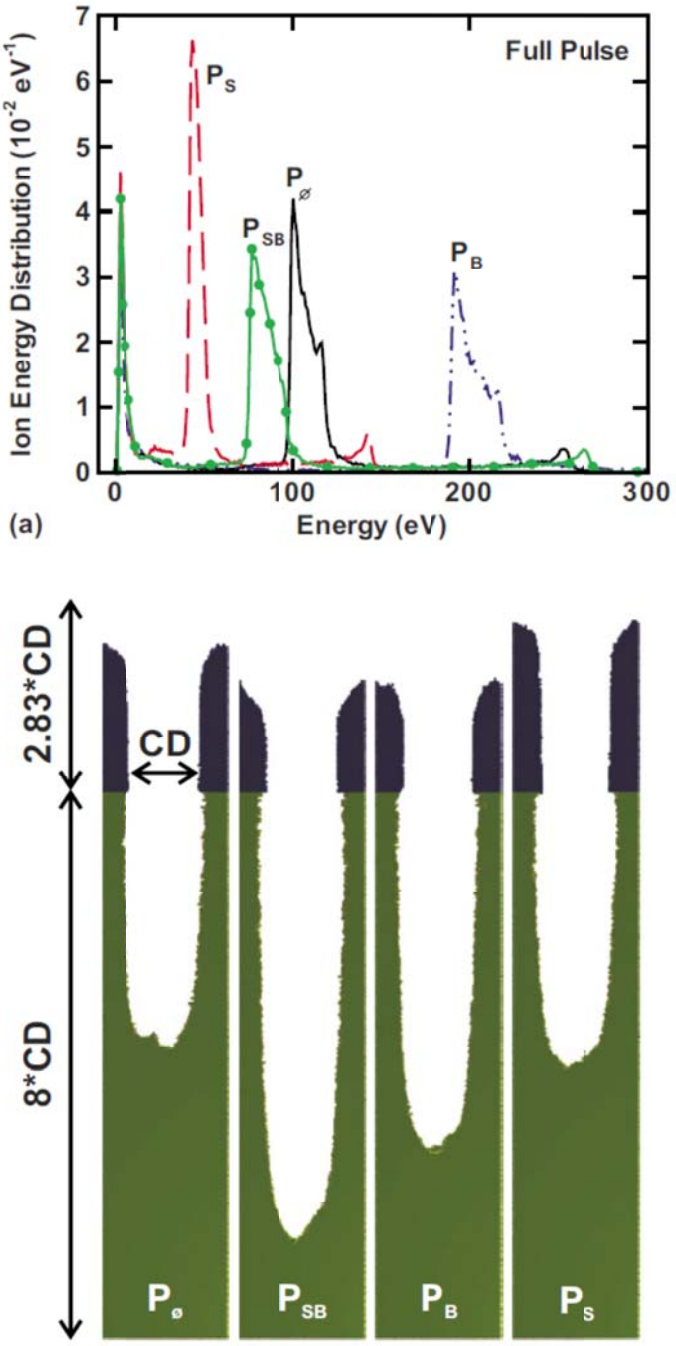

Figure 1.3 Effect of IED on vertical versus lateral etch rate and etch profile for polysilicon with an amorphous carbon hard mask.[16]

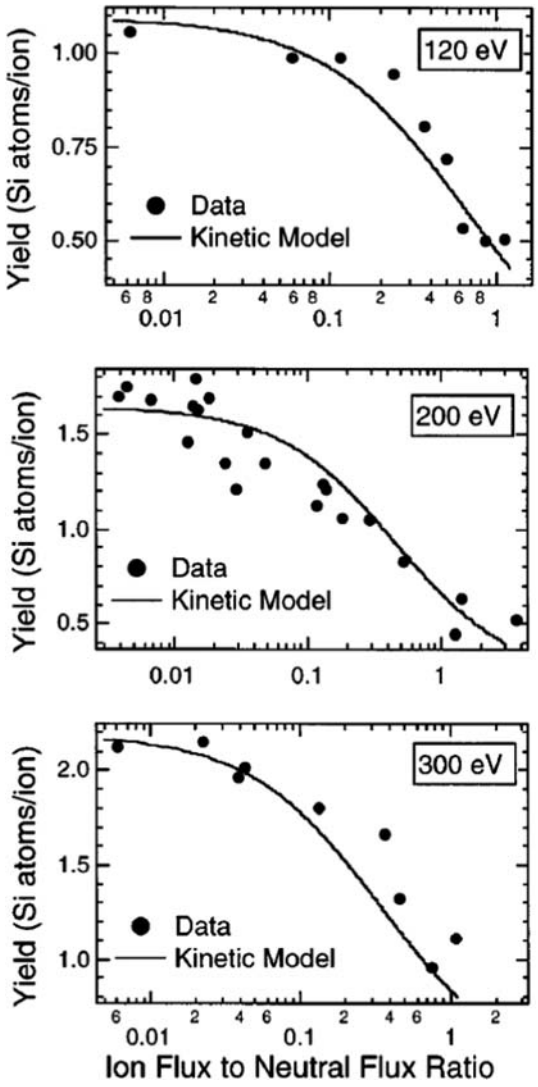

Figure 1.4 Silicon ion-assisted etch yield versus ion to neutral flux ratio at three ion energies.[28]

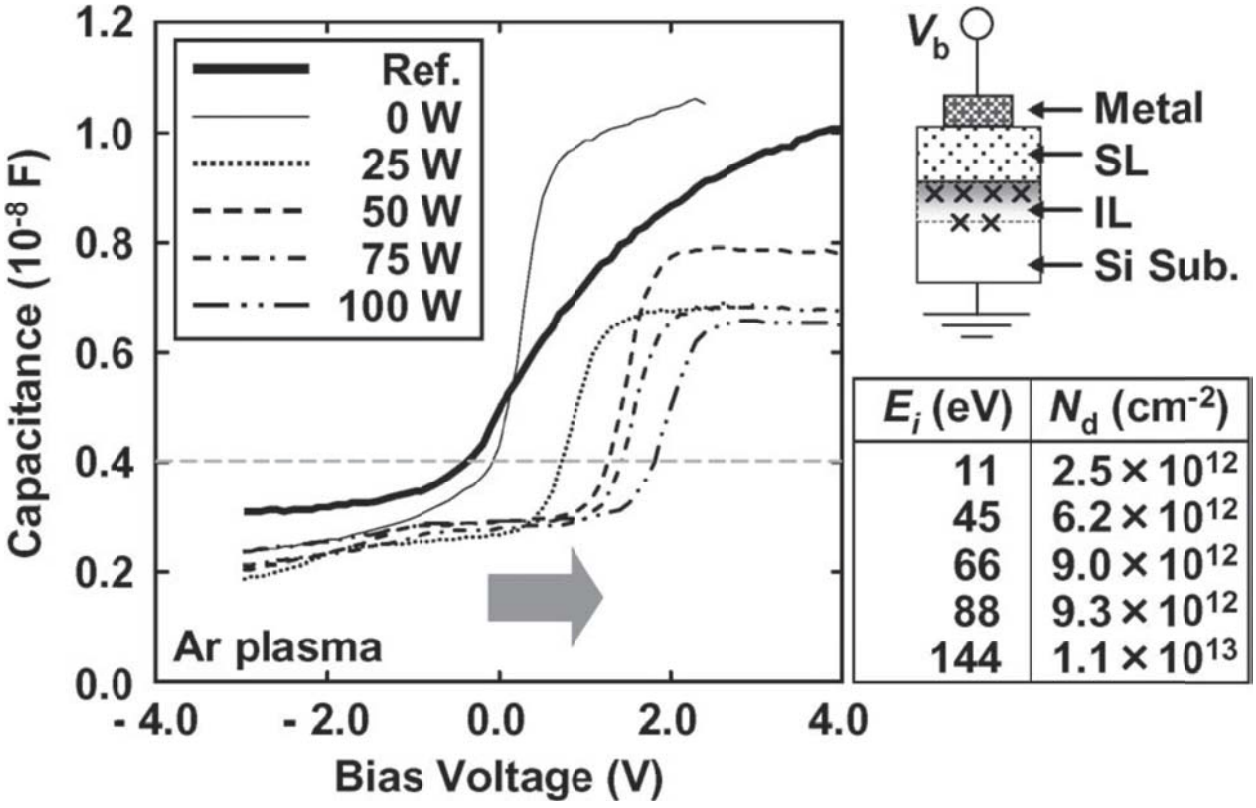

Figure 1.5 Capacitance versus voltage measurement on a silicon substrate exposed to an Argon ICP at various substrate bias powers. Corresponding ion bombardment energy and surface defect density is also shown.[59]

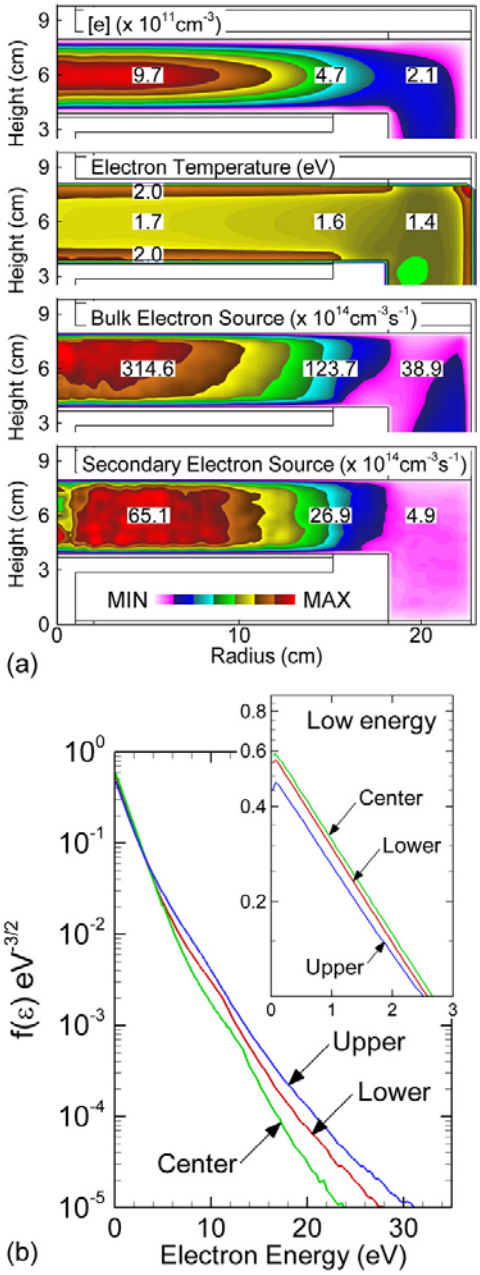

Figure 1.6 Plasma parameters of a dual frequency CCP operated in continuous mode as computed by the HPEM.[71]

1.9 References

1. M. A. Lieberman and A. J. Lichtenberg, Principles of Plasma Discharges and Materials Processing (John Wiley & Sons, Inc., Hoboken, NJ, 2005).

2. S. Banna, A. Agarwal, G. Cunge, M. Darnon, E. Pargon, and O. Joubert, J. Vac. Sci. Technol. A **30**, 040801 (2012).

3. M. Boulos, P. Fauchais, and E. Pfender, Thermal Plasmas: Fundamentals and Applications (Springer US, Boston, MA, 1994).

4. D. Uhrlandt, R. Bussiahn, S. Gorchakov, H. Lange, D. Loffhagen, and D. Nötzold, J. Phys. D: Appl. Phys. **38**, 3318 (2005).

5. D.T.K. Kwok, L. Tong, C.Y. Yeung, C.G. dos Remedios, and P. K. Chu, Surf. And Coatings Technol. **204**, 2892 (2010)

6. M. Barela, H. Anderson, and G. S. Oehrlein, J. Vac. Sci. Technol. A **23**, 408 (2005).

7. A. Agarwal and M. J. Kushner, J. Vac. Sci. Technol. A **23**, 1440 (2005).

8. A. Agarwal and M. J. Kushner, J. Vac. Sci. Technol. A **26**, 498 (2008).

9. M. Sobolewski, J. Vac. Sci. Technol. A **24**, 1892 (2006).

10. X. Li, L. Ling, X. Hua, G. S. Oehrlein, Y. Wang, and H. M. Anderson, J. Vac. Sci. Technol. A **21**, 1955 (2003).

11. M. Schaepkens, G. S. Oehrlein, J. M. Cook, J. Vac. Sci. Technol. B **18**, 848 (2000).

12. S. D. Athavale and D. J. Economou, J. Vac. Sci. Technol. A **13**, 966 (1995).

13. U. Cvelbar, J. Phys. D: Appl. Phys. **44**, 174014 (2011).

14. J. W. Coburn and H. F. Winters, J. Appl. Phys. **50**, 3189 (1979).

15. J. W. Coburn and H. F. Winters, J. Vac. Sci. Technol. **16**, 391 (1979).

16. A. Agarwal, P. J. Stout, S. Banna, S. Rauf, K. Collins, J. Vac. Sci. Technol. A **29**, 011017 (2011).

17. A. Agarwal, P. J. Stout, S. Banna, S. Rauf, K. Tokashiki, J.-Y. Lee, K. Collins, J. Appl. Phys. **106**, 103305 (2009).

18. R. Ye, T. Ishigaki, and T. Sakuta, Plasma Sources Sci. Technol. **14**, 387 (2005).

19. J. Zhou, I. T. Martin, R. Ayers, E. Adams, D. Liu, E. R. Fisher, Plasma Sources Sci. Technol. **15**, 714 (2006).

20. T. Yew and R. Reif, J. Appl. Phys. **68**, 4681 (1990).

21. J. Hopwood, Plasma Sources Sci. Technol. **1**, 109 (1992).

22. S. Samukawa and T. Mieno, Plasma Sources Sci. Technol. **5**, 132 (1996).

23. K. Ono and M. Tuda, Thin Solid Films **374**, 208 (2000).

24. H. Sugai, K. Nakamura, Y. Hikosaka, and M. Nakamura, J. Vac. Sci. Technol. A **13**, 887 (1995).

25. D. J. Economou, Thin Solid Films **365**, 348 (2000).

26. C. Cardinaud, M.-C. Peignon, and P.-Y. Tessier, Applied Surface Science **164**, 72 (2000).

27. V. M. Donnelly and A. Kornblit, J. Vac. Sci. Technol. A **31**, 050825 (2013).

28. J. A. Levinson, E. S. G. Shaqfeh, M. Balooch, and A. V. Hamza, J. Vac. Sci. Technol. A **15**, 1902 (1997).

29. S. W. Pang, D. D. Rathman, D. J. Silversmith, R. W. Mountain, and P. D. DeGraff, J. Appl. Phys. **54**, 3272 (1983).

30. D. B. Graves and D. Humbird, Applied Surface Science **192**, 72 (2002).

31. H. F. Winters, J. W. Coburn, and T. J. Chuang, J. Vac. Sci. Technol. B **1**, 469 (1983).

32. T. H. Ahn, K. Nakamura, and H. Sugai, Plasma Sources Sci. Technol. **5**, 139 (1996).

33. S. Samakuwa, K. Noguchi, J. I. Colonell, K. H. A. Bogart, M. V. Malyshev, and V. M. Donnelly, J. Vac. Sci. Technol. B **18**, 834 (2000).

34. M. Schaepkens, G. S. Oehrlein, J. M. Cook, J. Vac. Sci. Technol. B **18**, 856 (2000).

35. M.H. Jeon, A.K. Mishra, S.-K. Kang, K.N. Kim, I.J. Kim, S.B. Lee, T.H. Sin, G.Y. Yeom, Current Applied Physics **13**, 1830 (2013).

36. G. Cunge, D. Vempaire, R. Ramos, M. Touzeau, O. Joubert, P. Bodard, and N. Sadeghi, Plasma Sources Sci. Technol. **19**, 034017 (2010).

37. L. Godet, S. Radovanov, J. Sheuer, C. Cardinaud, N. Fernandez, Y. Ferro, and G. Cartry, Plasma Sources Sci. Technol. **21**, 065006 (2012).

38. C. Petit-Etienne, M. Darnon, L. Vallier, E. Pargon, G. Cunge, F. Boulard, O. Jounert, S. Banna, and T. Lill, J. Vac. Sci. Technol. B **28**, 926 (2010).

39. T. Maruyama, N. FujiWara, S.Ogino, and M. Yoneda, Jpn. J. Appl. Phys. **36**, 2526 (1997).

40. T. Goto and M. Hori, Jpn. J. Appl. Phys. **35**, 6521 (1996).

41. C. Choi, O. S. Kwon, Y. S. Seol, Y. W. Kim, and I. H. Choi, J. Vac. Sci. Technol. B **18**, 811 (2000).

42. E. Kunnen, M. R. Baklanov, A. Franquet, D. Shamiryan, T. V. Rakhimova, A. M. Urbanowicz, H. Struyf, and W. Boullart, J. Vac. Sci. Technol. B **28**, 450 (2010).

43. M. M. Mirza, H. Zhou, P. Velha, X. Li, K. E. Docherty, A. Samarelli, G. Ternent, and D. J. Paul, J. Vac. Sci. Technol. B **30**, 06FF02 (2012).

44. A. Zeniou, K. Ellinas, A. Olziersky, and E. Gogolides, Nanotechnology **25**, 035302 (2014)

45. Y. Zhao, P. Fay, A. Wibowo, and C. Youtsey, J. Vac. Sci. Technol. B **31**, 06FF05 (2013).

46. S. Q. Xiao, S. Xu, and K. Ostrikov, Materials Science and Engineering R **78**, 1 (2014)

47. G. Fridman, A. Shereshevsky, M. M. Jost, A. D. Brooks, A. Fridman, A. Gutsol, V. Vasilets, and G. Friedman, Plasma Chem Plasma Process **27**, 163 (2007).

48. A. Harsch, J. Calderon, R.B. Timmons, and G.W. Gross, Journal of Neuroscience Methods **98**, 135 (2000).

49. S.-X. Zhao, F. Gao, Y.-N. Wang, and A. Bogaerts, Plasma Sources Sci. Technol. **21**, 025008 (2012).

50. H.-C. Lee, J.-K. Lee, and C.-W. Chung, Phys. Plasmas **17**, 033506 (2010).

51. M. A. Song, Y.-W. Lee, and T. H. Chung, Phys. Plasmas **18**, 023504 (2011).

52. Y. W. Lee, H. L. Lee, and T. H. Chung, J. Appl. Phys. **109**, 113302 (2011).

53. V. A. Godyak, IEEE Trans. Plasma Sci. **34**, 755 (2006).

54. N. A. Dyatko, Y. Z. Ionikh, N. B. Kolokolov, A. V. Meshchanov, and A. P. Napartovich, J. Phys. D: Appl. Phys. **33**, 2010 (2000).

55. M. V. Malyshev and V. M. Donnelly, Plasma Sources Sci. Technol. **9**, 353 (2000).

56. A. Maresca, K. Orlov, and U. Kortshagen, Phys. Rev. E **65**, 056405 (2002).

57. S. Uhm, K.-H. Lee, H. Y. Chang, and C. W. Chung, Phys. Plasmas **11,** 4830 (2004).

58. A. Ranjan, V. M. Donnelly, and D. J. Economou, J. Vac. Sci. Technol. A **24**, 1839 (2006).

59. K. Eriguchi, Y. Nakakubo, A. Matsuda, Y. Takao, and K. Ono, IEEE Electron Device Letters **30**, 1275 (2009)

60. J. R. Woodworth, I. C. Abraham, M. E. Riley, P. A. Miller, T. W. Hamilton, B. P. Aragon, R. J. Shul, and C. G. Willison, J. Vac. Sci. Technol. A **20**, 873 (2002).

61. S. Rauf, J. Appl. Phys. **87**, 7647 (2000).

62. S.-B. Wang and A. E. Wendt, J. Vac. Sci. Technol. A **19**, 2425 (2001).

63. P. Diomede, D. J. Economou, and V. M. Donnelly, J. Appl. Phys. **109**, 083302 (2011).

64. H. Shin, W. Zhu, L. Xu, V. M. Donnelly, and D. J. Economou, Plasma Sources Sci. Technol. **20**, 055001 (2011).

65. L. J. Mahoney, A. E. Wendt, E. Barrios, C. J. Richards, and J. L. Shohet, J. Appl. Phys. **76**, 2041 (1994).

66. V. A. Godyak, R. B. Piejak, and B. M. Alexandrovich, Plasma Sources Sci. Technol. **11**, 525 (2002).

67. L. Xu, D. J. Economou, V. M. Donnelly, and P. Ruchhoeft, Appl. Phys. Lett. **87**, 041502 (2005).

68. S. Hamaguchi, IBM J. Res. Develop. **43**, 199 (1999).

69. H. C. Kim, F. Iza, S. S. Yang, M. Radmilović-Radjenović, and J. K. Lee, J. Phys. D: Appl. Phys. **38**, R283 (2005).

70. M. D. Logue, H. Shin, W. Zhu, L. Xu, V. M. Donnelly, D. J. Economou, and M. J. Kushner, Plasma Sources Sci. Technol. **21**, 065009 (2012).

71. S.-H. Song and M. J. Kushner, Plasma Sources Sci. Technol. **21**, 055028 (2012).

Chapter 2 Description of the Model

2.1 Introduction

The model employed in this thesis is the Hybrid Plasma Equipment Model (HPEM). The HPEM is developed to model low temperature plasmas at low to moderate pressures (<10 Torr) in plasma processing systems.[1-17] The HPEM is a two-dimensional fluid hydrodynamics model consisting of separate modules, each of which addresses different physical phenomena or the same phenomena using different techniques, and transfers information between the modules in a hierarchical manner.[1] The modules are executed sequentially on time scales short enough to resolve pulsed periods. A single execution cycle through all modules used in a simulation, with each module accepting data from the previous module and providing data for the next in a sequential manner, is called an iteration.[1] The modules are cycled through until a convergence is reached or a specified number of iterations have occurred.

There can be large differences in the range of the dynamic and integrating time steps for each module. The HPEM uses time slicing techniques to address this. Thus, a given module holds the inputs from other modules constant, or only allows the inputs to vary in time in a predetermined way, while executing its own code. The time spent in a module is determined by its dynamic timescale. For this technique to be effective, some fore-knowledge is needed regarding the degree to which changes in quantities in another module affect the results of the current module.[1] When trying to integrate the HPEM to a steady state (SS) or harmonic steady state (HSS), acceleration techniques are used to account for the large difference in timescales needed for different physical phenomena to reach a SS or HSS. Time slicing is one form of

acceleration.[1] Another form of acceleration involves stopping the simulation, adjusting species densities toward their SS or HSS values, and then restarting the simulation.[1] The HPEM uses a single structured, rectilinear mesh in all modules. Densities, temperatures, potentials, and magnetic fields are calculated at the mesh vertices, while fluxes and electric fields are calculated at the mid-points between vertices. Material properties such as permittivity and conductivity are specified at the vertices as well as in the interior of numerical cells. This allows the boundary between different materials to be owned by either material.

There are four modules used in this investigation. First, the Electro Magnetic Module (EMM) is used to solve Maxwell's equations for antenna produced electric and magnetic fields such as for plasmas generated by inductively coupled, helicon, or microwave sources. Using cylindrical coordinates and antenna currents in the azimuthal direction, the EMM produces $E_\theta(\vec{r},\phi)$, $B_r(\vec{r},\phi)$, and $B_z(\vec{r},\phi)$, where ϕ is the spatially dependent phase.[1] Second, the Electron Energy Transport Module (EETM) uses the calculated fields from the EMM and electrostatic electric fields ($E_r(\vec{r},\phi), E_z(\vec{r},\phi)$) from the Fluid Kinetics-Poisson Module (FKPM) to produce electron energy distributions (EEDs), which in turn produce electron transport and impact rate coefficients. The EETM can calculate the electron energy distribution through several different methods including: a Local Field Approximation, an electron Monte-Carlo simulation, or an electron energy equation. The results discussed in Chapters 3 – 6 use an electron Monte Carlo simulation (eMCS), which involves electron-electron collisions, to obtain the electron energy distribution.

Third, the FKPM is used to obtain densities, fluxes, and temperatures of all charged and neutral species, as well as the electric potential from the solution of Poisson's equation. Separate continuity, momentum, and energy equations are used for all heavy species. Continuity

equations are used for electrons where fluxes are represented using conventional drift-diffusion. Fourth, the Plasma Chemistry Monte Carlo Module (PCMCM) is used to obtain the fluxes as well as the energy and angular distributions of charged and neutral species striking chamber surfaces. The electron temperature, T_e, is obtained from $T_e = \frac{2}{3}\langle\varepsilon\rangle$, where the average electron energy $\langle\varepsilon\rangle$ is computed from the electron energy distributions produced by the EETM.

2.2 Electromagnetics Module

On the first iteration in the EMM, the inputs to the EMM have an assumed profile based on initial pre-set conditions. Because of the modular approach of the HPEM, the module has no knowledge of how its inputs are calculated and the calculation of the electromagnetic fields in the system is independent of the method used to calculate the EMM input parameters. The EMM calculates the inductively coupled electric and magnetic fields in the system produced from one or more rf coilsets or from a microwave source. The EMM also calculates static magnetic fields, produced by solenoid coils or permanent magnets, in the radial (r) and axial (z) directions.

Maxwell's equations are solved in the frequency domain under time harmonic conditions to obtain the spatially dependent, vector, and phase components of antenna produced electric and magnetic fields during the rf cycle. The EMM takes in as input parameters, the magnetostatic field, conductivity, plasma current density, and non-plasma current density as functions of position and phase to calculate the electromagnetic fields. The EMM is also called when the effects of static magnetic fields, such as those generated by permanent magnets or solenoid coils, are included in the simulation. When including the effects of static magnetic fields, the tensor forms of the transport coefficients (e.g. conductivity, mobility, diffusion coefficient) should be used in the model. There are no microwave sources or static magnetic fields in this study.

Under these conditions, azimuthally symmetric antennas, which are the type of antennas used in this study, produce only an azimuthal (θ) component of the rf electric field, as well as radial (r) and axial (z) components of the rf magnetic field in cylindrical coordinates. The amplitude of the rf electric field is obtained by solving the wave equation:

$$-\nabla\left(\frac{1}{\mu}\nabla\cdot\vec{E}\right)+\nabla\cdot\left(\frac{1}{\mu}\nabla\vec{E}\right)=\frac{\partial^2\left(\varepsilon\vec{E}\right)}{\partial t^2}+\frac{\partial\left(\vec{J}_{plasma}+\vec{J}_{antenna}\right)}{\partial t}, \tag{2.2.1}$$

where μ is the permeability, $\vec{E}$ is the azimuthal electric field, ε is the permittivity, $\vec{J}_{antenna}$ is the antenna current density, and $\vec{J}_{plasma}(r,\phi)=\overline{\overline{\sigma}}\cdot E_\theta(r,\phi)+\overrightarrow{J_e}(r,\phi)_{MCS}$ is the plasma current density by electrons with tensor conductivity $\overline{\overline{\sigma}}$. $\overrightarrow{J_e}(r,\phi)_{MCS}$ is the kinetically derived electron current obtained from the eMCS. The inclusion of $\overrightarrow{J_e}(r,\phi)_{MCS}$ is optional. The ion current is ignored due to the low mobility of ions. The rf magnetic field is computed from the rf electric field by the equation

$$B(r,z)=(i/\omega)\nabla\times\vec{E}\,. \tag{2.2.2}$$

The boundary conditions imposed on the solution of the wave equation are that $E_\theta=0$ on metal surfaces in the reactor and on the axis ($r=0$). A metal layer is specified in the mesh along all boundaries of the system geometry, except along the axis ($r=0$) in symmetric systems to ensure that $E_\theta=0$ at the boundaries of the system.

In the absence of a static magnetic field, which is the case for the results of this thesis, the tensor form of the conductivity is equal to its isotropic value, σ_0, given by:

$$\sigma_0=\frac{q_e^2 n_e}{m_e}\frac{1}{\nu_m+i\omega}, \tag{2.2.3}$$

where q_e is the unit electron charge, n_e is the electron density, m_e is the electron mass, ν_m is the electron momentum transfer collision frequency, and ω is the rf source frequency. For calculating power deposition only the real part of the conductivity is used.

In order to obtain the results in Chapter 6, several modules including the EMM have to be modified. Originally the HPEM was setup to allow multiple ICP coilsets (maximum of 3) to be modeled, but the electron Monte Carlo simulation module (eMCS) could not be used to calculate the electron energy distribution in the EETM. Instead an electron energy equation is used to solve for the EED. In order to allow for the eMCS to be used in the EETM, variables used in calculating the spatially dependent magnitude and phase of the electromagnetic fields have to be modified to correctly add the contributions from each coilset. The arrays for the variables containing the magnitudes and phases of the fields have to be expanded in dimension to allow for the contribution of each coilset to be stored. The calculation for the spatially dependent azimuthal electric fields and the corresponding power deposition is looped through for each coilset and then added together to obtain the total azimuthal electric field and power deposition from all coilsets.

The EMM is also modified to correct for non-collisional heating effects in the calculation of the azimuthal field and ICP power deposition when multiple coilsets are involved. The inductively coupled fields calculated in the EMM are normalized to provide the total power deposition as specified by the user. There are three approaches to do this. The first approach assumes completely collisional power deposition and assumes power to be equal to $\vec{J} \cdot \vec{E}$. This ignores non-collisional heating effects. The second way to normalize the electric field to provide the specified power is to calculate the power "kinetically" in the eMCS, which will correct for non-collisional heating effects. When correcting for non-collisional heating effects, the electric

field and power deposition by ICP coils is modified by a correction factor between 1/3 and 7. The third approach is to calculate "kinetic" electron currents in the eMCS and feed them back into the calculation of the electric field. This will include the effect of non-collisional heating. The EMM is modified to allow for the second approach of normalizing the electric field, which corrects for non-collisional heating effects, to be used with multiple coilsets.

2.3 Electron Energy Transport Module

The EETM calculates the EEDF as a function of energy, position, and phase, and then uses the calculated EEDF to determine electron impact rate coefficients and source functions as a function of position and phase. The EETM takes in the density of plasma species as a function of position as well as the electromagnetic, electrostatic, and magnetostatic fields as a function of position and phase. The densities of plasma species as well as the electro-static fields are calculated in the FKPM and their values are then fed into the EETM. The EEDF can be calculated in one of three ways: a Local Field Approximation, Monte Carlo Simulation, or Electron Energy Equation. The modular approach of the HPEM allows the method for calculating the EEDF to be chosen based on what is most appropriate for the operating conditions without worrying about affecting the calculation of other parameters in other modules. Once the EEDF has been obtained, the resulting electron impact rate coefficients and source functions are calculated and fed back into the FKPM, completing the cycle. For the work of this thesis the Monte Carlo method was chosen. Boltzmann's equation, eq. 2.3.1, is solved for using an electron Monte Carlo simulation (eMCS), to calculate the EEDFs for both bulk and secondary electrons. The eMCS is described in detail in [18, 19] and a summary of those descriptions will be presented here.

$$\frac{\partial f\left(\vec{v},\vec{r},t\right)}{\partial t} = -\vec{v}\nabla f\left(\vec{v},\vec{r},t\right) - \frac{q\left(\vec{E}_{rz}\left(\vec{r}\right)+\vec{E}_{\theta}\left(\vec{r},\phi\right)+\vec{v}\times\vec{B}_{rz}\left(\vec{r},\phi\right)\right)}{m}\nabla_{v} f\left(\vec{v},\vec{r},t\right) + \left(\frac{\partial f\left(\vec{v},\vec{r},t\right)}{\partial t}\right)_{c}, \qquad (2.3.1)$$

2.3.1 Electron Monte-Carlo Simulation

The eMCS is a 3v-3d (3 velocity components, 3 dimensions) model which integrates electron trajectories from electromagnetic, electrostatic, and magnetostatic fields obtained from the EMM and FKPM, and uses Monte Carlo techniques for collisions. In the FKPM, the densities of plasma species as well as Poisson's equation are integrated as a function of time over many rf cycles. The vector components of the electric field as a function of position and phase, $\vec{E}(\vec{r},\phi)$, as well as the cycle averaged densities of all charged and neutral species, $N_i(\vec{r})$, are recorded during the last rf cycle before the eMCS is called. These recordings are then transferred to the eMCS, where two simulations are performed, one for bulk electrons and one for secondary beam electrons.

On the first call to the eMCS, when calculating the EEDF for bulk electrons, $f_b(\varepsilon,\vec{r})$, the electrons are initially given a Maxwellian velocity distribution and placed in the reactor using a distribution weighted by the local electron density. On subsequent calls the trajectories are restarted from their coordinates at the end of the previous call. Electron trajectories are advanced using a second order Euler method with pseudoparticles being used to represent electrons. The acceleration of electrons, and thus the advancement of electron trajectories, is governed by the Lorentz equation,

$$\frac{d\vec{v}}{dt} = \frac{q_e}{m_e}\left(\vec{E} + \vec{v}\times\vec{B}\right), \tag{2.3.2}$$

where $\vec{E}$ is the local electric field, $\vec{B}$ is the local magnetic field, $\vec{v} = \frac{d\vec{r}}{dt}$ is the velocity, and $\vec{r}$ is the location of the pseudoparticle. The electric field contains both an rf component from the EMM as well as an electrostatic component from the FKPM. The magnetic field contains both rf

and static components as well, although in this thesis there are no static components as there are no magnetostatic fields. As described by Song and Kushner [19],

"The time step Δt for each pseudoparticle is chosen as the minimum of the following: a specified fraction of the rf cycle, the time to cross half of the computational mesh in any direction, the time to the next collision, the time for the particle to be decelerated to zero speed, or the time to when statistics are being collected when all particles should be at the same time, T_f."

A pseudoparticle's trajectory is no longer integrated once it has reached T_f, until all other pseudoparticles reach T_f. After recording statistics, the trajectories are restarted.

An energy grid is used to collect or calculate statistics and collision frequencies. Energy bins have constant widths over a specified energy range, and within an energy bin i, the total collision frequency, ν_i, is computed by summing all possible collisions with every heavy particle plasma species using the following equation,

$$\nu_{\mathrm{i}} = \left(\frac{2\varepsilon_{\mathrm{i}}}{\mathrm{m_e}} \right)^{\frac{1}{2}} \sum_{\mathrm{j,k}} \sigma_{\mathrm{ijk}} \mathrm{N_j} \,, \tag{2.3.3}$$

where ε_i is the average energy within the bin, m_e is the electron mass, σ_{ijk} is the cross section at energy i, for species j and collision process k, and N_j is the number density of species j.[18, 19] As this point, ν_i does not account for the frequency of electron-electron (*e*-*e*) collisions.

Null collision cross sections are used to provide a constant collision frequency. The null collision frequency in a particular energy range, is equal to the difference of the actual collision frequency and the maximum collision frequency in that range. The time between collisions is obtained from

$$\Delta t = -\ln(r_1)/\nu_{mj} \,, \tag{2.3.4}$$

where r_1 is a random number distributed on (0,1) and ν_{mj} is the maximum collision frequency in energy range j based on both electron energy and density of collision partners. If a null

collision is determined to have occurred, then the electron's trajectory is unaltered. If instead a real collision is determined to have occurred, the electron energy is modified according to the type of collision and the electron trajectory is scattered to reflect the occurrence of the collision.

Statistics for $f_b(\varepsilon)$ are collected for every particle on every time step. The particles are binned by energy and location and are proportionally weighted to the product of the number of electrons each pseudoparticle represents, *w*, and its last time step, Δt. A particle's weighting is distributed to its own cell and to neighboring cells in proportion to the fraction of the volume of the finite particle size that resides in the neighboring cell, η. A particle's size and volume are equal to that of the numerical mesh. Thus, for a particle in spatial bin j and energy bin i, the running sum of statistics is

$$\sum_{j'=j,neighbors} \left[F_{ij'} \rightarrow F_{ij'} + w\Delta t \eta_{jj'} \right]. \tag{2.3.5}$$

When modeling transients, there should be frequent feedback from the eMCS to the FKPM and vice-versa. This means the relative change in power or voltage should be small between calls to the eMCS. In the eMCS pseudoparticles are added for ionizations (with a randomly chosen isotropic angular distribution) and removed for losses such as those incurred by attachment, recombination, or leaving the volume. If the particle number exceeds a maximum value, then the particle number is reduced by randomly removing particles. If the particle number is reduced below a minimum value, particles are randomly seeded in the plasma.

At the end of a given call to the eMCS, $f_b(\varepsilon, \vec{r})$ at each spatial location is obtained by normalizing the statistics such that

$$\sum_i F_{ij} = \sum_i f_{bij} \varepsilon_i^{\frac{1}{2}} \Delta\varepsilon_i = 1, \tag{2.3.6}$$

where f_{bij} ($eV^{-3/2}$) is $f_b(\varepsilon_i,\vec{r})$ at $\vec{r}$, and $\Delta\varepsilon_i$ is the width of the energy bin. F_{ij} is the sum of the pseudoparticles's weightings at $\vec{r}$ for energy bin i having energy ε_i.

A particle mesh technique where electrons collide with an energy resolved electron fluid is used to account for e-e collisions. The spatially dependent $f_b(\varepsilon,\vec{r})$ recorded during the previous call to the eMCS allows this to be accomplished in the following manner. The incident pseudoparticle in the e-e collision has an initial velocity $\vec{v}_0$. The velocity of the collision partner for the incident pseudoparticle is randomly chosen from $f_b(\varepsilon,\vec{r})$ at that location. This was computed on the previous call to the eMCS. Only the energy distribution $f_b(\varepsilon,\vec{r})$ is retained from the previous call to the eMCS, so it is assumed that the target electron has an isotropic angular distribution. A cumulative probability is used to determine the probability of selecting a collision partner having energy ε' for a pseudoparticle in the j^{th} spatial bin. The cumulative probability is

$$\Pi_j(\varepsilon_i') = \sum_{k=1}^{i} P_j(\varepsilon_k') / \sum_k P_j(\varepsilon_k'), \tag{2.3.7}$$

$$P_j(\varepsilon') = f_j(\varepsilon')\varepsilon'^{1/2}\,\Delta\varepsilon' / \left(\sum_i f_j(\varepsilon'_i)\varepsilon_i'^{1/2}\,\Delta\varepsilon'\right), \tag{2.3.8}$$

where $f_j(\varepsilon')$ is $f_b(\varepsilon,\vec{r})$ in the j^{th} spatial bin, ε' is the energy of the electron collision partner, and $\Delta\varepsilon'$ is the width of the energy bin of the collision partner. The summation in the numerator of eq. 2.3.7 is over lower energies so that $\sum_i \Pi_j(\varepsilon_i') = 1$ and the summation in eq. 2.3.8 is over the entire energy range.

The energy of the target electron ε_i' must satisfy the relation

$$\Pi_j(\varepsilon_{i-1}') < r_2 \le \Pi_j(\varepsilon_i'), \tag{2.3.9}$$

where r_2 is a random number distributed between (0, 1). The probabilities are precomputed at the beginning of each iteration. Once the collision partner velocity, $\vec{v}'$, is chosen, the impact parameter for 90° scattering, b_0, is calculated using the formula [20],

$$b_0 = e^2 / \left(2\pi\varepsilon_0 m_e g^2\right), \tag{2.3.10}$$

where m_e is the electron mass, $g = \left|\vec{v}_0 - \vec{v}'\right|$ is the relative speed between the collision partners, and ε_0 is the vacuum permittivity. The collision event is ignored if $\cos(\theta) < b_0 / \lambda_D$, where θ is the angle between the velocity of the pseudo-electron and its collision partner and λ_D is the local Debye length. This approach may not represent very small angle scattering very well, however $f_b(\varepsilon)$ is not significantly affected at the energies that determine inelastic rate coefficients. If $\cos(\theta) < b_0 / \lambda_D$ is found to be false, the probability of an e-e collision during the current time step Δt is determined from

$$P_{ee}(g, \Delta t) = n_j \sigma_{ee}(g) g \Delta t, \tag{2.3.11}$$

where n_j is the density of electrons in the j^{th} spatial bin obtained from the FKPM, and the momentum transfer Coulomb cross section, $\sigma_{ee}(g)$, is [21]

$$\sigma_{ee}(g) = 4\pi b_0^2 \left[1 + \ln\left(\lambda_d / b_0\right)^2\right]^{1/2}. \tag{2.3.12}$$

This procedure is justified if, $P_{ee}(g, \Delta t) << 1$ for the conditions of interest. This is the case for virtually all conditions of this thesis. The collision event takes place if $P_{ee}(g, \Delta t) \geq r_3$. If a collision does occur, then post collision a relative velocity $\vec{g}'$ is randomly determined such that [22]

$$
\begin{aligned}
g_z' &= \pm |\vec{g}| r_4, \\
g_x' &= |\vec{g}| \sqrt{1-r_4^2}\cos(2\pi r_5), \\
g_y' &= |\vec{g}| \sqrt{1-r_4^2}\sin(2\pi r_5),
\end{aligned}
\tag{2.3.13}
$$

where g_z' is positive or negative if g_z is positive or negative. The final velocity of the incident pseudoparticle, $\vec{v}_f$, is updated by eq. 2.3.14,

$$
\begin{aligned}
\vec{v}_f &= \vec{v}_R + 0.5\vec{g}, \\
\vec{v}_R &= 0.5(\vec{v}' + \vec{v}_0).
\end{aligned}
\tag{2.3.14}
$$

The collision partner's change in velocity in the stored distribution function is disregarded. At the end of a call to the eMCS, $f_b(\varepsilon, \vec{r})$ are used to compute electron impact rate coefficients $k_j(\vec{r})$ for collision process j,

$$
k_j(\vec{r})[cm^3 s^{-1}] = \sum_{i=1} f_{bi}(\vec{r})\sigma_j(\varepsilon_i)\left(\frac{2\varepsilon_i}{m_e}\right)^{1/2}\Delta\varepsilon_i . \tag{2.3.15}
$$

The FKPM holds the values of $k_j(\vec{r})$ constant between calls to the eMCS. The source function resulting from the rate coefficient is then

$$
S_j(\vec{r})[cm^{-3}s^{-1}] = n_e(\vec{r})k_j(\vec{r})N_j(\vec{r}), \tag{2.3.16}
$$

for electron density n_e and heavy particle collision partner density N_j.

The EEDs of secondary electrons that are first emitted from surfaces and accelerated by sheaths, $f_s(\varepsilon, \vec{r})$, are obtained by a similar process. The flux striking surfaces of energetic particles (ions, photons, excited states) of type j, $\vec{\phi}_j(\vec{r})$, is obtained from the FKPM instead of seeding electrons in the bulk plasma. The total rate of secondary electron emission, R_S (1/s), is obtained from

$$R_S = \sum_k R_{Sk}$$
$$R_{Sk} = \sum_j \gamma_j \vec{\phi}_j(\vec{r}_k) A_k \quad , \tag{2.3.17}$$

where the summation is over species j having secondary electron emission coefficient γ_j and surface locations k having surface area A_k. Secondary electrons are then randomly launched perpendicularly to the surface with an energy of 4 eV from spatial location k in proportion to R_{Sk} / R_S. The number of secondary electrons to be launched is preselected. The statistical weighting of the particle, w, has units of current or particles/s. Then particle trajectories are tracked and statistics to produce $f_s(\varepsilon, \vec{r})$ are collected in the same manner as for $f_b(\varepsilon, \vec{r})$. Since w has units of particles/s, the distribution functions $f_s(\varepsilon, \vec{r})$ are normalized,

$$\sum_j F_{ij} = \sum_{i,j} f_{sij} \varepsilon_i^{\frac{1}{2}} \Delta\varepsilon_i \Delta \mathrm{V_j} \quad , \tag{2.3.18}$$

where $f_{sij} = f_s(\varepsilon_i)$, ε_i is the energy of the secondary electron in bin i, $\Delta\varepsilon_i$ is the width of the energy bin, and ΔV_j is the volume of the cell at location j. With this normalization, $f_s(\varepsilon, \vec{r})$ have units of electrons/cm^3-eV-s.

Pseudoparticle trajectories are followed until the particle collides with a surface or falls below a specified energy, typically the lowest electronic excitation threshold, ε_T. Once one of these conditions occurs, the pseudoparticle is removed from the simulation. Pseudoparticles that are emitted originally and have their energy fall below ε_T have their weightings summed into a current source, $Q_e(\vec{r})$ (C/cm^3-s), using eq. 2.3.19,

$$\sum_{j'=j,neighbors} \left[Q_{j'} \rightarrow Q_{j'} + \frac{qw\eta_{jj'}}{\Delta V_{j'}} \right], \tag{2.3.19}$$

where Q_j is the current source for location j having volume ΔV_j. Surface emitted secondary electrons act as a source of electrons for the electron continuity equation in the fluid simulation. This source is provided by $Q_e(\vec{r})$. This source appears as net charge injection in the solution of Poisson's equation through the change in electron density. This is because this source does not also appear in a positive ion continuity equation. A rate of surface charging $Q_{se}(\vec{r})$ (C/cm^2-s), which comes from secondary electrons striking a surface, is calculated from a summation similar to that for $Q_e(\vec{r})$, and then included in the continuity equation for surface charging in the fluid modules.

Electron impact source functions for secondary electrons, eq. 2.3.20, are transferred back to the FKPM instead of rate coefficients, since $f_s(\varepsilon,\vec{r})$ is ultimately normalized to the magnitude of the secondary electron current, R_S.

$$S_{ej}(\vec{r})[cm^{-3}s^{-1}] = N_j(\vec{r})\sum_{i=1} f_{si}(\vec{r})\sigma_j(\varepsilon_i)\left(\frac{2\varepsilon_i}{m_e}\right)^{1/2}\Delta\varepsilon_i . \qquad (2.3.20)$$

The values of $S_{ej}(\vec{r})$ are held constant in the FKPM between calls to the eMCS.

2.4 Fluid Kinetics Module

In the FKPM, the densities, temperatures, and fluxes of all neutral and ionic species are determined by solving continuity, momentum and energy equations for all neutrals and ions. The density and flux of electrons are also calculated in the FKPM, while the electron temperature is determined from the EEDF calculated in the eMCS. Poisson's equation is also solved for in the FKPM to calculate the electrostatic potential and field as a function of position and phase. The FKPM also produces rate coefficients and source functions for heavy particle reactions. The continuity equation solved for neutral and ion transport is

$$\frac{\partial N_i}{\partial t} = -\nabla \cdot \vec{\phi}_i + S_i, \tag{2.4.1}$$

where N_i is the density of species i, $\vec{\phi}_i$ is the flux of the species, and S_i is the source due to gas phase collision processes. The flux of neutrals and ions can be determined multiple ways. A drift-diffusion method with and without including the effects of magnetic fields can be used. Neither option is used to obtain the results in this thesis. Another method is to solve the momentum equation

$$\begin{aligned}\frac{\partial \vec{\phi}_i}{\partial \mathrm{t}} = \frac{\partial (N_i \vec{v}_i)}{\partial t} = &-\frac{1}{m_i}\nabla(kN_iT_i) - \nabla \cdot (N_i \vec{v}_i \vec{v}_i) + \frac{q_i N_i}{m_i} \times (\vec{E}_S + \vec{v}_i \times \vec{B}) \\ &-\nabla \cdot \overline{\overline{\mu}}_i - \sum_j \frac{m_j}{m_i + m_j} N_i N_j (\vec{v}_i - \vec{v}_j)\nu_{ij},\end{aligned} \tag{2.4.2}$$

where $\vec{v}_i$ is velocity, m_i is the mass, T_i is temperature, E_S is the electrostatic field, $\overline{\overline{\mu}}_i$ is the viscosity tensor (used only for neutrals), and ν_{ij} is the collision frequency between species i and j. An energy equation, seen in eq. 2.4.3, can also be solved for in addition to the momentum equation

$$\begin{aligned}\frac{\partial (N_i c_i T_i)}{\partial t} = &\nabla \cdot \kappa_i \nabla T_i - P_i \nabla \cdot \vec{v}_i - \nabla \cdot (N_i \vec{v}_i \varepsilon_i) \\ &+ \frac{N_i q_i^2 \nu_i}{m_i(\nu_i^2 + \omega^2)} E_\Theta^2 + \frac{N_i q_i^2}{m_i \nu_i} E_S^2 \\ &+ \sum_j 3\frac{m_{ij}}{m_i + m_j} N_i N_{ji} R_{ij} k_B (T_j - T_i) \pm \sum_j 3 N_i N_j R_{ij} k_B T_j .\end{aligned} \tag{2.4.3}$$

where c_i is the heat capacity in a relation of $\varepsilon_i = c_i T_i$, κ_i is the thermal conductivity, P_i is the partial pressure, ν_i is the momentum transfer collision frequency, E_Θ is the rf electric field, ω

is the rf frequency, $m_{ij} \equiv m_i m_j / (m_i + m_j)$ is the reduced mass, k_B is Boltzmann's constant, and R_{ij} is the rate coefficient for formation of the species by collisions between heavy particles. The first three terms on the RHS of eq. 2.4.3 are power transfer by thermal conductivity, compressive heating, and advective transport. The next two terms are additional heating contributions for ions from both the electromagnetic and electrostatic fields. The last two terms are heating contributions from elastic collisions and charge exchange collisions (either positive or negative contribution). In this thesis the momentum equation along with the energy equation is solved in order to obtain the flux of neutrals and ions.

For electrons, only the continuity equation is solved in the FKPM. The flux is obtained using a drift-diffusion approximation. The electron energy is obtained from the eMCS. Using the conventional drift-diffusion approximation, the electron flux is calculated by eq. 2.4.4

$$\vec{\phi}_e = q_e n_e \overline{\overline{\mu}}_e \cdot \vec{E} - \overline{\overline{D}}_e \cdot \nabla n_e , \tag{2.4.4}$$

where n_e is density of electrons moving in the electric field $\vec{E}$ and having tensor mobility $\overline{\overline{\mu}}_e$, tensor diffusivity $\overline{\overline{D}}_e$, and charge q_e. In the absence of a static magnetic field, the tensor mobility and diffusivity become equal to their isotropic values.

Due to the tight coupling of electrostatic fields to the densities of charged particles, Poisson's equation is solved within the FKPM. There are several ways in which Poisson's equation can be solved. It can be solved for explicitly, semi-implicitly, semi-implicitly with implicit electrons and predictor-corrector ions, semi-implicitly with implicit electron densities and fluxes, with a semi-implicit ambipolar approximation, and using any of the previous options with a sheath model. The results of this thesis are obtained by using the semi-implicit form of Poisson's equation given by

$$
\begin{aligned}
&-\nabla\cdot\left(\varepsilon\nabla\Phi_S\left(t+\Delta t\right)\right)\\
&=\sum_i q_i\left(N_i(t)-\Delta t\nabla\cdot\phi_i\left(\Phi_S\left(t+\Delta t\right)\right)+S_i(t)\right)\\
&+\rho_S(t)-\Delta t\nabla\cdot\left(\sum_i q_i\phi_{Si}\left(\Phi_S\left(t+\Delta t\right)\right)-\sigma_M\nabla\Phi_S\left(t+\Delta t\right)\right),
\end{aligned}
\tag{2.4.5}
$$

where Φ_S is the electrostatic potential, ε is the local permittivity, ρ_S is the charge density in or on non-plasma materials, ϕ_{Si} is the flux of charged species incident onto surfaces in contact with the plasma i, N_i is the density of species i, q_i is the electrical charge of species i, and σ_M is the material conductivity. This method solves for the potential at a future time $t+\Delta t$. The charge densities are set to be equal to their current values at time t plus some small fraction of their predicted values at time $t+\Delta t$ based on the divergence of their fluxes.

When ion fluxes are derived by solving their momentum equations instead of using a drift-diffusion equation, the direct semi-implicit solution for the ion fluxes with Φ_S is lost. $\phi_{ion}\left(t+\Delta t\right)$ is no longer an easily quantified function of Φ_S and this makes numerically constructing Jacobian elements difficult. When there are many ion species, it becomes computationally burdensome to include ion momemtum equations in the matrix for semi-implicit solutions of electron and ion densities and Φ_S. However, even an approximate prediction for the ion densities at future times $N\left(t+\Delta t\right)$, has been found to provide additional stability and allow for larger time steps to be taken. This prediction is provided by recording a short past history of fluxes and source functions and numerically deriving derivatives. An example of this is,

$$
N\left(t+\Delta t\right)=N\left(t\right)+\Delta t\left(-\nabla\cdot\left(\phi\left(t\right)+\Delta t\frac{d\phi(t)}{dt}\right)+S\left(t\right)+\Delta t\frac{dS(t)}{dt}\right),
\tag{2.4.6}
$$

where $d\phi(t)/dt$ and $dS(t)/dt$ are derived from a past history of fluxes and source functions respectively.[1]

There are two different methods that may be used to solve the matrices obtained from implementing the various options mentioned above. Which method is most appropriate depends on the simulation. The presence or absence of a magnetostatic field has a significant influence on which method is most appropriate. In a case where finite differences are being used for discretization on a structured mesh in the absence of a magnetostatic field, the numerical molecule is a five-point molecule with five nearest neighbor points.[1] Each of these points are connected to the center point by a coefficient containing transport coefficients and geometrical information.[1] In this situation, the iterative successive-over-relaxation (SOR) method is considered to be a fast, efficient method of solving Poisson's equation. In the presence of a magnetostatic field, the numerical molecule becomes a nine-point molecule that contains next-nearest neighbors that do not share a coefficient with the center point. A sparse matrix technique is preferred in these conditions. No matter the choice of method, the construction of the matrices to implement the options mentioned above and the method of solving those matrices should be independent.

In the FKPM, acceleration techniques are used to speed the rate convergence of computed quantities. The cycle averaged time rate of change of densities is recorded over a period of many rf cycles during execution of the FKPM. The integration is then paused and the densities of species are increased (or decreased) proportional to these average rates and the integration is then restarted. As different rates of acceleration are applied to different species depending on their derivatives, it is difficult to assign a precise time interval for which the densities are projected into the future. The net charge density may not be conserved through the

acceleration process, due to different acceleration rates for different species. In each cell in the volume and on surfaces, the charge density is recorded before acceleration. This is to stop unphysical transients in the plasma potential and the charging of surfaces from occurring. The charge density in each cell is set to be the same after acceleration as before by adjusting the electron density.

2.5 Plasma Chemistry Monte Carlo Module

The PCMCM is a 3v-3d (three velocity components, three dimensions) Monte- Carlo simulation of the trajectories, including collisions, of plasma species from the gas phase to reactor surfaces. The PCMCM is used to calculate the energy and angular distributions (EADs) of plasma species hitting a surface. The PCMCM launches pseudoparticles representing ions and neutral species at randomly chosen times during the rf period. By default, the PCMCM loops through every (r,z) mesh cell in the plasma region of the reactor, and integrates the trajectory of pseudoparticles launched one at a time from the current (r,z) mesh cell until the particle is lost. This can be through either a gas phase collision or by hitting a surface. If the pseudoparticle hits a user-specified surface for which the EADs are to be calculated, the EAD of the pseudoparticle is recorded. The angles are recorded relative to the local normal.

Ion transport in the time varying sheath is resolved by dynamically choosing the appropriate time steps. The time step is chosen to be no larger than a fraction of the rf cycle (typically 0.01) or the time to cross a fraction of a computational mesh cell (typically 0.5 far from the sheath and 0.02 in the sheath). The launching of the pseudoparticles is done in a loop until all particles have been launched and removed from the system. The number of pseudoparticles to be launched at a given (r,z) position is weighted by the spatially dependent source function of the plasma species between a user defined minimum and maximum value. As

part of the work discussed in Chapter 4, the PCMCM is upgraded to allow for a stencil to be defined by the user, which would confine the launching of pseudoparticles in the PCMCM to within a specified range in r and z.

The source functions for all heavy particle plasma species (ions and neutrals) as well as the electric fields in the reactor are calculated in the FKPM as a function of position and are exported to the PCMCM. The exported electric fields are used to integrate the trajectories of ions. The initial velocities of the plasma species are randomly chosen from a Maxwell-Boltzmann distribution having the temperature of that species as computed by the FKPM. Trajectories of pseudoparticles representing ions are integrated by interpolating electric fields in space and time. Null collision techniques are used in the selection of collision times and mean free paths for individual particles. The maximum collision frequency for each PCMCM species, i, over the entire computational domain is determined by equation 2.5.1 below,

$$\begin{aligned} \nu_{im} &= \sum_j \nu_{ij}, \\ \nu_{ij} &= \max\left(\left(v\sigma_j(v)\right)_m N_{jm}\right), \end{aligned} \tag{2.5.1}$$

where the sum is over collisions j, $(v\sigma_j(v))_m$ is the maximum product of the particle speed and cross section for collision j at that speed, and N_{jm} is the maximum density of the collision partner in the computational domain. The randomly chosen time to the next collision is then,

$$t_c = t_0 - \frac{1}{\nu_{im}} \ln(1-r), \tag{2.5.2}$$

where t_0 is the current time and r is a random number distributed on (0,1). Null collision techniques are used in a similar way as in the eMCS to determine if a collision has occurred. If the time to the next collision is reached and a null collision is determined to have occurred the particle's trajectory is not adjusted, the time to the next collision is recalculated based on eq 2.5.2,

and the particle trajectory continues to be integrated. The pseudoparticles in the PCMCM are particle representations of the same plasma species that are represented as fluids in the FKPM. Thus, the collisional processes undergone by the pseudoparticles are based on the reaction mechanisms used by the FKPM.

IEDs can be obtained for plasma systems operated under both continuous (cw) and pulsed conditions. Under cw conditions, the electric field spatial profile on the last iteration is stored and used to integrate the ion trajectories assuming that the properties of the plasma, including the electric field, are now at steady state. Under pulsed conditions IEDs can be obtained in two ways. The first way is that for each iteration during a pulse, IEDs are obtained as if the current iteration is the last iteration in a cw plasma, and then averaged together. If the source function of an ion is small, fewer pseudoparticles will be launched and the effect of the IED of that iteration on the total averaged IED will be small. If the source function of an ion is less than or equal to 0 for the current iteration and position, no pseudoparticles for that ion are launched at that position for the current iteration. A problem with this method is that it does not accurately account for the effect of the ion transit time. While a large number of particles may be generated during the plasma on period of a pulse, many of those particles may actually reach the sheath during the plasma off period of the pulse. Thus there can be significant ion bombardment during iterations in the off period of the pulse, even though the source functions during these iterations are small or even negative.

In order to obtain the results of Chapters 4 and 5, the PCMCM is modified to take into account the effect of ion transit time on when a particle reaches the sheath, and thus the energy with which the ion actually bombards the surface. In these chapters, time averaged IEDs are obtained for periodically pulsed plasma with a fixed pulse repetition frequency (PRF).

"The electric fields that are used in advancing the trajectories of the particles are periodically stored during the pulsed cycle, and these electric fields are interpolated as a function of position and time during integration of the ion trajectories. Depending on the PRF and duty cycle of the applied power, T_e and ionization sources may significantly vary over the pulsed cycle. For these conditions, electron impact ionization sources for ions are also recorded as a function of space and time. Pseudoparticles, representing ions in the PCMCM, are then launched during the pulse period from locations and phase in the period in proportion to these time dependent ionization sources. In the event that the transit time for an ion from its site of creation to a surface is longer than the pulse period, the electric fields are repeated for additional pulsed periods until the ion strikes a surface or is lost through a gas phase collision process."[23]

2.6 Figures

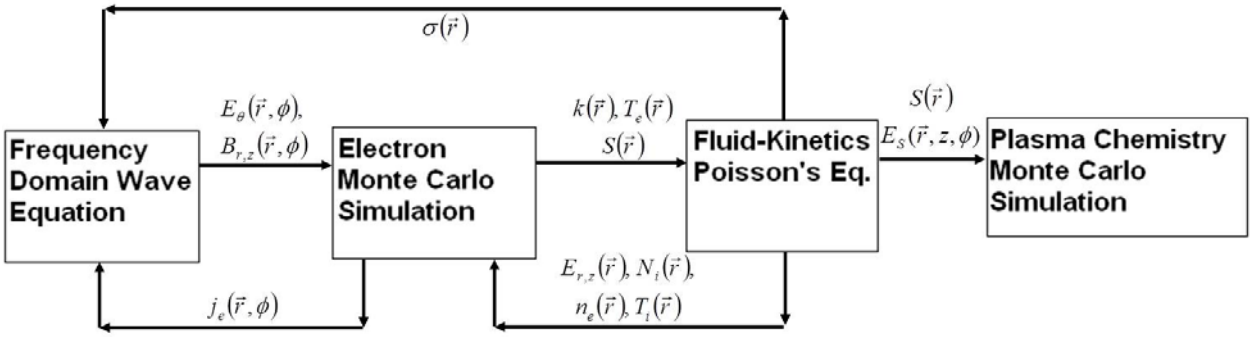

Figure 2.1 Flow chart of HPEM showing information exchange between the modules used for this thesis.

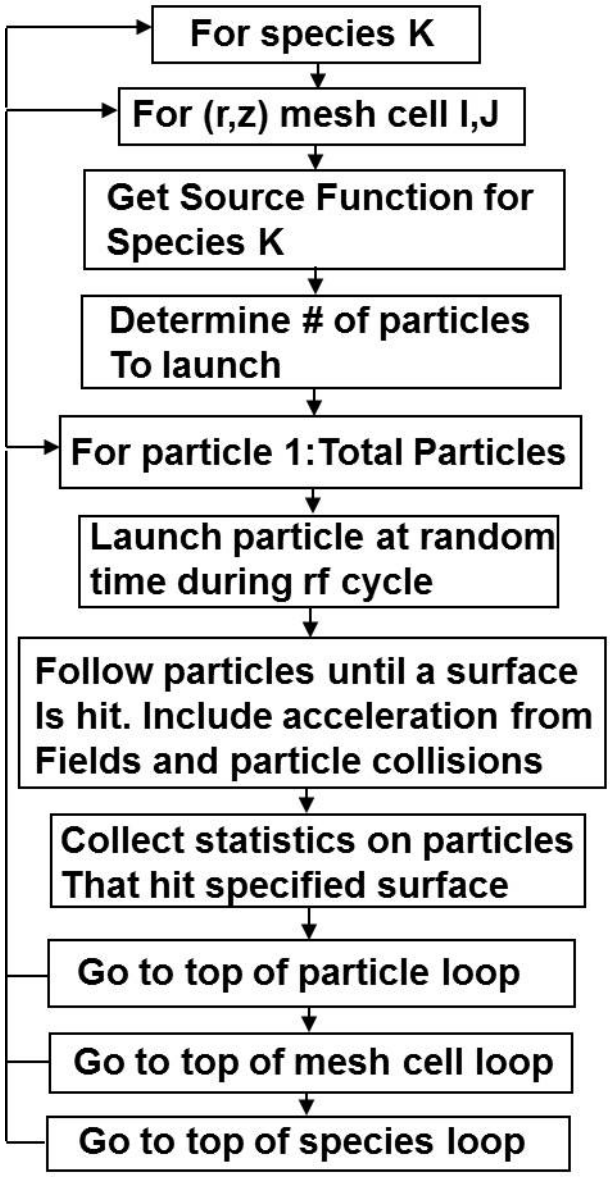

Figure 2.2 Flowchart of PCMCM showing process by which statistics for IEDs are collected.

2.7 References

1. M. J. Kushner, J. Phys. D: Appl. Phys. **42**, 194013 (2009).
2. A. Agarwal and M. J. Kushner, J. Vac. Sci. Technol. A **23**, 1440 (2005).
3. A. Agarwal and M. J. Kushner, J. Vac. Sci. Technol. A **26**, 498 (2008).
4. A. Agarwal, P. J. Stout, S. Banna, S. Rauf, K. Collins, J. Vac. Sci. Technol. A **29**, 011017 (2011).
5. A. Agarwal, P. J. Stout, S. Banna, S. Rauf, K. Tokashiki, J.-Y. Lee, K. Collins, J. Appl. Phys. **106**, 103305 (2009).
6. S. Banna, A. Agarwal, G. Cunge, M. Darnon, E. Pargon, and O. Joubert, J. Vac. Sci. Technol. A **30**, 040801 (2012).
7. W. Z. Collison, T. Q. Ni, and M. S. Barnes, J. Vac. Sci. Technol. A **16**, 100 (1998).
8. S. Tinck, W. Boullart, and A. Bogaerts, J. Phys. D: Appl. Phys. **41**, 065207 (2008).
9. S.-H. Song and M. J. Kushner, J. Vac. Sci. Technol. A **32**, 021306 (2014).
10. J. Shoeb and M. J. Kushner, J. Vac. Sci. Technol. A **30**, 041303 (2012).
11. M. Wang and M. J. Kushner, J. Vac. Sci. Technol. A **29**, 051306 (2011).
12. P. Subramonium and M. J. Kushner, J. Vac. Sci. Technol. A **22**, 534 (2004).
13. P. Subramonium and M. J. Kushner, Appl. Phys. Lett. **85**, 721 (2004).
14. P. Subramonium and M. J. Kushner, J. Appl. Phys. **96**, 82 (2004).
15. Y. Yang and M. J. Kushner, J. Vac. Sci. Technol. A **25**, 1420 (2007).
16. J. Shoeb and M. J. Kushner, J. Vac. Sci. Technol. A **47**, 1289 (2009).
17. A. Agarwal and M. J. Kushner, J. Vac. Sci. Technol. A **27**, 37 (2009).
18. A. V. Vasenkov and M. J. Kushner, Phys. Rev. E **66**, 066411 (2002).
19. S.-H. Song and M. J. Kushner, Plasma Sources Sci. Technol. **21**, 065009 (2012).
20. M. Mitchner, C. H. Kruger, *Partially Ionized Gases* (Wiley, New York, 1973), p. 265.
21. V. Vahedi, M. A. Lieberman, G. DiPeso, T. D. Rognlien and D. Hewett, J. Appl. Phys. **78**, 1446 (1995).

22. G. A. Bird, *Molecular Gas Dynamics and the Direct Simulation of Gas Flows* (Oxford University Press, New York, 1994).

23. M. D. Logue, H. Shin, W. Zhu, L. Xu, V. M. Donnelly, D. J. Economou, and M. J. Kushner, Plasma Sources Sci. Technol. **21**, 065009 (2012).

Chapter 3 Electron Energy Distributions and Source Functions in Ar/N_2 Inductively Coupled Plasmas Using Pulsed Power For a Variety of Duty Cycles, Pressures, and Frequencies

3.1 Introduction

Optimization of plasma materials processing ultimately requires control of the flux of reactive species (radicals, ions, photons) to surfaces. Control of these species is greatly facilitated by controlling the source functions resulting from electron collisions with feedstock gases and their dissociation products. This control is a direct consequence of controlling the electron energy distribution (EED).[1] In steady state or continuous wave (cw) plasmas, such as low pressure inductively coupled plasmas (ICPs), the rate of ionization, as determined by the EED, must exactly balance the rate of loss of charged particles, either in real-time or averaged over relatively short radio-frequency (rf) cycles. (Short in this case, refers to the rf period being much smaller than the diffusion or attachment time for loss of electrons, or the time for electron energy loss.) For a given gas mixture, flow rate, power deposition, frequency, and geometry, there is usually a single EED that will provide this balance between electron sources and losses. (EEDs are, in fact, spatially varying in the plasma – in this context, I refer to the spatial average.)

Pulsed plasmas provide a means to broaden the parameter space available to customize EEDs. In a pulsed plasma, the power is applied over a fraction (the duty cycle, DC) of a repetitively pulsed cycle (the pulse repetition frequency or PRF). In pulsed plasmas, the balance between sources and losses need only be maintained over the pulsed period, which provides additional parameters to optimize the EED, such as DC and PRF. The pulsed period can be

commensurate to or longer than the time for electron loss by diffusion, attachment, or energy loss. Several studies have investigated the effect of pulsed power on radical density formation in electron cyclotron resonance (ECR) plasmas [2-4] and ICPs [5]. ICPs, as used for etching and deposition, are particularly attractive for EED control through pulsing. The smaller influence of surface associated processes, such as secondary electron emission and acceleration by sheaths, enables a more direct correlation between power deposition and electron heating. Substrate biases for ion acceleration applied to ICPs operating in high plasma density mode have little effect on the EEDs due to small amounts of electron heating produced by the thin sheaths.

Kortshagen *et al*. measured the spatial variation of EEDs in an argon ICP under continuous wave (cw) conditions at pressures of 5 – 40 mTorr.[6] They compared the EEDs to theoretical results from a 1D model. They found that with increasing pressure there was a change in the shape of the EED from concave to convex in the elastic energy range ($\varepsilon < 11.6$ eV) and that the EEDs displayed non-local behavior. Sing and Graves measured EEDs in cw ICPs sustained in Ar, N_2, Ar/N_2, and other gases.[7] In Ar, they found that varying power while keeping pressure constant at 10 mTorr had little effect on the EEDs. When keeping the power constant at 300 W and varying pressure from 2-40 mTorr, they found the EEDs to be non-Maxwellian at all pressures, although for 10-40 mTorr, the EEDs were nearly Maxwellian below the inelastic collision thresholds. The EEDs were two-temperature distributions above 10 mTorr and three-temperature distributions at 2 mTorr. In N_2 ICPs at a constant power of 450 W, a decrease in the electron energy probability functions (EEPFs) around 3 eV was observed as the pressure was increased from 10-100 mTorr due to the increased importance of energy loss due to vibrational excitation. In Ar/N_2 discharges, increasing the Ar fraction reduces the EEPF dip around 3 eV and reduces the propensity for a two-temperature distribution.

Malyshev and Donnelly investigated the temporal dynamics of electron temperature (T_e), electron density (n_e), and the EED in a pulsed Cl_2 ICP with an rf substrate bias.[8] They found that during the afterglow of the power pulse, the rf bias on the substrate did affect the EEDs. As the plasma density decreased during the afterglow due to diffusion and attachment, the sheath thickness at the substrate increased. The widening sheath increased the rate of stochastic electron heating which then increased the rate of heating of the EED. When the ion density decayed to values normally associated with capacitively coupled plasmas (CCPs), the EEDs became indistinguishable from those of cw reactive ion etching (RIE) plasmas.

Hebner and Fleddermann investigated the effect of peak rf power, duty cycle, and PRF on electron density and plasma potential in pulsed Ar and Cl_2 ICPs.[9] They found that the peak electron density initially increased with duty cycle before decreasing above 30%. This is due to a balance between the amount of power being deposited into the plasma and the time it takes for the n_e source and loss mechanisms to come into equilibrium. Increasing rf power led to larger peak n_e values, while increasing pulse repetition frequency (PRF) caused n_e to decay to lower values in the plasma afterglow and a greater dynamic range in n_e during the pulse. Increased duty cycle was also found to cause the peak plasma potential to decrease due to a higher residual n_e at the beginning of the pulse shielding the bulk plasma from the applied rf potential.

Kimura and Ohe investigated the effect of pressure on the EEDs in Ar discharges in a planar ICP system.[10] They found that for a cw power of 50 W the EED had a three-temperature distribution at 5 mTorr of pressure due to the depletion of high-energy electrons at inelastic thresholds.[10] The EED had a bi-Maxwellian structure below the first inelastic threshold. The EEDs at pressures higher than 10 mTorr were two-temperature distributions. The slope of the tail of the EED is dominated by inelastic collisions as opposed to electron-electron

collisions, which results in the EED having two temperatures for the bulk and tail of the EED. Maresca, Orlov, and Kortshagen experimentally investigated the diffusive cooling of electrons and EEDs in a planar, pulsed Ar ICP.[11] They attributed observed decays in the tail of the EEDs to both inelastic collisions and to loss of electrons having energy greater than the sheath potential to walls $\rightarrow$ diffusion cooling.

Godyak *et al*. investigated the effect of power, pressure, and rf frequency on EEDs and plasma parameters in an Ar ICP.[12] At 100 mTorr the plasma is collisionally dominated and the EED at all powers appears almost Maxwellian in the elastic energy range and is depleted above the inelastic energy threshold ($\approx$11.6 eV). This appears as a two-temperature distribution. At 10 mTorr, a three-temperature structure is observed for the EEPF at low power, with a well-defined low energy bump due to non-local electron kinetics in low pressure discharges with moderate plasma density. The EEPFs move toward a two-temperature distribution with increasing power. At lower pressure, 1-10 mTorr, the rf frequency had a noticeable effect on the EEPF at all powers, with reduced electron heating at higher frequencies due to the reduced skin depth of the electromagnetic field.

Godyak investigated non-equilibrium EEDs in ICPs and discussed ways to control electron temperatures, T_e, and thus EEDs.[13] He found that there may be a two-temperature distribution in the EED due to anomalous skin effects where the RF current is not a local function of the rf field. One such effect is selective, collisionless heating of the faster and hotter electrons that cross the sheath in a fraction of the rf period, the selective nature of this heating can lead to two-temperature distributions. In low pressure ICPs having an anomalous skin effect the effective electron temperature was found to have a strong dependence on frequency. This

frequency effect is reduced as the plasma density increases and the EED becomes more Maxwellian due to increased collisions.[13]

Another method to control T_e, and thus EEDs, as discussed by Godyak, is pulsing of the discharge power, which decouples the electron heating and electron energy loss processes. During repetitive pulsing, at the beginning of the activeglow (power pulse-on time) T_e initially overshoots the steady state value of T_e, before decaying to that value. This spike in T_e is due to the ICP power being dissipated into a smaller electron density than the activeglow steady state density. The T_e must also exceed the value for which ionization balances losses in order to increase the electron density during the pulse. The activeglow steady state of T_e may be different from the cw mode steady state value obtained if pulse-period-average (PPA) power was applied continuously. During the afterglow (power pulse-off time) T_e quickly decays below the cw steady state value due to collisional energy losses and diffusion cooling. This phenomenon has a pressure dependence, as lower pressures will result in higher T_e during the pulse-on time as well as a faster cooling rate during the pulse-off time due to diffusion cooling. At lower pressures the electron mean free path is longer, which reduces energy loss from collisions during the pulse-on time and allows higher energy electrons to diffuse to the walls faster.[13]

In this chapter, a computational investigation of EEDs and source functions in a pulsed Ar/N_2 planar ICP discharge is presented. This gas mixture is chosen as there are collisional energy loss reactions at low (vibrational excitation), intermediate (electron excitation) and high (ionization) energies. The effect of pulsed power for various duty cycles and pressures on EEDs and source functions for $N_2(v = 1)$, $N_2(A)$, and Ar^+ through direct electron-impact reactions is examined. The threshold energies of these reactions are 1.3 eV, 6 eV, and 16 eV, which are intended to be representative of low, mid, and high threshold processes, respectively. $N_2(v = 1)$

represents the first vibrational state of N_2, and $N_2(A)$ represents the first electronic metastable state of N_2, the $N_2\left(A^3\Sigma_u^+\right)$ state.

All results are for plasmas sustained in argon/nitrogen (Ar/N_2=80/20). The species consist of Ar (ground state), Ar*, Ar**, Ar***, Ar^+, N_2 (ground state), $N_2(v)$, N_2^*, N_2^+, N (ground state), N*, N^+, and electrons. Ar* represents the combined metastable states of the $Ar(3p^54s)$ manifold [$Ar(1s_5)$, $Ar(1s_3)$] and Ar** represents the combined radiative states [$Ar(1s_4)$, $Ar(1s_2)$]. Ar*** is a lumped state representing $Ar(3p^54p)$ and higher states in the excited state manifold. Radiation trapping of the Ar** state is included. $N_2(v)$ represents the combined vibrational states of N_2, and N_2* represents the combined electronic states of N_2. N* represents the combined electronic states of atomic nitrogen, $N(4s^22d)$ and $N(4s^22p)$.

3.2 Description of the Reactor and Experiment

A schematic of the ICP reactor used in the computational investigation is shown in Fig. 3.1. The plasma is sustained in a 25 cm diameter reactor, 16.5 cm tall with a 3-turn planar coil on top of a dielectric window. Gas is injected through a cylindrical nozzle at the top underneath the center coil of the ICP and pumped annularly at the bottom. Computed plasma parameters [electron temperature (T_e), electron density (n_e), and electron source function (S_e)], EEDs, and source functions for $N_2(v=1)$, $N_2(A)$, and Ar^+ are discussed below. When comparing EEDs or source functions for different heights, two or more of the heights indicated in Fig. 3.1 are used. In most cases, comparisons will be made between the heights of 11.5 cm and 5.5 cm, inside and outside the electromagnetic skin depth, respectively. In all cases the pulse-period-average (PPA) power is 300 W, the PRF = 20 kHz, the ICP frequency is 10 MHz, and the flow rate is 100 sccm.

3.3 Effect of Pulsed Power on Plasma Parameters

Plasma parameters during a pulse period of the ICP power are first discussed for a duty cycle of 30% and pressure of 5 mTorr. The spatial profiles for n_e, T_e, and net electron impact ionization source, S_e, for different times during the pulse period are shown in Figs. 3.2, 3.3, and 3.4. T_e at a radius of 5.9 cm and heights of 11.5 cm (in the skin depth) and 5.5 cm (below the midplane) as a function of time is shown in Fig. 3.5. The densities of plasma species [N_2(v = 1)], [N_2(A)], [Ar^+], and [e] at a radius of 5.9 cm and heights of 11.5 cm (in the skin depth) and 5.5 cm (below the midplane) as a function of time for a pressure of 5 mTorr is shown in Fig. 3.6.

At the start of the power-on period, T_e and S_e first increase near the coil underneath the nozzle. The ICP power is deposited within the skin depth of the rf field (≈1 – 2 cm) near the coils and only those electrons located in the skin depth are initially heated. At 5 mTorr, the mean-free-path for electron energy loss is ≈20 cm, and so the skin depth is anomalous, that is partly non-collisional. With the exception of the initial spike in T_e (discussed below), T_e in the skin depth layer is 5 – 6 eV. These higher energy electrons then diffuse through the chamber, undergoing collisions and producing ionization. The calculation of T_e is dominated by the more numerous low energy electrons, while ionization is dominated by the sparse high energy electrons, which have longer mean-free-paths. As a result, S_e appears to extend further from the skin depth than does T_e.

There is a spike in T_e near the coils at the start of the pulse to as high as 12 eV, a phenomenon typically called *overshoot*. At the beginning of the pulse, power is dissipated into a smaller inventory of electrons, which then elevates their temperature above the quasi-steady state value, 3.5 – 4 eV. In fact, T_e must at some point exceed the quasi-steady state value in order to increase the plasma density from its prepulse value. The local spike in S_e is to 8×10^{16} $cm^{-3}s^{-1}$,

compared to a quasi-steady state value of 10^{16} $cm^{-3}s^{-1}$. This spike in both T_e and S_e produces a local maximum in n_e under the coils of 2×10^{11} cm^{-3}. The modulation in the peak value of n_e during the pulse period is a factor of 2. The modulation in T_e is significantly greater, requiring only 5 μs to decrease to 0.5 eV when power is terminated, a value that is then sustained largely by superelastic electron heating in the afterglow.

When the ICP power is turned off, the rapid decay in T_e leads to a regime where the electron loss through diffusion to the walls and recombination is larger than electron generation through electron impact ionization. This results in S_e transitioning from positive to negative – a net source to a net loss. The loss is dominated by dissociative recombination of N_2^+. The rate coefficient for dissociative recombination scales as $T_e^{-0.5}$, which is not a strong temperature dependence compared to ionization. Therefore, the negative S_e largely follows the plasma density during the recombination phase of the pulse cycle.

When the ICP power is turned on, there is an initial overshoot of both T_e (at all pressures), followed by a decay to a quasi-steady state value, as shown in Fig. 3.5. At pressures of ≤10 mTorr, the initial electron density is low enough that there is a large overshoot in T_e (9 – 12 eV) before the temperature begins to settle toward a steady state value. There is not a strong overshoot at higher pressures due to there being a smaller modulation in the electron density due to the lower rate of electron loss by diffusion during the afterglow. The lower steady state T_e and longer rise time with increasing pressure is expected due to an increased rate of energy loss through electron-electron collisions.

The modulation of the different plasma species shown in Fig. 3.6 is a reflection of the modulation in T_e and the threshold energies for generation of the plasma species through electron impact collisions. As T_e increases, the number of electrons with energies higher than the

threshold energy for inelastic collisions increases. This leads to increases in $[N_2(A)]$, $[Ar^+]$, and n_e during the pulse on period. Changes in the densities of plasma species occur slower than changes in T_e. First, the densities of excited states are in the pulse-periodic steady state. Many pulses are required to achieve this steady state, with an incremental change in each pulse. At the beginning of the pulse, electrons gain energy from the applied rf electric field quickly, however, a longer time is required for that energy to be dissipated through collisions at 5 mTorr.

At 5 mTorr, T_e initially spikes to a value of ≈12 eV when the plasma turns on at t ≈ 1 μs at a height of 11.5 cm. This leads to an immediate increase in electron and ion density as the high temperature electrons undergo ionizing collisions. There is some oscillation in the first few microseconds as the sudden increase in density from the spike in T_e at t ≈ 1 μs causes T_e to drop below its quasi-steady state value, which causes a dip in ionization and density, which causes T_e to increase again. During this process and throughout the pulse on period, as the electron density increases the skin depth in which plasma is absorbed decreases. As the ICP power is fixed, the power density must go up, which increases electron heating, raising T_e above its quasi-steady state value.

At the peak density of ≈1.6 x 10^{11} cm^{-3}, the skin depth becomes ≈1.3 cm, which causes the height of 11.5 cm, which is ≈1.1 cm away from the dielectric window, to be near the edge of the skin depth. Being at the fringe of the skin depth causes the power density to decrease, which reduces T_e and n_e back toward their quasi-steady state values. In the afterglow, T_e rapidly decreases due to diffusion cooling. As pressure increases, the rate of diffusion cooling drops due to the reduction in mean free path (MFP) going from 5 mTorr to 50 mTorr. This process is somewhat mitigated by gas heating, which rarefies the gas and reduces the gas density. Going from 5 mTorr to 50 mTorr, the reactor averaged gas temperature increases from ≈550K to ≈620K,

an increase of ≈13%. As pressure increases, the increased collisionality as well as the higher n_e at the beginning of the pulse, suppress the oscillations in T_e. The increased density at the beginning of the pulse also suppresses the effect of the change in the skin depth on T_e and n_e as n_e reaches ≈1.6 x 10^{11} cm^{-3} and a skin depth of ≈1.3 cm within 2 μs of the start of the pulse at 50 mTorr and the density continues to increase throughout the pulse.

At 5 mTorr and a height of 5.5 cm, below the midplane, the electron density does not immediately increase at the start of the pulse. There is a finite speed at which energy is transferred from the skin depth through the plasma outside the skin depth to lift the tail of the EED sufficiently to initiate an increase in ionization and electron density. This "ionization speed" can be estimated from Figs. 3.5 and 3.6. The overshoot in T_e in the skin depth at a height of 11.5 cm occurs at t ≈ 1 μs. n_e also starts to increase at this time. n_e does not start to increase until t ≈ 5 μs. Thus the ionization speed is ≈6 cm/4 μs or 1.5 x 10^6 cm/s.

3.4 EEDs versus Height

The effect of pulsing of the rf source power on $f_e(\varepsilon)$ is discussed. As a source of validation of our model, EEDs in Ar/N_2 ICP with a cw power of 350 W at 60 mTorr for different Ar/N_2 gas ratios, are compared to the experimental results of Singh and Graves [7] in Fig. 3.7. There is agreement between this model and the experimental data in the observed trend of a decreased dip in the EED at around 3 eV as the Ar content is increased. The dip in the EED at around 3 eV is a result of resonant electron-molecule vibrational cross sections in N_2.[7] The EEDs become more Maxwellian as the Ar content is increased. There is some discrepancy between the model and experimental results at low energy, but this could be partly due to the low collection efficiency of Langmuir probes at low energies.

$f_e(\varepsilon)$ at different times during the pulse cycle for a radius of 5.9 cm and heights of 11.5 cm (in the skin depth) and 5.5 cm (below the midplane) are shown in Figs. 3.8 for 5 mTorr and Fig. 3.9 for 50 mTorr. The ICP is operated with a PPA power of 300 W and a duty cycle of 30%. At 5 mTorr, the overshoot in T_e in the skin depth produces an extension of $f_e(\varepsilon)$ to high energies, which persists for the duration of the power-on portion of the cycle. Upon termination of the power, $f_e(\varepsilon)$ decays most rapidly at energies above the threshold for excitation of N_2(A) at 6.2 eV. As $f_e(\varepsilon)$ thermalizes during the afterglow, the EED separates into two regions. The cross sections for vibrational excitation of N_2 are resonant with appreciable values only between 1.3 and 3.8 eV. The threshold for electronic excitation of N_2(A) is at 6.2 eV. Thus, there is an energy region between 3.8 eV and 6.2 eV where elastic collisions dominate. Electrons between these two energies have a lower rate of energy loss than either lower or higher energies. For example, at the start of the afterglow, at a radius of 5.9 cm and height of 11.5 cm, the power loss per electron at 5 eV (in the elastic gap) is ≈286 eV/s during the afterglow, whereas at 2 eV the power loss is ≈3.4 x 10^5 eV/s and at 8 eV is ≈2.0 x 10^5 eV/s. Electrons will persist in this energy gap for extended periods of time due to their low power loss.

At a height of 5.5 cm, the tail of $f_e(\varepsilon)$ rises as electrons accelerated in the skin depth transport across the reactor. Note that the tail of $f_e(\varepsilon)$ at time 1 (beginning of power-on) is depressed at the lower height, while the tail is extended in the skin depth. $f_e(\varepsilon)$ has a 2-temperature distribution early during the pulse as the less populated tail is repopulated with high energy, long mean free path electrons. The decay process for $f_e(\varepsilon)$ at the lower height is nearly the same as in the skin-depth. The decay of electron energy has both local and non-local components, neither of which depends strongly on position. Collisional energy loss depends only on the local density and mole fractions of the gas. Although the gas is somewhat rarefied in

the center of the reactor (T_{gas} = 632 K), the mole fractions are fairly uniform. So the rate of collisional loss is nearly the same as a function of position. The non-local component of the decay is diffusion cooling, which primarily involves long-mean-free path electrons having energies greater than the plasma potential.

At 50 mTorr, the behavior of $f_e(\varepsilon)$ in the electromagnetic skin depth is similar to that at 5 mTorr – an initial extension of the tail of $f_e(\varepsilon)$, followed by a collisional relaxation. Lower in the reactor, the behavior of $f_e(\varepsilon)$ is also similar to that at 5 mTorr, except that the tail of $f_e(\varepsilon)$ during the pulse does not extend as far. At 5 mTorr and a height of 11.5 cm, the momentum transfer mean free path (MFP) is ≈20.6 cm and the inelastic collision MFP is ≈23.1 cm, which leads to an energy relaxation length of ≈12.6 cm, which is essentially the reactor height. At 50 mTorr the larger gas density leads to a larger collision frequency, which reduces the MFPs and energy relaxation length. The momentum transfer mean free path (MFP) is reduced to ≈4.1 cm and the inelastic collision MFP is ≈4.8 cm, which leads to an energy relaxation length of ≈2.6 cm. The reduction in MFP going from 5 mTorr to 50 mTorr leads to an increase in collision frequency from ≈2.1 x 10^6 s^{-1} to ≈1.4 x 10^7 s^{-1}.

This means that at 5 mTorr, electrons that are heated in the skin depth at a height of 11.5 cm retain most of their energy upon reaching the height of 5.5 cm since it is only 6 cm away, half the energy relaxation length. At 50 mTorr, electrons that are heated in the skin depth at a height of 11.5 cm lose a significant amount of their energy before reaching a height of 5.5 cm, which is over 2 energy relaxation lengths away. This is particularly seen during the pulse at energies above the threshold for electronic excitation of nitrogen, with increasing effect at higher energies. Inelastic processes, particularly those like excitation and ionization, will cause the biggest source

of energy loss due to their higher threshold energies. This is why the biggest deviation with pressure comes at energies above the threshold energy for electronic excitation of N_2.

The time averaged EEDs as a function of height at a radius of 5.9 cm, for three different duty cycles are shown in Fig. 3.10 for 5 mTorr and Fig. 3.11 for 50 mTorr, respectively. The threshold energies for excitation of $N_2(v = 1)$, $N_2(A)$ and Ar^+ (from the ground state) are noted. At 5 mTorr, the time averaged EEDs are not sensitive functions of position and duty cycle except at energies above the threshold energy for excitation of $N_2(A)$ from the ground state. Above that energy, $f_e(\varepsilon)$ for all heights have the same shape but the slope becomes more negative the further from the skin depth $f_e(\varepsilon)$ is calculated. The EEDs at low duty cycle have a three-temperature distribution, which begins transitioning to a two-temperature distribution as the duty cycle increases. The ranges in energy that correspond to the three temperature regimes are: ε = 0-1.0 eV, ε = 1.0-2.5 eV, and $\varepsilon > 2.5$ eV. These temperatures are 0.7 eV, 0.59 eV, and 5.8 eV, at a height of 11.5 cm and 0.63 eV, 0.61 eV, and 3.95 eV, at a height of 5.5 cm. These regimes correspond to superpositions or averages of $f_e(\varepsilon)$ during the on and off periods of the pulse. The first two temperature regimes correspond to the pulse off period when $f_e(\varepsilon)$ has thermalized and is cut-off by the vibrational excitation thresholds. The third regime ($\varepsilon > 2.5$ eV) corresponds to the pulse on period. The large mean free path at 5 mTorr leads to electrons that gain energy in the skin depth of the electric field being able to transit axially through the chamber without losing significant energy. The result is that the shape of $f_e(\varepsilon)$ at any height is not a local function of the field at that height. That is, electron energy transport is largely non-local.

As duty cycle decreases, the overshoot in T_e at the start of the pulse increases and the tail of $f_e(\varepsilon)$ is lifted. This results from two factors. For a given PPA power deposition, shorter duty cycles means that the peak power during the power-on cycle is larger. Shorter duty cycles

produce longer inter-pulse periods, which allows for more recombination and diffusion loss. The smaller electron density at the start of the next power-on cycle produces more overshoot. At the same time, the longer duty cycle results in the tail of $f_e(\varepsilon)$ being elevated for a longer fraction of the period. The end result is a lifting of the tail of the pulse averaged EED with increasing duty cycle.

At 50 mTorr, the mean free path of electrons is significantly reduced, leading to increased collisions. The end result is a significant height dependence of the tail of $f_e(\varepsilon)$ and more clear delineation of the collisional threshold energies. There is a more rapid collisional relaxation of the tail of the $f_e(\varepsilon)$ by electronic excitation of N_2, beginning with $N_2(A)$, which produces a more cut-off $f_e(\varepsilon)$ with distance from the skin-depth.

The effect of the PPA power magnitude is also investigated for a PPA power of 75 W, pressures of 5 mTorr and 50 mTorr, and duty cycles of 10%, 30%, and 50%. The trends remain the same and so only results for the 300 W cases are presented. The effect of lowering the PPA power from 300 W to 75 W is to lower the tail of the computed $f_e(\varepsilon)$ for all conditions. $f_e(\varepsilon)$ at the three threshold energies at 75 W is slightly reduced compared to $f_e(\varepsilon)$ at the three threshold energies at 300 W.

3.5 Effects of Pulsing on Source Functions

The spatial profiles for the electron impact source functions for $N_2(v = 1)$, $N_2(A)$, and Ar^+ are shown in Figs. 3.12-3.14. The ICP was operated with a PPA power of 300 W, a duty cycle of 30%, a pressure of 5 mTorr, and a 10 MHz rf frequency. The modulation of the source function between the pulse-on and pulse-off periods increases as the threshold energy for the process increases. For $N_2(v = 1)$, there is finite excitation during the entire pulse-period. For Ar^+, there is essentially no direct ionization of the ground state at the end of the cycle. For all

processes, the peak in the source function occurs underneath the coils within the skin depth of the electromagnetic wave. However, the time at which the source function peaks is different for the three processes. For $N_2(v = 1)$, the source function peaks just after the ICP power has turned off. For $N_2(A)$ the source function has maximum peaks just prior to the ICP power being turned off. For Ar^+, the source function peaks when the ICP power first reaches its peak value after being turned on. These trends result from the dynamics of $f_e(\varepsilon)$ during the pulse-period, with an extended tail at the leading edge of the pulse-on period and transport of high energy electrons downwards through the reactor in the later part of the pulse. Note that the source function for $N_2(v = 1)$ decreases during the pulse under the coil. This results from the tail of $f_e(\varepsilon)$ being so extended that the low energy electrons that produce vibrational excitation are depleted.

The cycle-averaged source functions for $N_2(v = 1)$, $N_2(A)$, and Ar^+ during different periods of a pulse as a function of duty cycle, at (r,z) = 5.9 cm, 11.5 cm, are shown in Figs. 3.16 and 3.17. The operating pressures are 5 mTorr and 50 mTorr, respectively. The ICP is also operated with a PPA power of 300 W and an rf frequency of 10 MHz. The results indicate that duty cycle has little effect on the time averaged magnitude of the source function of a particular process, when averaging over the full pulse period. At most, it changes by a factor of ≈2 going from 50% duty cycle to 10% duty cycle. When the full pulse period is broken down into 3 subset periods: activeglow, early afterglow, and late afterglow, duty cycle can have more of an effect on the time averaged source functions for the subset periods compared to the full pulse period. The early afterglow is defined as the first 2 μs of the afterglow period.

In general, the time averaged source function magnitude increases with decreasing duty cycle for the three plasma species regardless of whether averaging over the full pulse period or a subset of the full period. The source function for $N_2(v = 1)$ increases with decreasing duty cycle

because as the duty cycle decreases with the PPA power remaining constant, a higher peak power is deposited into the plasma during the pulse on period. This leads to a larger T_e and a high rate of ionization during the pulse. There are less low energy electrons in the skin depth during the pulse, as these electrons are constantly gaining energy from the rf electric field. During the afterglow, the high energy electrons created during the pulse quickly lose their energy through collisions, which increases the density of low energy electrons during the afterglow. The ratio of activeglow to afterglow time determines the amount of time spent with the lesser density of low energy electrons of the activeglow versus the greater density of low energy electrons in the afterglow. However, the density of electron in the afterglow is not constant, and decays to lower and lower values as the afterglow time gets longer. This reduction is why the increase in the source function for $N_2(v = 1)$ is not a large function of duty cycle.

Increasing pressure from 5 mTorr to 50 mTorr increases the source function for $N_2(v = 1)$ by a factor of ≈11-13 for the activeglow and early afterglow periods, ≈22-38 for the late afterglow period, and ≈14-17 for the full pulse period depending on duty cycle. Increased pressure increases the gas density, which leads to a greater electron density from the increased collision frequency, which increases from ≈2.1 x 10^6 s^{-1} to ≈1.4 x 10^7 s^{-1}. At 50 mTorr the increased collision frequency reduces the rate of diffusion losses in the afterglow so the low energy electron density remains higher in the afterglow than at 5 mTorr. This causes the increase in the source function of $N_2(v = 1)$ with decreasing duty cycle to be slightly larger.

The source function of $N_2(A)$, averaged over the full pulse period, does not change much at all as a function of duty cycle when averaged over the pulse. While the magnitude of the source function for all three separate periods increases with decreasing duty cycle, the low magnitude in the late afterglow and the short duration of the early afterglow causes little change

in the source function when averaged over the whole pulse period. This same behavior is seen at both 5 mTorr and 50 mTorr. The source function for $N_2(A)$ increases by a factor of ≈5 for the activeglow period, ≈ 3-10 for the early afterglow period, ≈38-175 for the late afterglow period, and ≈5 for the full pulse period depending on duty cycle as pressure increases. The magnitude of the source function in the late afterglow is three orders of magnitude less than in the activeglow. Thus the late afterglow behavior has little to do with the behavior of the source function averaged over the entire pulse period. In the late afterglow, the higher energy electrons needed to electronically excite N_2 to $N_2(A)$ diffuse away or lose their energy through collisions, thereby reducing the source function.

The source function for Ar^+, averaged over the full pulse period, increases slightly with decreasing duty cycle. This occurs even though the source function of Ar^+ is zero in the late afterglow. As duty cycle decreases and the PPA power is kept constant, more and more power is being deposited in the pulse on period. This raises the tail of $f_e(\varepsilon)$ higher and higher leading to a significant increase in the source function when averaged over the activeglow period. The source function during the activeglow is so large that it dominates the average over the full pulse period. The source function averaged over the early afterglow period increases greatly with decreasing duty cycle as electrons are heated to higher and higher energies, increasing the number of electrons able to undergo multiple ionizing collisions. Increasing pressure increases the electron and gas density but also increases the collision frequency, which lowers the tail of $f_e(\varepsilon)$ above the threshold for argon ionization. In this case the lowering of the EEDF tail almost perfectly balances out the increase in gas and electron density, such that there is essentially no change in the source function when averaged over the activeglow or the full pulse period.

We can see that these results match our observations of the effect of pressure on $f_e(\varepsilon)$ time averaged over the full pulse at height z = 11.5 cm, as seen in Figs. 3.10 and 3.11. If the time averaged $f_e(\varepsilon)$ remains the same when the pressure is increased from 5 mTorr to 50 mTorr, then an increase of ≈ 10 in the time averaged source functions is expected due to the increase in gas density by ≈ 10. Observed deviations from this approximate value can be attributed to changes in the magnitude of $f_e(\varepsilon)$ at the threshold energy for the generation of the particular plasma species. If we look at the magnitude of $f_e(\varepsilon)$ at the threshold energy for the generation of each of the three species, we see the effect of pressure increasing or decreasing the magnitude of $f_e(\varepsilon)$. This leads to the observed deviations in the change with pressure, of the magnitude of the source functions time averaged over the full pulse, from the expected value of ≈ 10.

The effect of the PPA power magnitude is also investigated for a PPA power of 75 W, pressures of 5 mTorr and 50 mTorr, and duty cycles of 10%, 30%, and 50%. The trends remain the same and thus only results for the 300 W cases are presented. While the trends are the same, the modulation in the source functions of $N_2(v = 1)$ and $N_2(A)$ over the pulse increase significantly at 5 mTorr. The increase in source function modulation for those two species is a result of the larger reduction of the source functions in the plasma afterglow compared to the plasma activeglow. For Ar^+ the source function is already 0 in the afterglow, so this enhanced modulation is not seen. Lowering the PPA power from 300 W to 75 W reduces the source function magnitude for all conditions. With $f_e(\varepsilon)$ retaining the same overall shape at the three threshold energies at 75 W versus 300 W except slightly reduced in magnitude, changing the power changes the magnitudes of the source functions but not their temporal behavior.

One thing to note is that even though at 5 mTorr the time averaged magnitude of the source function, over the full pulse, of Ar^+ can be larger than that of $N_2(v = 1)$, Ar^+ is almost

exclusively generated during the pulse on period, while $N_2(v = 1)$ is constantly generated. This means that depending on the lifetimes of Ar^+ and $N_2(v = 1)$, their diffusion rates, and the position of the substrate, the actual time-averaged flux ratio between the two species can be very different than what might be expected from the time averaged source functions. This should generally be true when trying to control the flux ratio between any high and low threshold energy plasma species.

3.6 Concluding Remarks

In conclusion, results from a computational investigation of the potential of using pulsed power in an ICP to control $f_e(\varepsilon)$ and the magnitude of the source functions for low, mid, and high threshold energy processes are explored. The source functions for $N_2(v = 1)$, $N_2(A)$, and Ar^+ are used to represent low, mid, and high threshold energy processes, respectively. The effect of pressure and duty cycle is investigated at different heights. It is found that duty cycle does not have a significant impact on the time-averaged values, over the full pulse, of either $f_e(\varepsilon)$ or the source functions. The effect of duty cycle is to raise the tail of $f_e(\varepsilon)$ slightly, but the operating pressure determines the overall shape. The time-averaged magnitude of the source functions, over the full pulse, for the three species varies by at most a factor of 2 going from a 10% duty cycle to a 50% duty cycle.

Pressure has a significant effect on both $f_e(\varepsilon)$ and source functions. Increasing pressure decreases the electron mean free path. It also leads to a higher electron density during the pulse, which reduces the skin depth of the electromagnetic wave. All of this leads to a lowering of the tail of $f_e(\varepsilon)$, particularly outside of the skin depth, as well as a more significant dependence of $f_e(\varepsilon)$ on height. The source functions generally increase in magnitude with pressure in the skin depth due to the much larger gas density. Choice of PPA power has no effect on the overall shape of

$f_e(\varepsilon)$ except to lower the tail of $f_e(\varepsilon)$. This leads to a reduction in the magnitude of the source functions. The source functions of $N_2(v = 1)$ and $N_2(A)$ are able to be modulated over a larger range at 75 W PPA power due to the much lower tail of $f_e(\varepsilon)$ in the afterglow compared to at 300 W.

Overall, the initial choice of operating parameters such as pressure and distance of the wafer from the substrate have the biggest impact on controlling the flux of plasma species to the substrate surface. This is somewhat gas dependent, as the lifetimes and diffusion rates of the desired species also have a significant impact on the ability to control the flux of different plasma species to the substrate using the prescribed parameters.

3.7 Figures

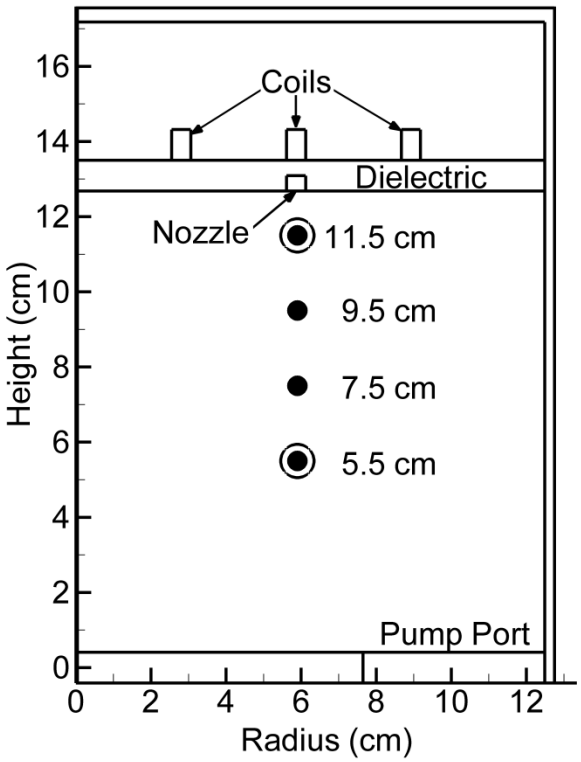

Figure 3.1 Schematic of model Inductively Coupled Plasma (ICP) reactor. EEDF calculations are taken at the positions indicated by the filled black circles at a radius of 5.9 cm.

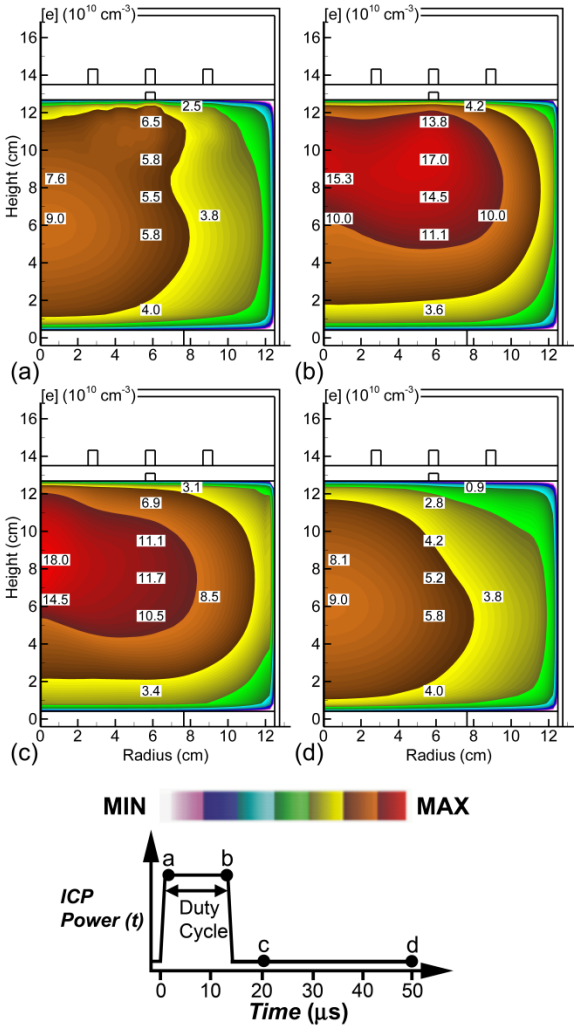

Figure 3.2 Electron density at different times during a single pulse of the ICP. Plasma conditions are Ar/N_2 (80/20), 300 W pulsed-period-averaged power, 5 mTorr, 100 sccm, 10 MHz, pulse repetition frequency = 20 kHz, duty cycle = 30%. (a) Start of pulse on period. (b) End of pulse on period. (c) Start of afterglow period. (d) End of afterglow period.

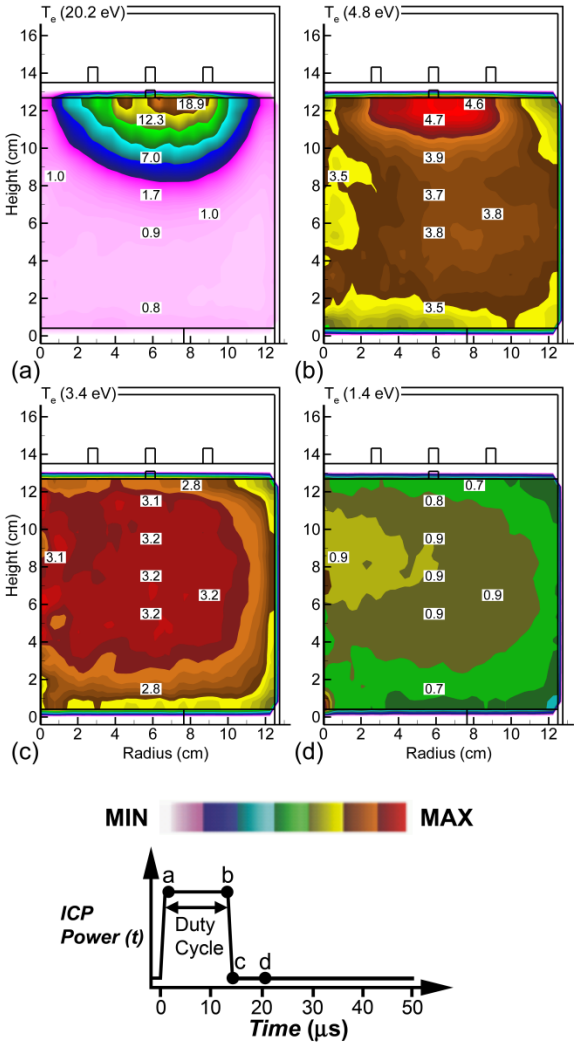

Figure 3.3 Electron temperature at different times during a single pulse of the ICP. Plasma conditions are Ar/N_2 (80/20), 300 W pulsed-period-averaged power, 5 mTorr, 100 sccm, 10 MHz, pulse repetition frequency = 20 kHz, duty cycle = 30%. (a) Start of pulse on period. (b) End of pulse on period. (c) Start of afterglow period. (d) End of afterglow period.

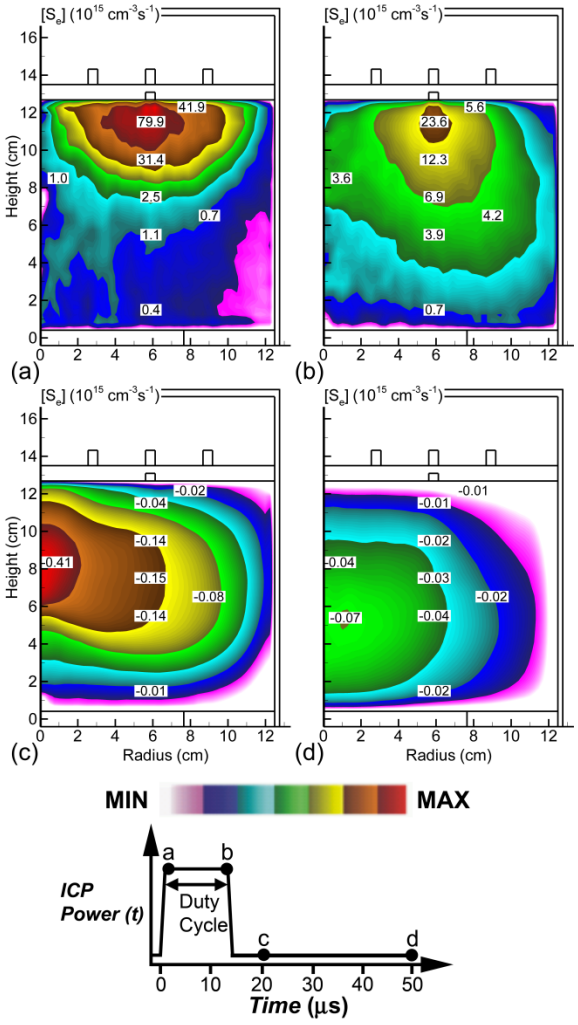

Figure 3.4 Electron source function at different times during a single pulse of the ICP. Plasma conditions are Ar/N_2 (80/20), 300 W pulsed-period-averaged power, 5 mTorr, 100 sccm, 10 MHz, pulse repetition frequency = 20 kHz, duty cycle = 30%. (a) Start of pulse on period. (b) End of pulse on period. (c) Start of afterglow period. (d) End of afterglow period.

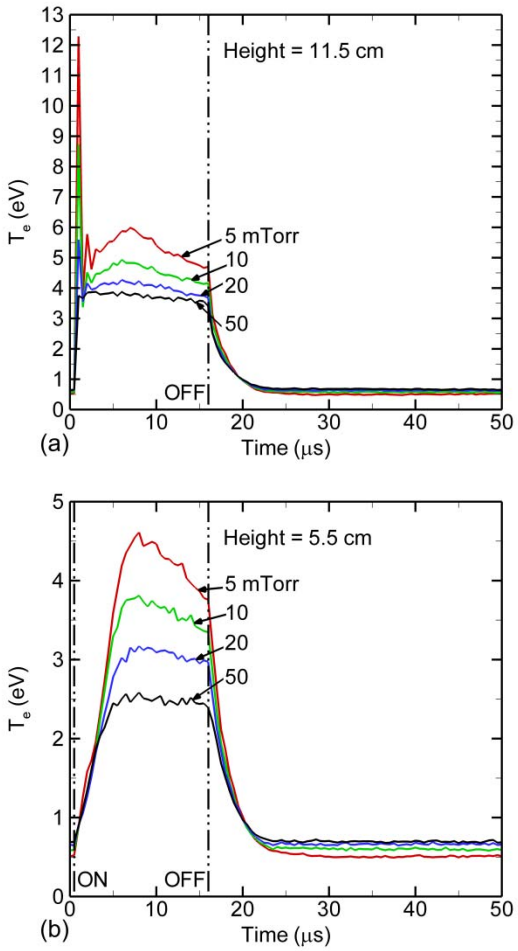

Figure 3.5 Electron temperature as a function of time for a single pulse at different pressures at two positions. Plasma conditions are Ar/N_2 (80/20), 300 W pulsed-period-averaged power, 100 sccm, 10 MHz, pulse repetition frequency = 20 kHz, duty cycle = 30%. (a) (r,z) = (5.9 cm, 11.5 cm). (b) (r,z) = (5.9 cm, 5.5 cm).

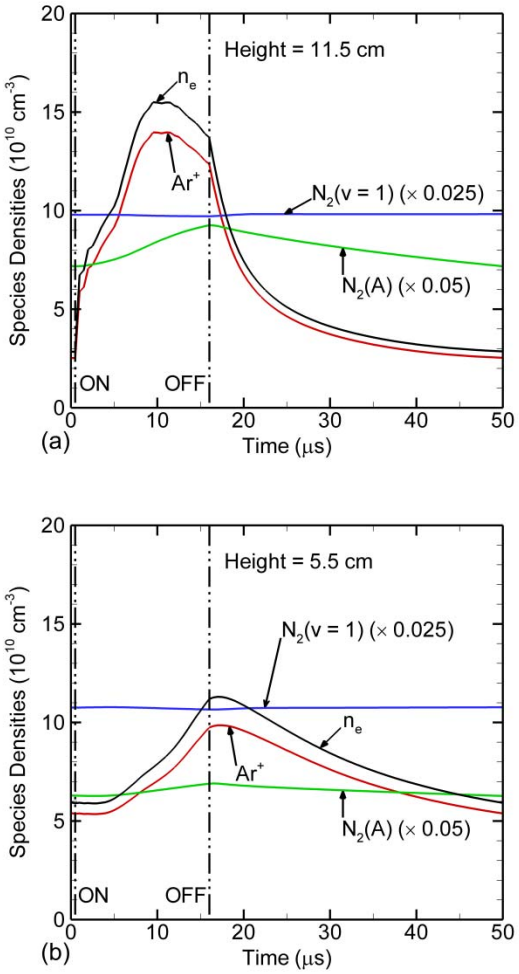

Figure 3.6 Density of plasma species (n_e, $N_2(v = 1)$, $N_2(A)$, and Ar^+) as a function of time for a single pulse at two positions. Plasma conditions are Ar/N_2 (80/20), 300 W pulsed-period-averaged power, 5 mTorr, 100 sccm, 10 MHz, pulse repetition frequency = 20 kHz, duty cycle = 30%. (a) (r,z) = (5.9 cm, 11.5 cm). (b) (r,z) = (5.9 cm, 5.5 cm).

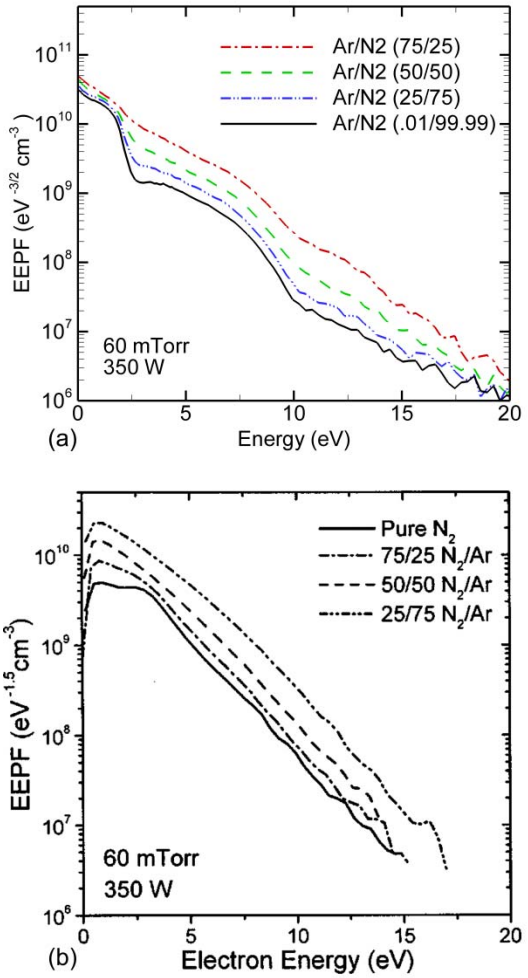

Figure 3.7 Electron energy probability functions (EEPFs) in an Ar/N_2 ICP for different gas mixture ratios Comparison is made between simulated EEPFs in the system shown in Fig. 1 and the experimental results found in [7]. (a) Simulated, plasma conditions are 350 W constant power, 60 mTorr, 100 sccm, 10 MHz. (b) Experimental, plasma conditions are 350 W constant power, 60 mTorr, 13.56 MHz.

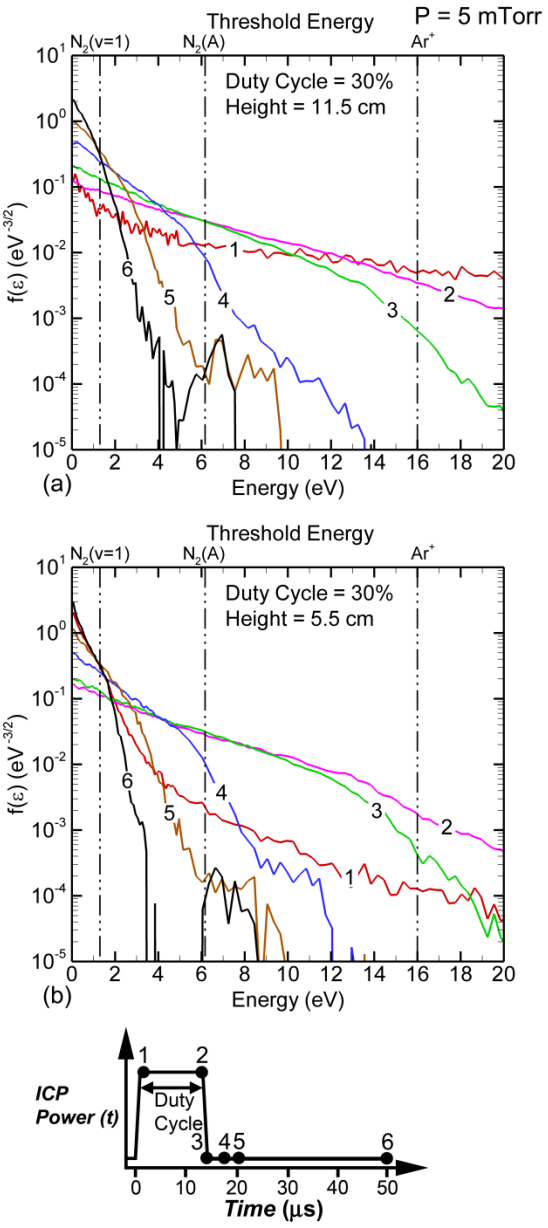

Figure 3.8 EEDFs as a function of time for a single pulse at two positions. Plasma conditions are Ar/N_2 (80/20), 300 W pulsed-period-averaged power, 5 mTorr, 100 sccm, 10 MHz, pulse repetition frequency = 20 kHz, duty cycle = 30%. (a) (r,z) = (5.9 cm, 11.5 cm). (b) (r,z) = (5.9 cm, 5.5 cm).

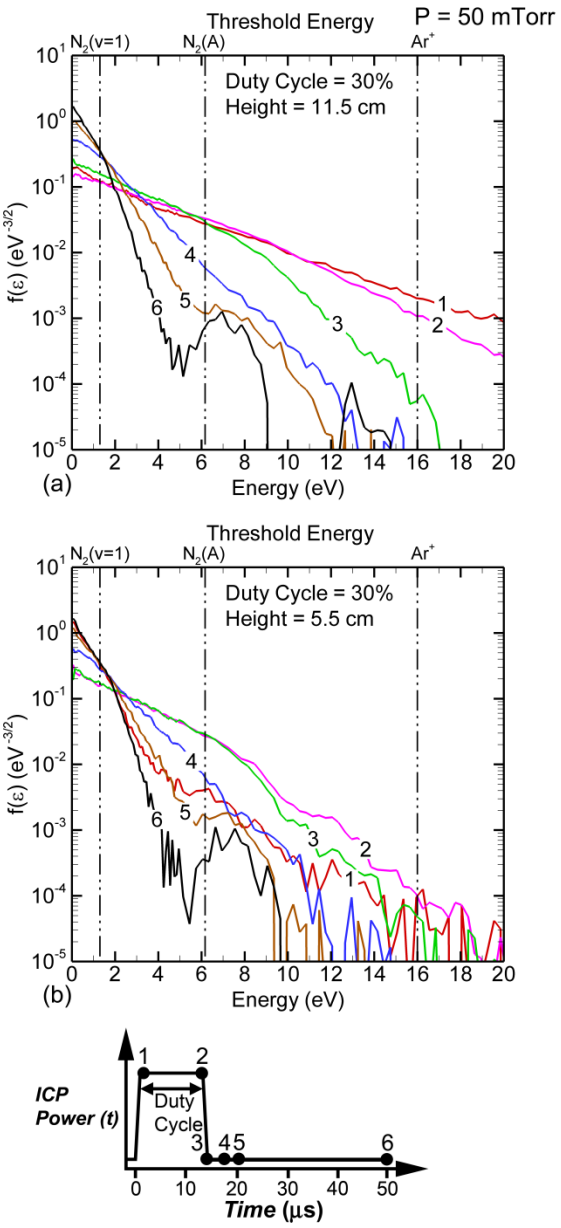

Figure 3.9 EEDFs as a function of time for a single pulse at two positions. Plasma conditions are Ar/N_2 (80/20), 300 W pulsed-period-averaged power, 50 mTorr, 100 sccm, 10 MHz, pulse repetition frequency = 20 kHz, duty cycle = 30%. (a) (r,z) = (5.9 cm, 11.5 cm). (b) (r,z) = (5.9 cm, 5.5 cm).

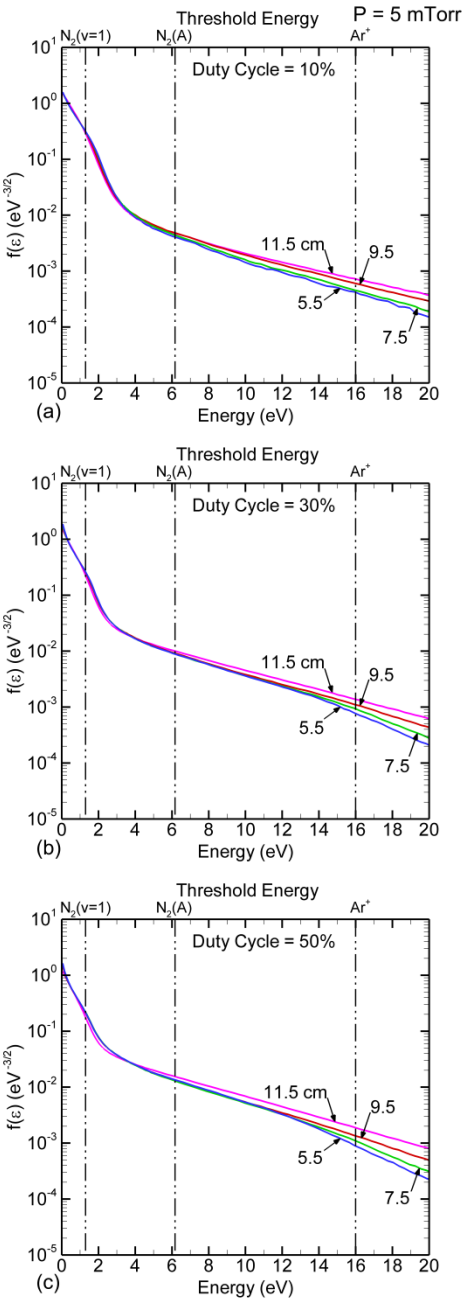

Figure 3.10 Time averaged EEDFs versus Height at a radius of 5.9 cm for different duty cycles. Plasma conditions are Ar/N_2 (80/20), 300 W pulsed-period-averaged power, 5 mTorr, 100 sccm, 10 MHz, pulse repetition frequency = 20 kHz. (a) 10%. (b) 30%. (c) 50%.

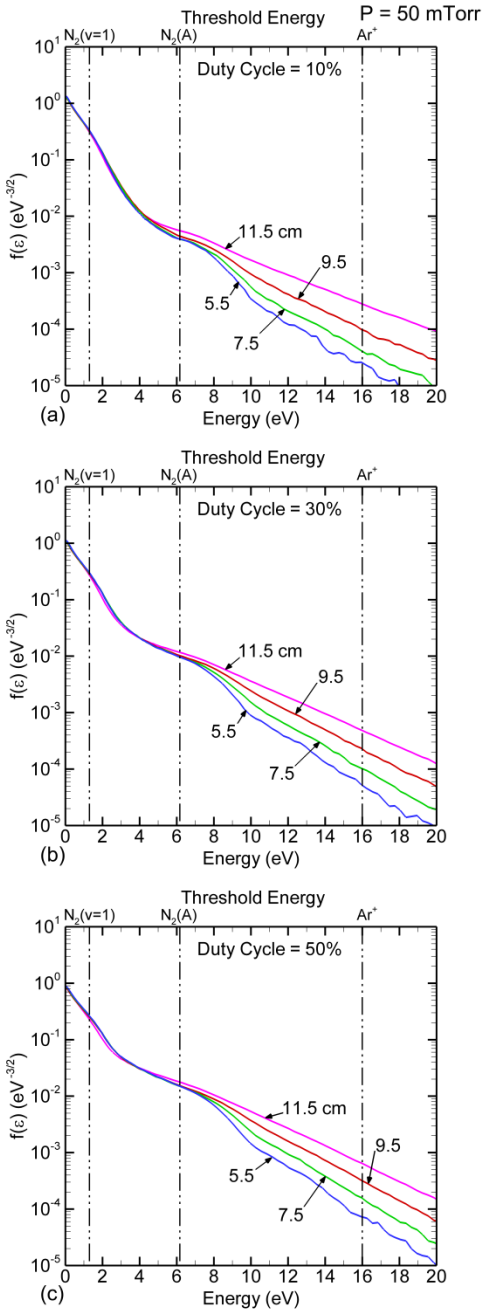

Figure 3.11 Time averaged EEDFs versus Height at a radius of 5.9 cm for different duty cycles. Plasma conditions are Ar/N_2 (80/20), 300 W pulsed-period-averaged power, 50 mTorr, 100 sccm, 10 MHz, pulse repetition frequency = 20 kHz. a) 10%. (b) 30%. (c) 50%.

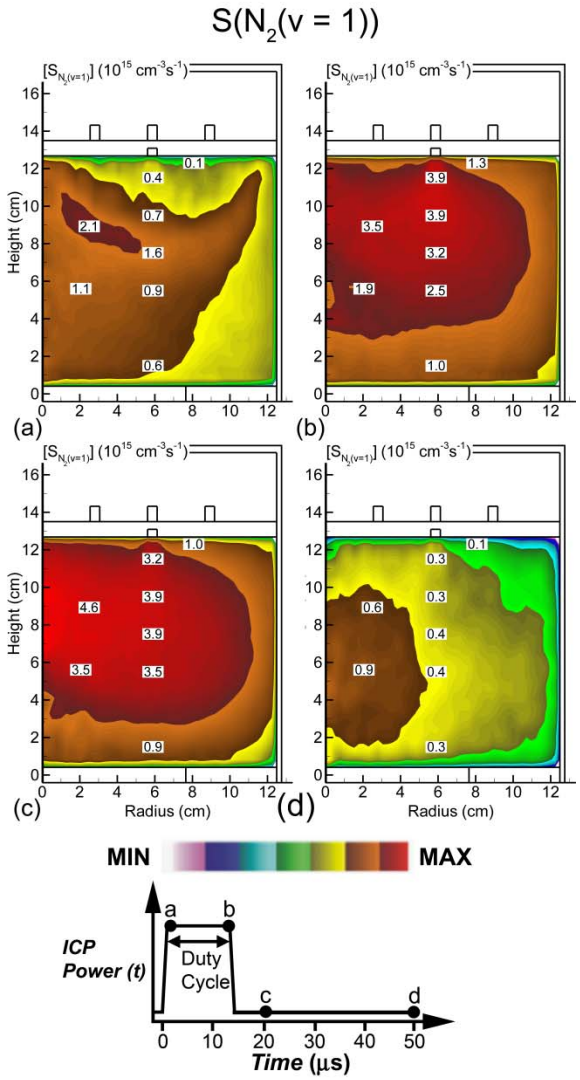

Figure 3.12 Source function of single step excitation of N_2 ground state to $N_2(v = 1)$ vibrational state at different times during a single pulse of the ICP. Plasma conditions are Ar/N_2 (80/20), 300 W pulsed-period-averaged power, 5 mTorr, 100 sccm, 10 MHz, pulse repetition frequency = 20 kHz, duty cycle = 30%. (a) Start of pulse on period. (b) End of pulse on period. (c) Start of afterglow period. (d) End of afterglow period.

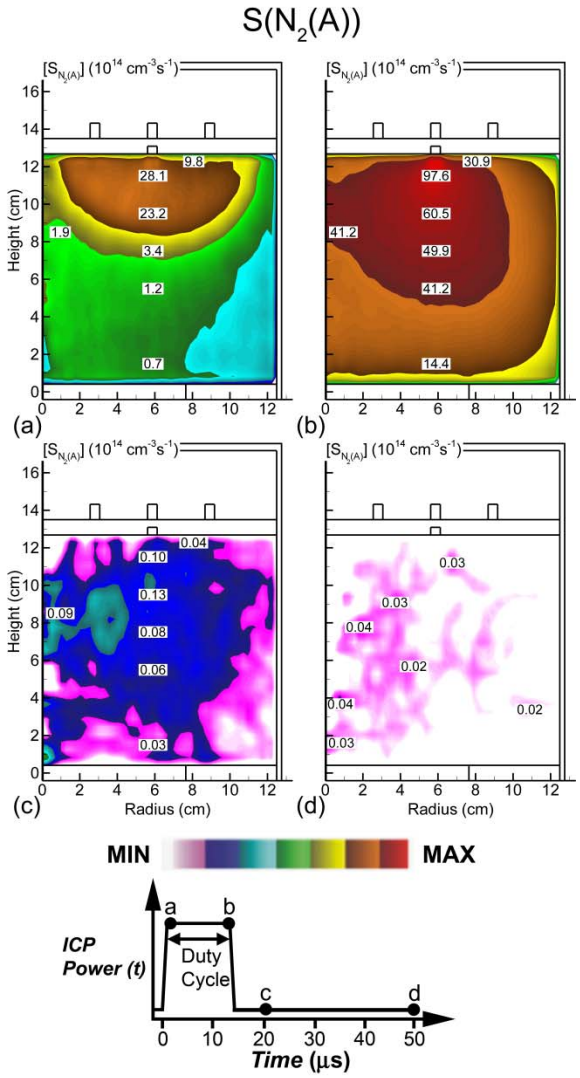

Figure 3.13 Source function of single step excitation of N_2 to $N_2(A)$ electronic state at different times during a single pulse of the ICP. Plasma conditions are Ar/N_2 (80/20), 300 W pulsed-period-averaged power, 5 mTorr, 100 sccm, 10 MHz, pulse repetition frequency = 20 kHz, duty cycle = 30%. (a) Start of pulse on period. (b) End of pulse on period. (c) Start of afterglow period. (d) End of afterglow period.

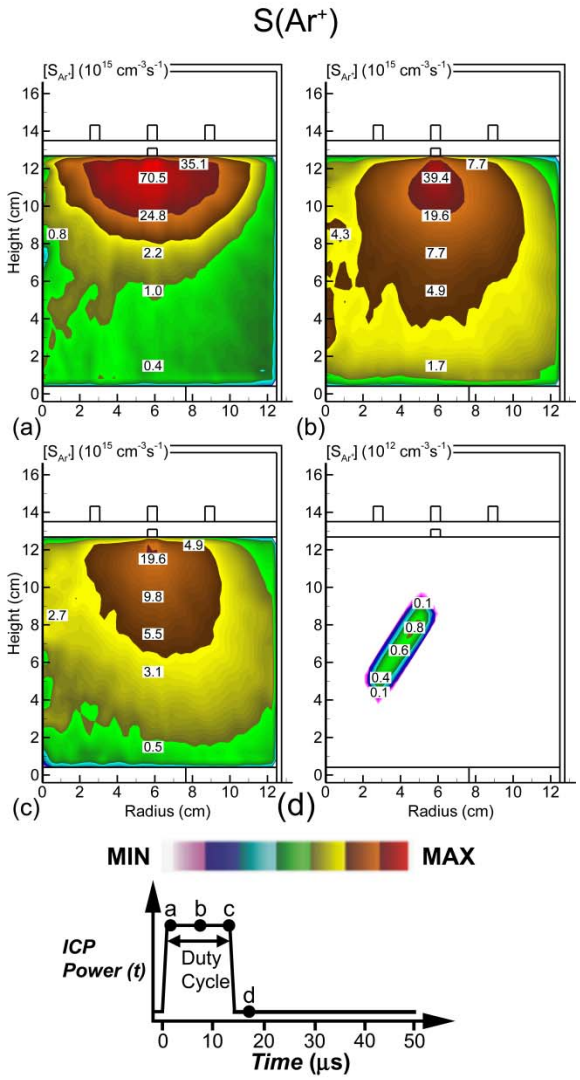

Figure 3.14 Source function of single step ionization of Ar ground state to Ar^+ ionized state at different times during a single pulse of the ICP. Plasma conditions are Ar/N_2 (80/20), 300 W pulsed-period-averaged power, 5 mTorr, 100 sccm, 10 MHz, pulse repetition frequency = 20 kHz, duty cycle = 30%. (a) Start of pulse on period. (b) End of pulse on period. (c) Start of afterglow period. (d) End of afterglow period.

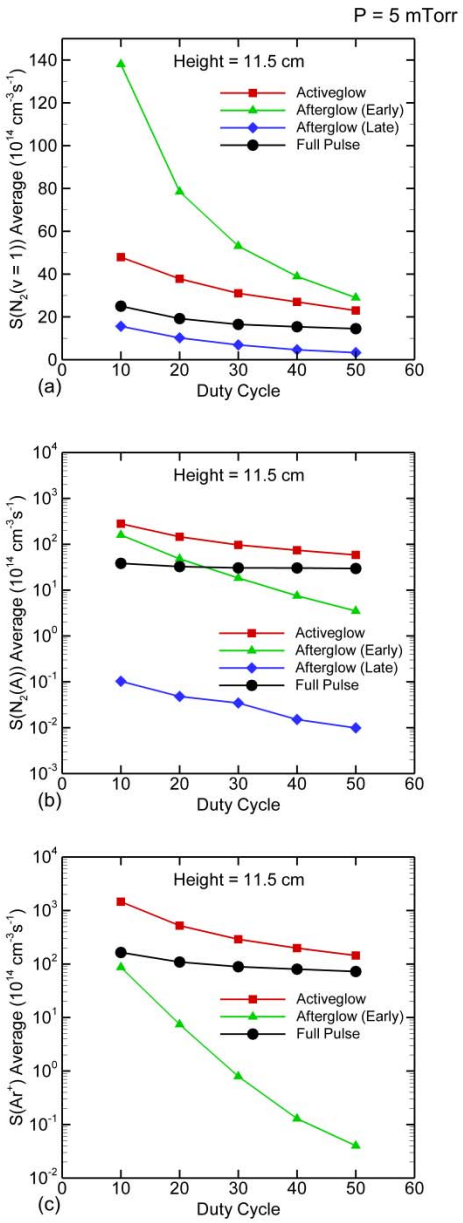

Figure 3.15 Time averaged source functions for a single pulse at (r,z) = (5.9 cm, 11.5 cm) during different time periods in the pulse as a function of duty cycle. Plasma conditions are Ar/N_2 (80/20), 300 W pulsed-period-averaged power, 5 mTorr, 100 sccm, 10 MHz, pulse repetition frequency = 20 kHz, duty cycle = 30%. (a) Source function of single step excitation of N_2 ground state to $N_2(v = 1)$ vibrational state. (b) Source function of single step excitation of N_2 to $N_2(A)$ electronic state. (c) Source function of single step ionization of Ar ground state to Ar^+ ionized state.

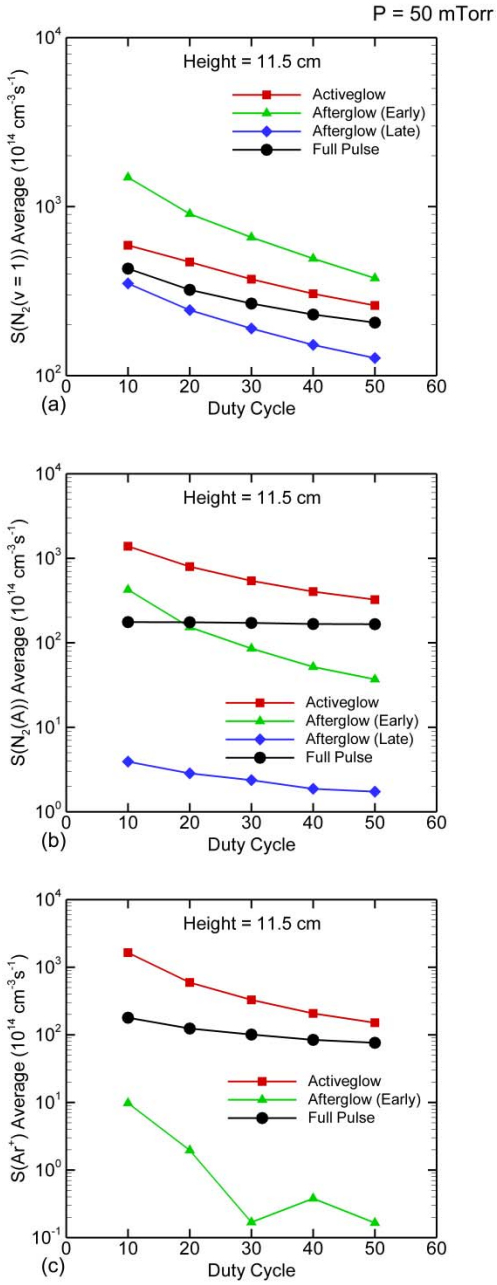

Figure 3.16 Time averaged source functions for a single pulse at (r,z) = (5.9 cm, 11.5 cm) during different time periods in the pulse as a function of duty cycle. Plasma conditions are Ar/N_2 (80/20), 300 W pulsed-period-averaged power, 50 mTorr, 100 sccm, 10 MHz, pulse repetition frequency = 20 kHz, duty cycle = 30%. (a) Source function of single step excitation of N_2 ground state to $N_2(v = 1)$ vibrational state. (b) Source function of single step excitation of N_2 to $N_2(A)$ electronic state. (c) Source function of single step ionization of Ar ground state to Ar^+ ionized state.

3.8 References

1. D. J. Economou, Thin Solid Films, **365**, 348 (2000).
2. K. Takahashi, M. Hori, and T. Goto, Jpn. J. Appl. Phys., **32**, 1088 (1993).
3. T. Goto and M. Hori, Jpn. J. Appl. Phys., **35**, 6521 (1996).
4. Y. Yasaka and K. Nishimura, Plasma Sources Sci. Technol. **7**, 323 (1998).
5. M. Bauer, T. Schwarz-Selinger, H. Kang, and A. von Keudell, Plasma Sources Sci. Technol. **14**, 543 (2005).
6. U. Kortshagen, I. Pukropski, and M. Zethoff, J. Appl. Phys. **76**, 2048 (1994).
7. H. Singh and D. B. Graves, J. Appl. Phys. **87**, 4098 (2000).
8. M. V. Malyshev and V. M. Donnelly, Plasma Sources Sci. Technol. **9**, 353 (2000).
9. G.A. Hebner and C. B. Fleddermann, J. Appl. Phys. **82**, 2814 (1997).
10. T. Kimura and K. Ohe, J. Appl. Phys. **89**, 4240 (2001).
11. A. Maresca, K. Orlov, and U. Kortshagen, Phys. Rev. E **65**, 056405 (2002)
12. V. A. Godyak, R. B. Piejak, and B. M. Alexandrovich, Plasma Sources Sci. Technol. **11**, 525 (2002).
13. V. A. Godyak, "Nonequilibrium EEDF in Gas Discharge Plasmas", IEEE Trans. Plasma Sci. **34**, 755 (2006).
14. M. J. Kushner, J. Phys. D: Appl. Phys. **42**, 194013 (2009).
15. S.-H. Song and M. J. Kushner, Plasma Sources Sci. Technol. **21**, 055028 (2012).

Chapter 4 Ion Energy Distributions in Inductively Coupled Plasmas Having a Biased Boundary Electrode

4.1 Introduction

Control of ion energy distributions (IEDs) is important in a variety of plasma processing applications and, in particular, for plasma etching of microelectronics devices.[1-15] As feature sizes for microelectronic devices continue to shrink, tolerances for plasma etching become more stringent. To achieve the necessary wafer etch performance to meet these challenges better control of process conditions is required. Some important wafer etch performance areas that need to be better controlled for future microelectronics include vertical versus lateral etching, plasma induced damage, and profile deformation.[16] This can be achieved through control of etch characteristics such as etch rates, etch selectivity, and the energies of ions bombarding the wafer. Obtaining the desired etch rates, etch selectivity, and ion energies depends on controlling the IEDs for a given set of energy and material dependent reaction probabilities.[1-9] A number of strategies have been proposed to obtain this control, including non-sinusoidal waveforms [1, 9, 11, 13-15], multiple frequencies,[12] and pulsing[5-8, 10].

Wang and Wendt demonstrated an increase in the selectivity of etching between SiO_2 and Si through the use of tailored bias waveforms to produce nearly monoenergetic IEDs.[1, 9] Qin, Ting, and Wendt [13] investigated the effect of both sinusoidal and tailored bias waveforms on the substrate in an Ar/He pulsed helicon plasma. They found that the sinusoidal biases produced broad bimodal IEDs, with higher frequencies producing narrow IEDs. A typical bimodal IED produced by an rf bias is a double peaked IED, with the peaks corresponding to ion

bombardment at the minimum and maximum sheath potential. The sheath potential oscillates between its minimum and maximum due to the oscillating rf bias potential. Tailored bias waveforms, essentially a pulsed dc bias, allowed for a near constant sheath voltage and the production of narrow IEDs centered at approximately the applied voltage. The height of the IED peak decreased with increasing voltage. This was believed to be due to finite rise time effects and increasing charge exchange collisions in the sheath as the sheath width increased. They noted that sinusoidal biases applied even at frequencies of 30-40 MHz have broader IEDs than those produced using tailored waveforms. The tailored waveforms in principle may avoid finite wavelength effects at higher frequencies which produce radial nonuniformities due to standing waves.[13] However, tailored waveforms also contain Fourier components at these higher frequencies.

Samukawa and Mieno demonstrated increased etch selectivity between polycrystalline Si and SiO_2 by pulsing the microwave power in an electron cyclotron resonance (ECR) plasma.[5] The IED produced from the pulsed plasma was found to be narrower and shifted to lower energy with respect to the continuous wave (cw) case. Banna *et al*. found that synchronous pulsing of the electromagnetic power and the substrate bias power in an inductively coupled plasma (ICP) resulted in greater etch uniformity (but lower etch rate) for HBr/O_2 etching of SiO_2 on Si, an effect attributed, in part, to optimized IEDs.[6]

Agarwal *et al*. also investigated different pulsing modes of operation on simulated IEDs and etching profiles in Ar/Cl_2 plasmas.[8] They found that pulsing of only the rf bias led to a triple peaked IED with narrow peaks at 25, 90, and 200 eV. Pulsing only the ICP source led to a multi-peaked IED with broader peaks at 100 eV and in the 250-350 eV range. Synchronous pulsing of both the ICP and bias power also led to a multi peaked IED, with peaks at 5, 100, and

250 eV. They found that the etching rates could be controlled by various combinations of pulsing the bias, synchronous pulsing, source pulsing and varying duty cycle. These trends were generally explained by IEDs extending to higher energies having higher etching rates.

Lee, Tiwari, and Lee investigated a capacitively coupled plasma (CCP) having three rf biases (1, 30 and 120 MHz) simultaneously applied on the same substrate.[12] They found that the IEDs produced were in general bimodal with the energy spread determined by the voltage ratio of the three biases. They also found that the IEDs narrowed in width as the dominant voltage waveform was shifted to higher frequencies and the rf period became greater than the ion transit time.

To provide more options for controlling IEDs, combinations of pulsed dc and rf biasing of electrodes have been investigated. Xu *et al*.[10] and Diomede *et al*.[14] investigated applying pulsed dc biases in the afterglow of pulsed CCP with the goal of controlling the instantaneous plasma potential. This shifting of the plasma potential in turn controlled contributions to the IED at the energy of the plasma potential. The resulting IEDs had peaks at energies approximately equal to the applied dc bias during the afterglow of the pulsed rf bias in addition to the broader IEDs produced by the rf bias.

In many applications, it is desired to have lower but controllable energies for ions incident onto substrates than typically produced with CCPs. One such application is plasma etching of thin films, where precise control of IEDs is very important.[1] ICPs are an alternative wherein the plasma potential, Φ_P, is typically lower (tens of volts) than in CCPs, and so energies of ions impacting substrate surfaces are lower. In ICPs, ion energies can be raised well above the plasma potential by application of an rf bias, frequently resulting in a bimodal distribution. It is not possible to produce ion energies below the plasma potential unless the pressure is raised to

reduce energies through collisions. These collisions result in an IED that broadens to lower average energy. Since with cw excitation for a given pressure and gas mixture there is limited ability to control T_e (and Φ_P), there is also limited ability to control the IEDs. Pulsed ICPs provide a means to customize IEDs. During a pulsed cycle, the pulse repetition frequency and duty cycle determine the time dependence of ionization sources, T_e and Φ_P. For a sufficiently low pulse repetition frequency, ions will respond to the slowly varying Φ_P and sheath potential, and so customization of the IEDs is possible. However these IEDs tend to be broad, reflecting the difference in potential between the site of formation of the ion and the substrate.

In this chapter, a computational investigation of the IEDs of incident ions onto grounded surfaces in ICPs having a dc biased boundary electrode is presented. The test system models the reactor and experimental conditions of Shin et al.[2] in which pulsed or cw ICP power is combined with pulsed or cw dc biases to produce desired IEDs. It is observed that applying a positive dc bias results in a shift of the IED peak energy by an amount approximately equal to the applied bias, while negative dc biases result in a capped decrease in the IED peak energy. A cw bias results in a single or double peaked IED shifted in energy by the dc bias. IEDs are single peaked with cw ICP power and double peaked when the ICP power is pulsed. It is also observed that applying a pulsed positive dc bias in the afterglow of a pulsed ICP allows the IED peak energy to shift during the afterglow to approximately that of the dc bias during the bias pulse. The magnitude of the peak is determined by the length of the dc bias pulse. The applied dc bias is not found to have a significant influence on the plasma properties due to the relatively low amount of dc power deposition compared to the ICP power.

All results are for plasmas sustained in argon. The species consist of Ar (ground state), Ar*, Ar**, Ar***, Ar^+ and electrons. Ar* represents the combined metastable states of the

$Ar(3p^5 4s)$ manifold [$Ar(1s_5)$, $Ar(1s_3)$] and Ar** represents the combined radiative states [$Ar(1s_4)$, $Ar(1s_2)$]. Ar*** is a lumped state representing $Ar(3p^5 4p)$ and higher states in the excited state manifold. Radiation trapping of the Ar** state is included.

4.2 Description of the Reactor and Experiment

A schematic of the boundary electrode-ICP (BE-ICP) system used in the computational investigation is shown in Fig. 4.1, which is our representation of the experimental device described in Ref. [2]. The plasma is sustained in an 8 cm diameter dielectric tube with a 3-turn spiral coil powered at 10 MHz. (The experiments were done at 13.56 MHz.) A Faraday shield was employed in the experiment to reduce capacitive coupling and insure operation in the H-mode. In the model, a Faraday shield is also employed to suppress capacitive coupling from the coil. The Faraday shield is modeled as a metal except that azimuthal electric fields are allowed to pass through it. The boundary electrode consists of three nested metal cylinders 3 cm tall and 2.6, 6.4 and 8.0 cm in diameter. Gas is injected on axis at the top and pumped annularly at the bottom. IEDs are experimentally measured using a retarding field energy analyzer (RFEA) and so simulations producing IEADs have the RFEA in place, as shown in Fig. 4.1. Plasma parameters [electron temperature (T_e), plasma potential (Φ_P), electron density (n_e), and ion density (n_i)] are experimentally measured using a Langmuir probe without the RFEA in place. Therefore when comparisons between the model and experiment are made for these quantities, the RFEA structure is removed from the simulation. Details of the experimental procedure may be found in Refs. [1] and [2].

4.3 Control of IEDs with Pulsing and BEs

The characteristics of ICPs with cw power and bias are first discussed with comparisons to experiments to provide a baseline for the pulsed studies.

4.3.1 IEDs and plasma parameters with cw excitation

Computed and experimental measurements for electron density along the vertical axis of the reactor for pressures of 7 – 50 mTorr are shown in Fig. 4.2 for a cw power of 300 W and 40 sccm flowrate. The boundary electrode is grounded. The Φ_P on axis at the same height as that of the RFEA, 13.6 cm, are shown as a function of pressure in Fig. 4.2c. In general, there is good agreement between the computed and experimental values. Simulated electron densities have peak values of 1.3×10^{12} cm^{-3} at 50 mTorr, decreasing to 2.9×10^{11} cm^{-3} at 7 mTorr. Φ_P and T_e increase from 10.8 V and 2.7 eV at 50 mTorr to 13.7 V and 3.2 eV at 7 mTorr. The increase in plasma density with increasing pressure for constant power results from the decrease in T_e due to there being a lower rate of loss by diffusion. The lower T_e produces a lower rate of power deposition per electron, thereby requiring a larger electron density to dissipate the same power. The predicted T_e, are 0.1-1 eV higher than measured in the experiment, with the difference being larger at higher pressures.

Computed electron energy distributions, $f_e(\varepsilon)$ at the midpoint of the coil (height = 18 cm) and at a radial position (r = 3.5 cm) corresponding to the inductive skin depth for different pressures are shown in Fig. 4.3. The $f_e(\varepsilon)$ are essentially 2-temperature distributions, with a break point at $\varepsilon \approx 12$ eV, the first inelastic threshold. The effective temperatures of the bulk portion of $f_e(\varepsilon)$ ($\varepsilon < 12$ eV) have little variation with pressure from 7 – 50 mTorr, with $T_b \approx 3.5$ eV . The tails of $f_e(\varepsilon)$ ($\varepsilon > 12$ eV) have effective temperatures that decrease with increasing pressure, reflecting the increase in collisionality. The tail temperatures decrease from $T_t \approx 3.5$ eV at 7 mTorr to 1.4 eV at 50 mTorr. The decrease in ground state ionization rates due to the decrease in T_t is largely offset by the increase in multistep ionization due to increasing densities of Ar*.

n_e and T_e at 300 W and 14 mTorr with and without a 12 V bias applied to the boundary electrode, V_B, are shown in Fig. 4.4. Φ_P as a function of height and, $f_e(\varepsilon)$ at the midpoint of the coil at a radial position near the skin depth of the electromagnetic wave (r = 3.5 cm, height = 18 cm) for different V_B, are shown in Fig. 4.5. These results are with the RFEA in place to align with the IEDs discussed below. T_e has a peak at the side walls within the skin depth of the electromagnetic wave. The high thermal conductivity of the plasma produces a T_e that varies by less than 1 eV over the volume of the plasma, though this value of T_e largely reflects the value of T_b as T_t decreases into the interior of the plasma. The application of V_B = 12 V does not have a significant effect on either n_e or T_e, which is expected as the dc power (≈3.5 W for 12 V bias) is much smaller than the ICP power (300 W). The plasma density increases by only a few percent, and the electron temperature by only a tenth of an eV. The spatial distributions of the plasma potential, and so the bulk electric field, remain largely the same for different values of V_B. The peak value of Φ_P is merely shifted up or down in voltage as V_B is varied. For positive V_B, the plasma potential shifts upwards by approximately V_B. The majority of the applied bias is dropped across the sheath at the grounded substrate. For negative V_B there is a small decrease in the plasma potential of less than 1 V, with most of the bias being dropped across the sheath at the boundary electrode. This would then increase the energy of ions collected on the boundary electrode while not changing the energy of ions collected on the substrate.

The general trends observed in the shift of the plasma potential with V_B can be largely explained by the electropositive nature of the Ar plasma. For positive boundary voltages, the plasma potential is lifted above ground. There is little change in the floating sheath potential, since T_e does not appreciably change. Hence, the majority of this additional voltage is dropped across the sheath at the grounded electrode. When applying a negative bias to the boundary

electrode, there is a limited range over which the peak plasma potential can be lowered while the plasma potential remains sufficiently positive with respect to ground to trap thermal electrons (as required in an electropositive plasma).

Since the amplitude of the inductively coupled field changes little with V_B, electron heating rates are not significantly affected and the $f_e(\varepsilon)$ are essentially independent of applied bias as shown in Fig. 4.5b. Below the inelastic threshold, the $f_e(\varepsilon)$ for the different V_B are indistinguishable. Only in the tails of the distributions do small variations in $f_e(\varepsilon)$ occur. These variations are relatively small and may be partly influenced by the fact that $f_e(\varepsilon)$ is generated statistically.

Computed and experimental IEDs collected at the location of the RFEA are shown in Fig. 4.6 with the ICP operated at 300 W and 14 mTorr, and for V_B of -8 V to 12 V. The shape of the IEDs remains basically the same irrespective of the value of V_B while the energy of the maximum of the IED shifts with V_B. For positive values of V_B, the IED peak shifts from its position for zero bias, 10.8 eV, by approximately the value of V_B. When applying a negative V_B, the peak in the IED decreases from the grounded case by less than 1 eV for V_B as negative as -8 V. The model generally agrees well with the experiment, though the IEDs are systematically 1.4 eV lower in energy, an affect attributable to the computed plasma potential at zero bias being 1.4 V lower than in the experiment. Experimentally obtained IEDs are shown to be much smoother than in the model; however this is a function of the raw experimental data being averaged over 5000 I-V sweeps. This will be observed in all cases where computed IEDs are compared with experimentally obtained IEDs.

The trends in IEDs with V_B correspond to the shift in plasma potential with applied dc bias. For the experimental conditions, the mean free path for momentum transfer (dominated by

charge exchange) for argon ions is in excess of 1 cm, which is greater than the sheath thickness. Ions enter the sheath with an IED determined by their collisional transport from their site of formation, having a FWHM of 4-5 eV. The ions are then collisionlessly accelerated across the sheath, adding qV_B of energy in the case of positive biases. The simulated IEDs are narrower than those obtained experimentally, particularly in the lower energies. This may be due to increased collisionality not captured in the model as well as the inability of the simulation to resolve the true gridded structure of the RFEA which has some instrumental broadening.

4.3.2 IEDs with pulsed plasmas

Pulsing the ICP power and V_B provide additional means to control IEDs. Pulsing the ICP power provides a transient in T_e and so Φ_P, which produces modulation in the IED. In the afterglow of a pulsed ICP, T_e and the corresponding plasma potential decrease, enabling the IED to be shifted to lower energies. Pulsing V_B shifts Φ_P with the majority of the voltage dropped across the sheath, and so provides another means to modulate the peak of the IED. The IED collected over a pulse period is then a cycle average of all of these effects. Since only positive V_B can significantly affect the IED by changing the sheath potential at grounded surfaces, the peak energy of the IED can only be shifted to higher values. The low Φ_P in the afterglow allows for shifting of Φ_P to practically arbitrary values set by the dc bias.

Reactor averaged T_e and the maximum Φ_P as a function of time during one pulse cycle for different pressures without a dc bias are shown in Fig. 4.7 for a pulsed-period-averaged power of 120 W, pulse repetition frequency of 10 kHz and a duty cycle of 20%. (These results are without the RFEA in place.) The ICP power has a 2 μs rise and fall time. Electron energy distributions $f_e(\varepsilon)$ during the pulsed cycle near the skin depth of the electromagnetic wave for a pressure of 14 mTorr are also shown at different times during the pulsed cycle. The

experimental measurements for T_e at essentially the same conditions are shown in Fig. 4.8. When the ICP power is turned on, there is an initial overshoot of both T_e (at all pressures) and Φ_P (at 14 mTorr) followed by a decay to a quasi-steady state value. At the start of the pulse, the ICP power is initially being dissipated by fewer electrons than at the end of the power pulse due to diffusion losses during the power-off portion of the pulse. The end result at lower pressures, where there is more modulation in the electron density during the pulsed period, is an increase in T_e above the quasi-steady state value until sufficient ionization occurs to reduce the power dissipation per electron.[17] Increasing pressure reduces the degree of overshoot of T_e due to the lower rate of electron loss by diffusion during the afterglow, and so less modulation of the electron density during the pulsed cycle. The time dependence of Φ_P tracks that of T_e, increasing during the pulse to confine electrons as T_e increases.

When the ICP power is turned off, both T_e and Φ_P monotonically asymptote to a minimum value before the start of the next power pulse. The rate of decay increases with decreasing pressure, which indicates that diffusion cooling is a dominant energy loss mechanism.[15] (Higher energy electrons diffuse to walls more rapidly than lower energy electrons, which lowers the average electron energy and leads to diffusion cooling.) There is also a component of heating during the afterglow by superelastic relaxation of Ar* states which is more important at higher pressures where the fractional density of Ar* is higher. This heating tends to maintain T_e and Φ_P during the afterglow at higher pressures.[18]

The same trends are observed in the experimental data for T_e in Fig. 4.8. There is an initial overshoot of T_e (at all pressures) followed by a decay to a quasi-steady state value. The initial overshoot and the quasi-steady state value of the pulse on period are about 0.5 eV higher in the simulation compared to the experiment, consistent with differences with the cw

measurements. When the ICP power is turned off, T_e monotonically asymptotes to a minimum value before the start of the next power pulse, with the rate of decay increasing with decreasing pressure.

The dynamics of $f_e(\varepsilon)$ during the pulsed cycle, shown in Fig. 4.7c, reflect those of T_e and Φ_P. Initially, halfway during the rise time of the pulse (point 1 in Fig. 4.7c), all the electrons have energies below 4 eV basically matching the $f_e(\varepsilon)$ at the end of the pulse. When the power pulse initially reaches its peak value (point 2) the $f_e(\varepsilon)$ changes to having a long raised tail extending to an energy of 40 eV. The maximum extent of the tail of $f_e(\varepsilon)$ occurs about 1 μs after the power reaches its plateau value (point 3). The tail of $f_e(\varepsilon)$ then lowers as T_e decays to a quasi-steady state value (points 4 and 5). After the power pulse is turned off the maximum energy of $f_e(\varepsilon)$ reduces rapidly (points 6 and 7) and at t = 45 μs into the pulse (point 8) $f_e(\varepsilon)$ has returned to almost the same shape as at the start of the pulse.

IEDs averaged over the pulsed period are shown in Fig. 4.9a as a function of dc bias voltage. The operating conditions are 14 mTorr, 40 sccm, pulse repetition frequency = 10 kHz, duty cycle = 20% and a pulsed-period-averaged power of 120 W. The dc biases are applied continuously on the boundary electrode. The IEDs are normalized so that the height of the high energy peaks are approximately the same. Experimental results for the same conditions are shown in Fig. 4.9b. For each dc bias, the IED has two peaks – a broader peak at higher energy and a narrower peak at lower energy. These peaks result from the plasma potential during the power on and afterglow periods, respectively. The peak at high energy is within 1 V of the value of Φ_P during the power on portion of the cycle, shifted by the energy of the applied dc bias for positive biases. The width of the IED in the afterglow is narrower than when the ICP power is on, possibly due to the mean ion energy, and thus the width of the IED, being reduced in the

plasma afterglow. Since the application of a dc bias on the boundary electrode merely shifts the IEDs in energy, the narrower IED peak in the afterglow is shifted by the applied bias resulting in narrow IEDs with peaks at approximately the applied bias.

The simulations reproduce the experimental results, with a few exceptions. The high energy peak of the simulated IEDs, is systematically ≈2 - 3 eV lower than the experimental values. The low energy peak of the simulated IEDs is systematically 2 eV higher than the experimental values. This may be partially attributable to the model's prediction of a peak in the IED at ≈1 eV for biases of ≤ 0 V. In the model, this peak results from ions arriving at the RFEA when the plasma potential is at its minimum value late into the afterglow. (A similar low energy peak in the IED was observed during the afterglow of pulsed Ar capacitively coupled plasma using a particle-in-cell simulation by Diomede *et al*.[14])

The lack of this peak in the experiment is believed to be an artifact of the measurement which may discriminate against collection of low energy ions having a broad angular distribution. (In the model, all ions regardless of energy or angle of incidence are collected with the same efficiency.) The RFEA consists of three metal grids and a collector plate spaced 3 mm apart from each other. The top grid is 50% open and connected to a grounded stainless steel plate with a 0.3mm pinhole in contact with the plasma. The middle grid is biased at -30 V to repel electrons, and it is believed that this large negative voltage also acts as a trap to low energy ions, preventing them from reaching the collector plate. The third grid is biased with a saw-tooth ramp voltage to act as an energy discriminator to measure the IED. The middle and bottom grids are 85% open. When the sheath potential is large during the power-on phase (or with a positive dc bias), ions arriving at the RFEA have narrow angular distributions centered on the normal. Late in the afterglow and when the dc bias is negative, the sheath potential is small and so the ion

angular distributions arriving at the RFEA are broader in angle. If the collection efficiency of the RFEA decreases with increasing angle from the normal, particularly at low energy, then the low energy peak would be deemphasized.

To test the possibility of an angular dependence to the collection efficiency, simulations are run where ions are collected only within a specified angle of the normal ranging from 2^0 to 50^0 (full width of 4^0 - 100^0 centered on the normal). The resulting IEDs are shown in Fig. 4.10 for the pulsed plasma just discussed above without a dc bias. As the collection angle narrows, the low energy peak of the IED decreases in magnitude because these ions arrive with distributions having a broad angular spread contained within 9^0-10^0 of the normal (FWHM of 18^0-20^0 centered on the normal). The absolute magnitude of the ions in the high energy peak does not appreciably change, as these ions arrive with angles within about 3^0 of the normal (FWHM of 6^0 centered on the normal). With the IED normalized to unity, the peak at 10 eV increases with narrowing collection angle because the peak at low energy decreases. There is also likely a reduction in the experimental efficiency of recording an ion entering the RFEA having energies of <1 eV, an effect that is not included in the model. The RFEA incorporated a negatively biased grid above the ion energy selector grid. Very low energy ions can be easily deflected and collected by the negatively biased grid.

Another strategy in controlling IEDs is modulating V_B during the pulsed cycle. Since positive values of V_B merely shift the plasma potential, imposing a dc bias during a portion of the pulsed cycle for varying durations, the length of time higher energy ions are generated can be controlled. Using this strategy, one could, in principle, craft an IED which closely matches the threshold energy of a desired surface process.

Using the same pulsed ICP conditions (pulse repetition frequency = 10 kHz, duty cycle =

20% and a pulsed-period-averaged power of 120 W), a 24.4 V dc bias is applied for a time duration of Δt_{Bias} = 18 μs starting at 42 μs during the afterglow. (This is also a delay of Δt_{Delay} = 18 μs after the termination of the ICP pulse at 24 μs.) Plasma potential, electron temperature and electron density at different times during the pulse are shown in Figs. 4.11-4.13. T_e and n_e are not greatly affected by the application of the dc bias in the afterglow. During the active glow, n_e increases from 1.8×10^{11} cm^{-3} (value at the end of the prior pulse period) to 1.1×10^{12} (value at the end of the ICP power pulse), and monotonically decays thereafter. The off-axis peak in n_e early in the ICP power pulse is a reflection of ionization sources first peaking in the skin depth of the electromagnetic field launched from the coils before the thermal conduction (and some amount of long mean-free-path transport) produces high energy electrons and ionizing collisions in the center of the plasma.

Computed IEDs for a dc bias having Δt_{Delay} = 21 μs (starting at 45 μs) and Δt_{Bias} = 50 μs (45-95 μs) during the afterglow are shown in Fig. 4.14a for different pressures. Experimental results are in Fig. 4.15a. The IEDs are double peaked. The high energy peak at ≈25 eV is produced from the Φ_P maintained by the pulsed dc bias during the ICP afterglow when the plasma potential in the absence of the bias would be small. The low energy peak results from ions collected when the ICP power is applied (without the dc bias). This peak diminishes with increasing pressure, a trend that may be explained by transit time effects.

During the ICP power on period, in this case 20 μs in duration, ions will be collected at the RFEA with energies corresponding to the peak of the plasma potential (or with a few volts of Φ_P) if they can transit at least a few cm during the power on period. This distance is from the location of the peak of Φ_P to the RFEA. The majority of this transit occurs in a low electric field region in the bulk plasma as the presheath begins about 4 mm from the RFEA. (See Fig. 4.5.)

With a thermal speed of ions of about 7×10^4 cm/s during the power on pulse, approximately 15-20 μs are required for ions to collisionlessly transit the 1-2 cm required for the ions to arrive at the RFEA with energies near to the peak of Φ_P. This time is approximately the power on period. (50-60 μs would be required to transit from the center of the plasma.) With a mean free path decreasing to 1 mm at 50 mTorr, charge exchange collisions lengthen the transit time in addition to reducing energy at the RFEA, and so reduce the low energy peak.

Varying pressure over the range of a few to 50 mTorr has little effect on the position of the high-energy peak as this energy is primarily determined by the potential of the boundary electrode. The proportion of ions collected in the high energy peak decreases with increasing pressure due to the increasing influence of charge exchange collisions. The lower energy peak reduces in height and shifts to lower energies as the pressure is increased. This is due to the dynamics of the plasma determining the plasma potential, with increased collisionality at higher pressures broadening the peak and lowering T_e, which reduces the Φ_P needed to trap the thermal electrons. At 50 mTorr, the mean free path in the sheath is on the order of the sheath width which means ions will start to have charge exchange collisions even within the sheath.

There is good agreement in the observed trends between the simulated and experimental IEDs in Figs. 4.14a and 4.15a, respectively, but the magnitudes and shape of the IED starts to differ as the pressure increases. When initially simulating IEDs at 28 mTorr and 50 mTorr of pressure, the high energy peaks are not observed in the model. This is an effect of the specified ion collisionality in the model. In the model, the ion momentum transfer cross section is modified to account for the fall off of the cross section as the ion speed increases. This is done by dividing the cross section by a factor of $\left(1 + T_{ion,eff} / TT0\right)$, where $T_{ion,eff}$ is the effective ion temperature and $TT0$ is a user defined parameter, which sets the temperature at which the ion

momentum cross section is half of its uncorrected value.

Originally $TT0$ is set to a value of 10^6 °K, which corresponds to an energy of ≈86 eV. At 24.4 eV, the ion momentum transfer cross section is still 0.78 times its uncorrected value. At higher pressures, with increased gas density, the mean free path is reduced so much that ions cannot cross the sheath without undergoing collisions. Reducing $TT0$ reduces the ion momentum transfer cross section and increases the ion mean free path. This allows a large number of ions to cross the sheath without collisions. $TT0$ is 10^4 °K, which corresponds to an energy of ≈0.86 eV for the results shown in this chapter. This method of controlling ion collisionality in the model may not completely capture the true ion collision dynamics of the experiment, which is a possible source of discrepancy between the computed and experimental IEDs regardless of pressure.

IEDs with a pulsed dc bias of decreasing duration (Δt_{Bias} = 48 to 18 μs) are shown in Fig. 4.14b (experimental results are in Fig. 15b) for an ICP pulse repetition frequency of 10 kHz (pulse period of 100 μs), duty cycle = 20% and dc bias of 24.4 V. The dc bias has a fixed end time of t = 98 μs, and so Δt_{Delay} varies from 28 – 58 μs. The position of the high energy peak collected during the time the dc bias is on is unaffected by the duration of the dc bias, depending only on the value of the dc bias. The height of the peak increases with increasing Δt_{Bias}, which then decreases the peaks at low energy as the entire distribution is normalized to unity, while keeping the shapes nearly the same. The exception is the lowest energy peak (unresolved in the experiments) which increase with decreasing Δt_{Bias}. A decreasing Δt_{Bias} lengthens the time during the afterglow that the plasma potential is at its minimum value and so more low energy ions can be collected. So the proportion of ions between the low and high energy peaks can be controlled with the duration of the dc bias without significantly changing the shapes of either the

low or high energy peaks.

The effects of the pulse repetition frequency on IEDs are shown in Fig. 4.16a for an average ICP power of 120 W, a pressure of 14 mTorr, and a duty cycle of 20% for pulse repetition frequencies of 5 kHz, 7.5 kHz and 10 kHz. The reactor averaged T_e and n_e are shown in Figs. 4.16. A 24.4 V bias is applied beginning at 145, 75, and 45 μs (for 5, 7.5 and 10 kHz) with a duration of Δt_{Bias} = 50 μs. The bias end times for the 5 and 10 kHz cases are 5 μs before the start of the next pulse, while for the 7.5 kHz case the bias ends 9 μs before the start of the next pulse. The overall shapes of the IEDs remain the same with two peaks in the IED - the higher energy peak being narrower and centered at approximately the applied dc bias and the broader lower energy peak centered at the plasma potential during the ICP on phase. A third peak starts to develop at very low energy, ≈ 1 eV, for lower pulse repetition frequencies. Lower pulse repetition frequencies (for a fixed duty cycle) produce longer interpulse periods, which result in more low energy ions being collected when the plasma potential is at its lowest value. The longer period provides more time for ions to thermally diffuse to the sheath. With decreasing repetition rate (and increasing power on period), the reactor averaged T_e is simply extended at its plateau value, thereby extending Φ_P for a longer period. With the longer interpulse period, the electron density decreases to the point that the plasma is resistive enough that the dc bias begins to heat the electrons. This small heating of the electrons is reflected by the small increase in T_e at the end of the 5 kHz cycle.

IEDs are shown in Fig. 4.17 (for the same conditions as for Fig. 4.14b) while varying the duty cycle of the ICP power from 10% to 50%. The dc bias is applied for Δt_{Bias} = 28 μs (70-98 μs) during the 100 μs pulse. The shape of the IEDs and the energies of the peaks are nearly independent of duty cycle. By increasing the duty cycle, the amount of time the plasma potential

and ion production are at the quasi-cw values increases in proportion to the fixed time that V_B is applied. The ion fluxes collected with the energies corresponding to Φ_P and V_B scale with these relative times. For example, the height of the low and high energy peaks of the IEDs are nearly the same (with the peak from the bias slightly larger) for a duty cycle = 20% when the ICP power is on for 20μs and Δt_{Bias} = 28 μs. As the ICP power is on for a larger fraction of the period (higher duty cycle) the low energy peak increases and the high energy peak decreases. If the pulse repetition frequency is high enough and the interpulse period short enough, there is little change in the ion flux during the pulsed period. For these conditions, the relative contributions of the low and high energy peaks to the IEDs can be controlled by the fraction of the pulse period that the ICP power and boundary electrode bias are applied.

4.4 Concluding Remarks

In conclusion, results from computational and experimental investigations suggest that the use of a boundary electrode with a conventional ICP can provide for some control of IEDs incident onto grounded surfaces. For electropositive plasmas sustained in Ar for pressures up to 50 mTorr, application of positive biases result in an increase in the sheath at the grounded surface and an increase in the peak energy of the IED by nearly the applied bias. Negative biases result in a small, limited decrease in the IED peak energy due to the electropositive nature of the plasma that requires that the plasma potential remain positive with respect to ground. Applying a dc bias has a nominal effect on the electron density and temperature due to the low dc power deposition. The exception to these trends is during the late afterglow of a pulsed plasma where the plasma density decreases to a low enough value that the dc power provides measurable heating of the electrons.

Pulsing both the ICP power and dc bias allows for some customization of the IEDs. The

IEDs typically consist of a low energy peak corresponding to the plasma potential during ICP only operation and a high energy peak corresponding to the plasma potential during the dc bias only operation. The relative heights of the peaks are determined by several factors. The primary factor is the ratio of the time the ICP power is on compared to the time the dc bias is applied. These ratios are also controllable by choice of pressure, pulse repetition frequency and duty cycle.

When customizing the IED with, for example, combinations of ICP and dc boundary voltage pulses, ions in low and high energy ranges physically arrive on the substrate at different times. The question then arises whether the time integrated IEDs presented here can be used to represent the reactivity of ions delivered to the substrate. In typical low pressure materials processing plasmas, ion fluxes to the substrate are up to a few 10^{16} $cm^{-2}s^{-1}$. For surface site densities of a few 10^{14} cm^{-2} to 10^{15} cm^{-2}, the average surface site is struck by an ion only every 10-100 ms. So for all practical purposes, surface sites see only time averaged IEDs.

Microelectronics fabrication was the initial motivation for developing techniques to control IEDs. These processes are typically conducted in reactive gases whose ions may have a wide range of molecular weights. It is well known that in rf plasmas, as typically used for materials processing, the width in energy of the IED incident onto the substrate increases with decreasing frequency and decreasing mass [19]. This sensitivity results from the time required for the ion to cross the sheath being less than an rf cycle (producing wider IEDs) or greater than an rf cycle (producing narrower IEDs). It is expected that the techniques for controlling IEDs discussed here will be less sensitive to ion mass than traditional rf excitation provided that the ICP or dc pulse widths are long compared to the ion crossing times. In preliminary modeling, this is confirmed to be the case for ions ranging from H to Xe.

4.5 Figures

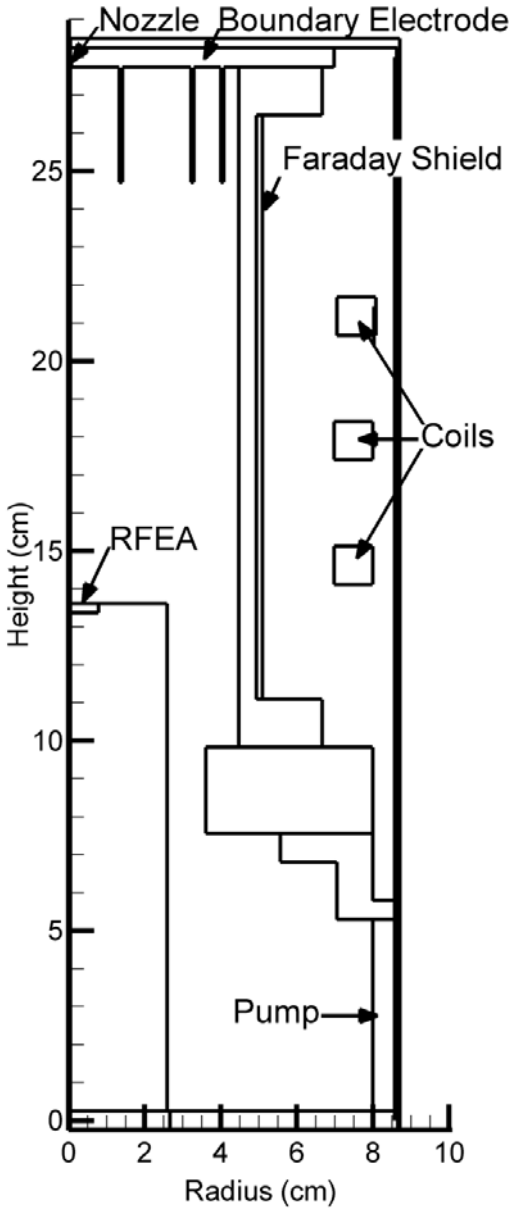

Figure 4.1 Schematic of the Boundary Electrode-Inductively Coupled Plasma (BE-ICP) reactor when measuring ion energy distributions (IEDs) using the RFEA (retarding field energy analyzer). When comparing to experimental results obtained with the Langmuir problem, the RFEA is removed.

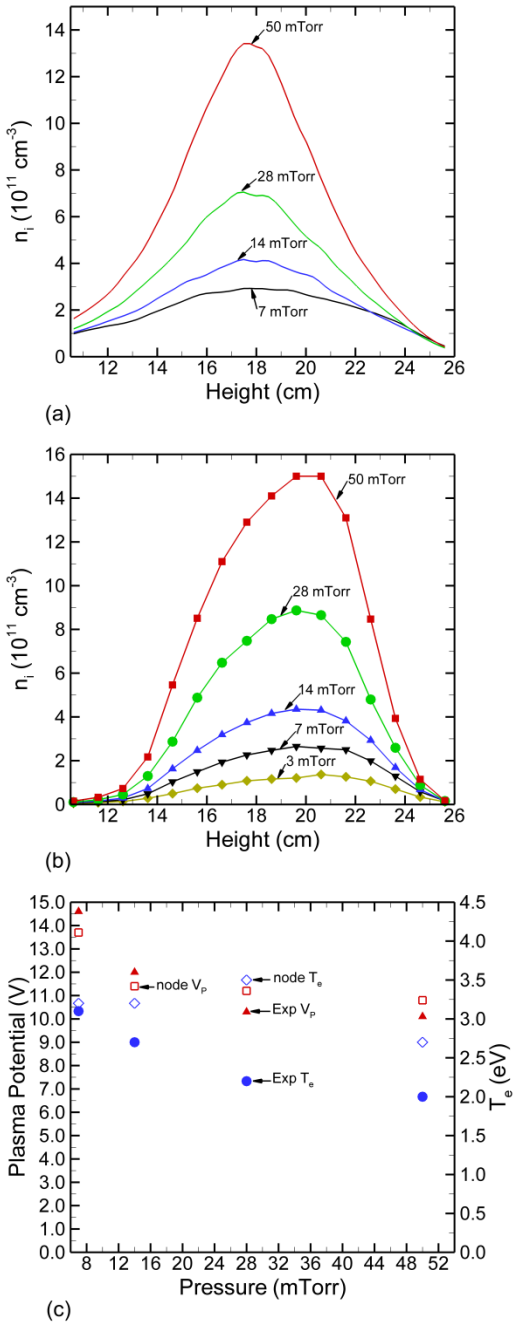

Figure 4.2 Plasma parameters at different pressures for a cw Ar plasma at 300 W and 40 sccm without RFEA. (a) Simulated ion density as a function of height near the axis of symmetry. (b) Experimental ion density as a function of height. (c) Experimental and simulated plasma potential taken on axis at a height of 13.6 cm (height of the RFEA).

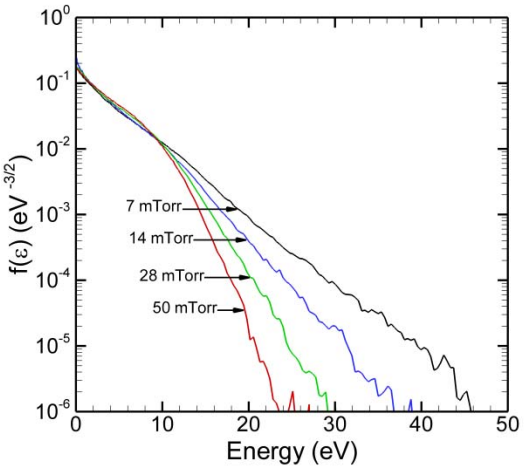

Figure 4.3 Simulated electron energy distributions, $f_e(\varepsilon)$, at different pressures, near skin depth of the electromagnetic wave without the RFEA (r = 3.5 cm, z = 18 cm). Plasma conditions are 300 W (cw) and 40 sccm flow rate. The $f_e(\varepsilon)$ resemble two-temperature distributions.

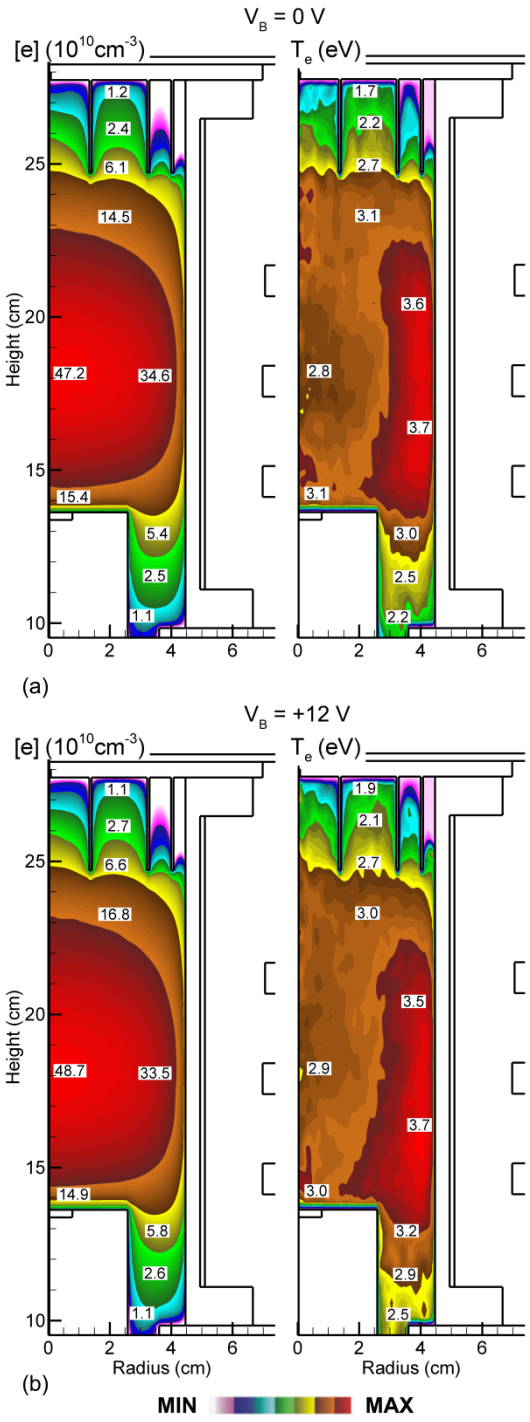

Figure 4.4 Electron density and temperature for two boundary electrode bias voltages. (a) V_B = 0 V. (b) V_B = +12 V. Plasma conditions are argon, 300 W (cw), 14 mTorr, and 40 sccm.

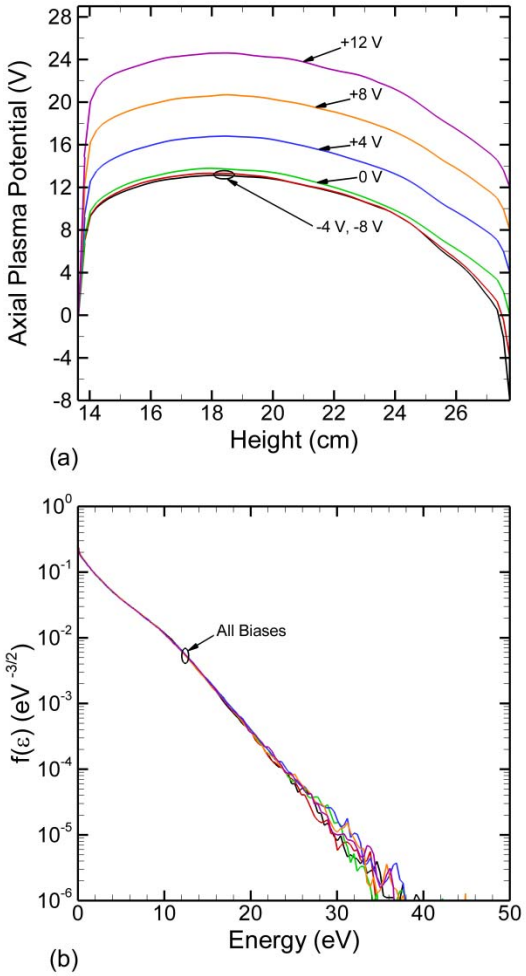

Figure 4.5 Parameters for a cw Ar plasma at 300 W, 14 mTorr, and 40 sccm for different dc biases with the RFEA. (a) Plasma potential as a function of height on axis. (b) Electron energy distributions. $f_e(\varepsilon)$ are shown for V_B from -8 V to 12 V, but are nearly indistinguishable.

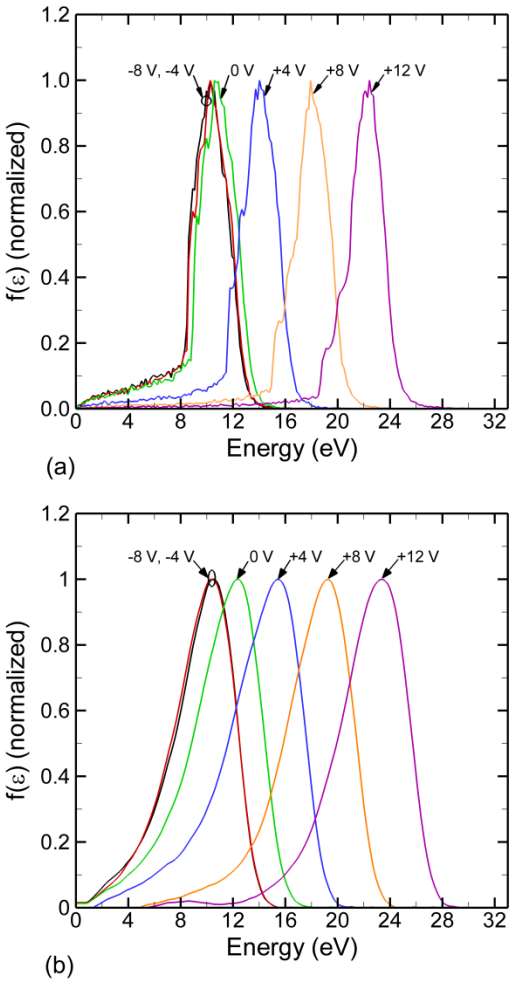

Figure 4.6 Ion energy distributions for different boundary electrode dc biases. (a) Simulated and (b) experimental. The IEDs have been normalized so their peak values are approximately equal. The plasma conditions are Ar, 300 W (cw), 14 mTorr, and 40 sccm. The peak of the IED can be shifted to higher values by approximately the value of V_B.

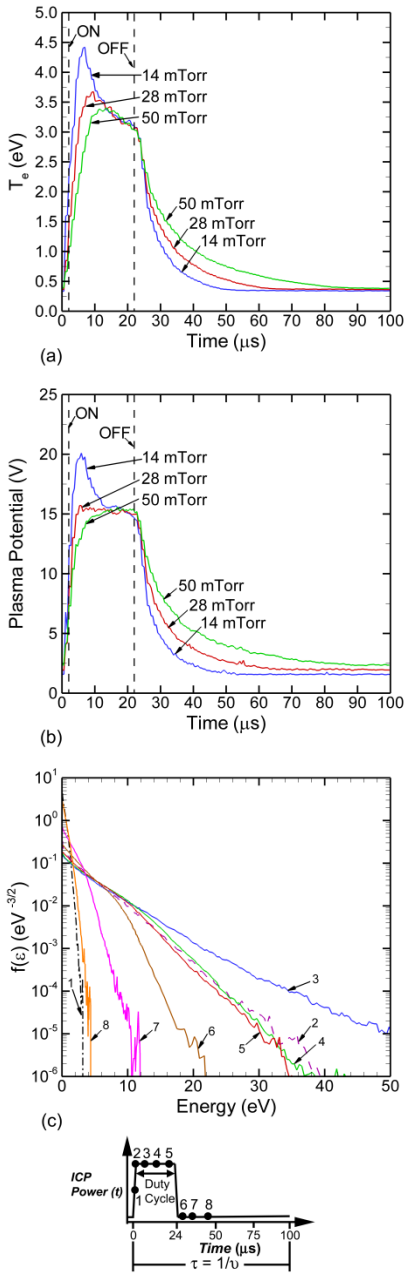

Figure 4.7 Plasma parameters as a function of time for a single pulse of the ICP power without the RFEA. The plasma conditions are argon, 120 W pulsed period averaged power, 40 sccm, pulse repetition frequency = 10 kHz, and 20% duty cycle. (a) Reactor averaged electron temperature at different pressures. (b) Maximum plasma potential at different pressures. (c) Electron energy distribution taken at designated times (points 1-8 on ICP power envelope) at a pressure of 14 mTorr.

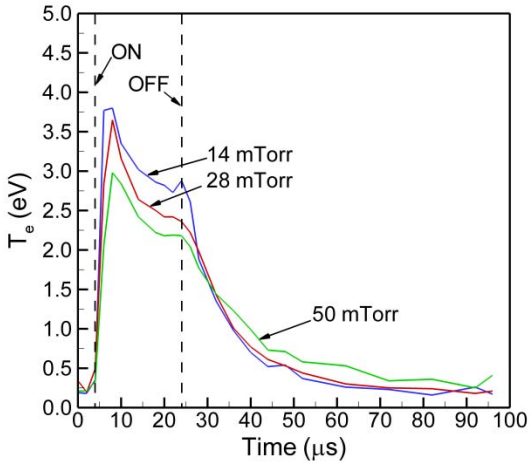

Figure 4.8 Experimental electron temperature as a function of time for a single pulse at different pressures without the RFEA. The plasma conditions are argon, 120 W pulsed period averaged power, 40 sccm, pulse repetition frequency = 10 kHz, and 20% duty cycle.

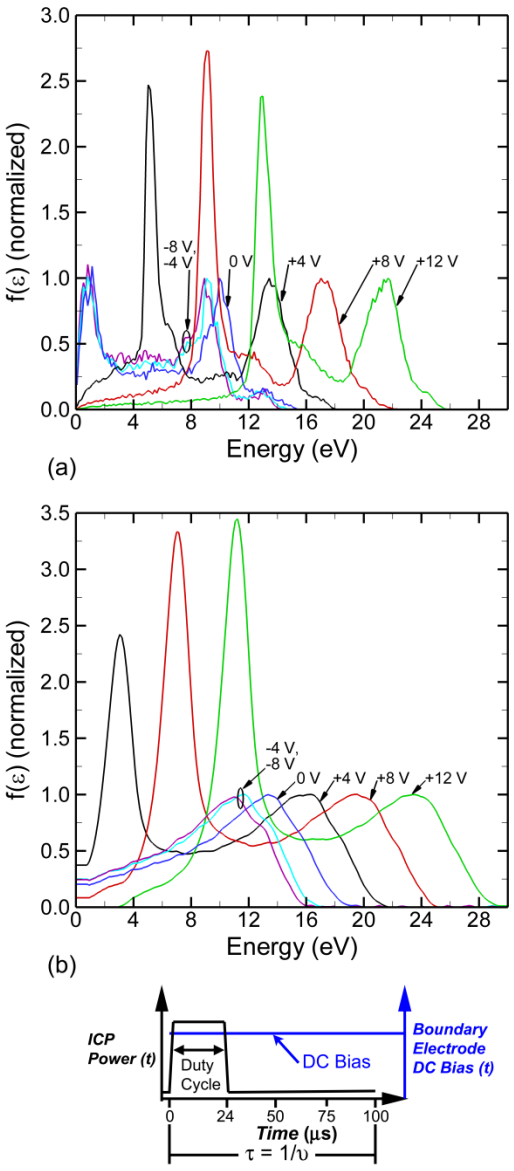

Figure 4.9 Normalized ion energy distributions in pulsed plasma for different dc V_B applied on the boundary electrode. Each distribution is normalized with respect to its peak value during the pulse ON period. The plasma conditions are argon, 120 W pulsed period averaged power, 40 sccm, pulse repetition frequency = 10 kHz, and 20% duty cycle. (a) Simulated and (b) experiments.

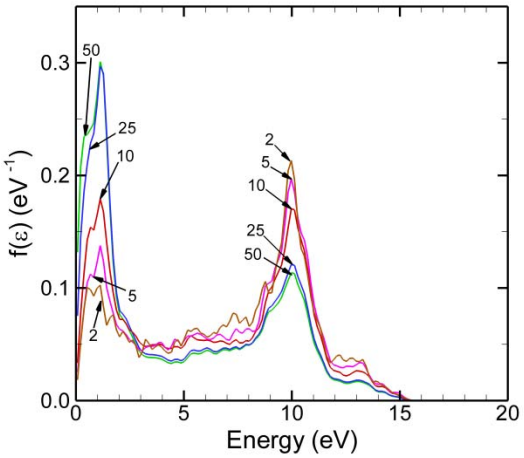

Figure 4.10 Simulated ion energy distributions as a function of ion collection angle (in degrees from normal) from the surface of the RFEA, 2 – 50^0 (FWHM 4-10^0 about the normal). Plasma conditions are argon, 120 W pulsed-period-averaged power, 40 sccm, pulse repetition frequency = 10 kHz, duty cycle = 20% and V_B = 0 V. The efficiency of collecting low energy ions decreases with decreasing collection angle.

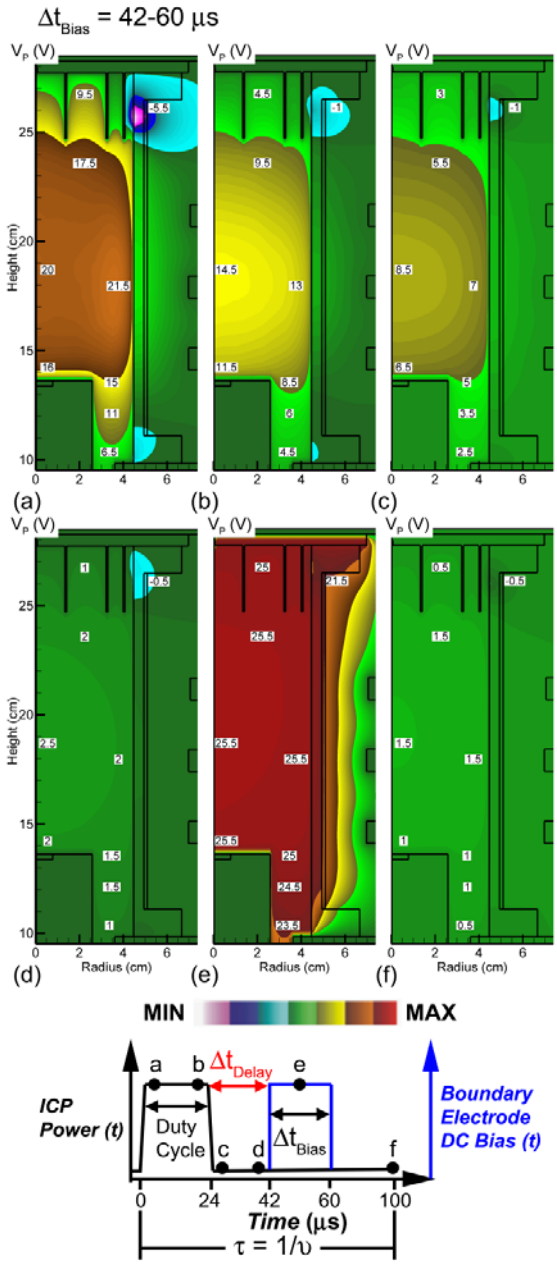

Figure 4.11 Plasma potential at different times during a single pulse for pulsed ICP and pulsed V_B = 24.4 V [Δt_{Bias} = 18 μs (42-60 μs)]. Plasma conditions are argon, 120 W pulsed-period-averaged power, 14 mTorr, 40 sccm, pulse repetition frequency = 10 kHz, duty cycle = 20%. (a) 2 μs after pulse starts. (b) 2 μs before pulse ends. (c) 2 μs after pulse ends. (d) 2 μs before start of applied bias. (e) Middle of applied bias time period. (f) End of pulse. The times of each frame are noted in the waveform. The plasma potential is nearly uniformly elevated by application of V_B.

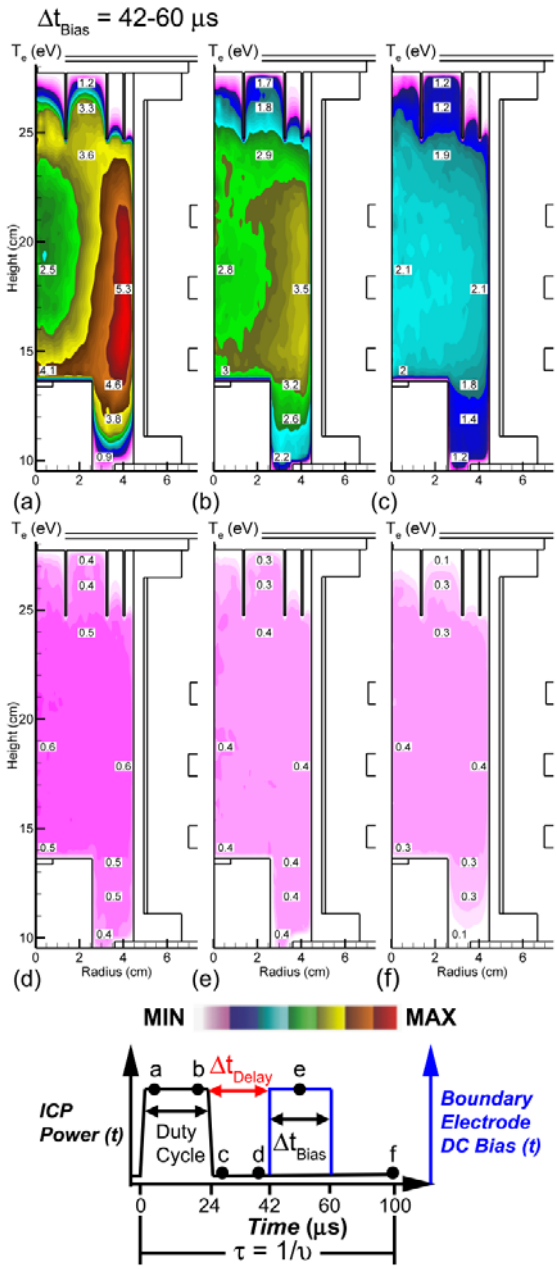

Figure 4.12 Electron temperature at different times during a single pulse for pulsed ICP and pulsed V_B = 24.4 V [Δt_{Bias} = 18 μs (42-60 μs)]. Plasma conditions are argon, 120 W pulsed-period-averaged power, 14 mTorr, 40 sccm, pulse repetition frequency = 10 kHz, duty cycle = 20%. (a) 2 μs after pulse starts. (b) 2 μs before pulse ends. (c) 2 μs after pulse ends. (d) 2 μs before start of applied bias. (e) Middle of applied bias time period. (f) End of pulse. The times of each frame are noted in the waveform. T_e peaks in the skin depth during the pulse and becomes more uniform in the afterglow. Application of V_B does not significantly affect T_e.

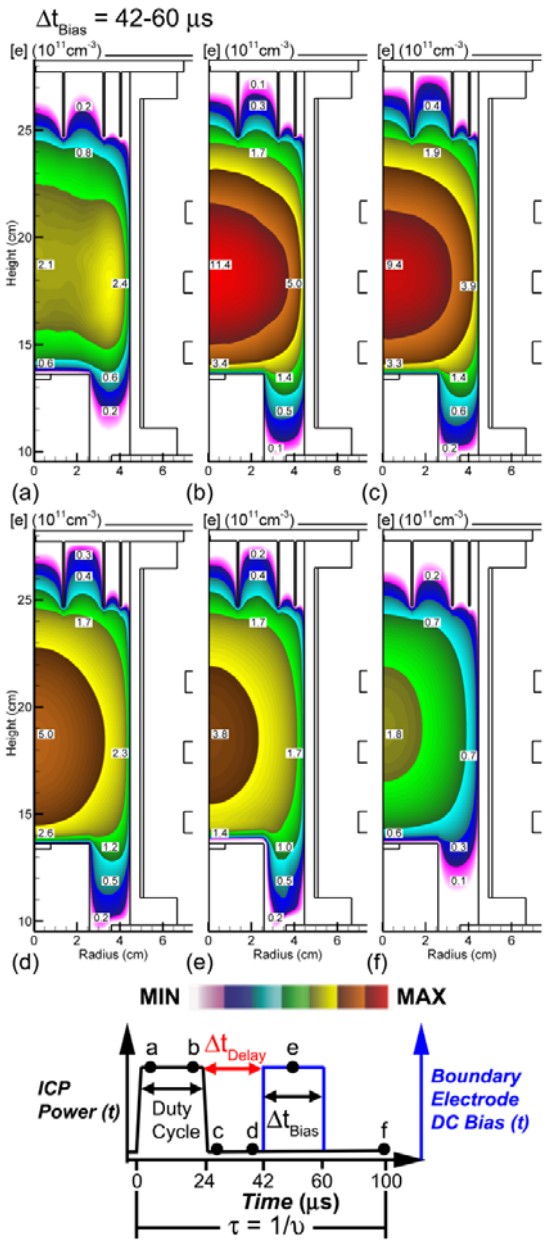

Figure 4.13 Electron density at different times during a single pulse for pulsed ICP and pulsed V_B = 24.4 V [Δt_{Bias} = 18 µs (42-60 µs)]. Plasma conditions are argon, 120 W pulsed-period-averaged power, 14 mTorr, 40 sccm, pulse repetition frequency = 10 kHz, duty cycle = 20%. (a) 2 µs after pulse starts. (b) 2 µs before pulse ends. (c) 2 µs after pulse ends. (d) 2 µs before start of applied bias. (e) Middle of applied bias time period. (f) End of pulse. The times of each frame are noted in the waveform. n_e peaks in the skin depth early during the pulse where the ionization sources are larges, and becomes diffusion dominated later in the pulse and afterglow. Application of V_B does not significantly affect n_e.

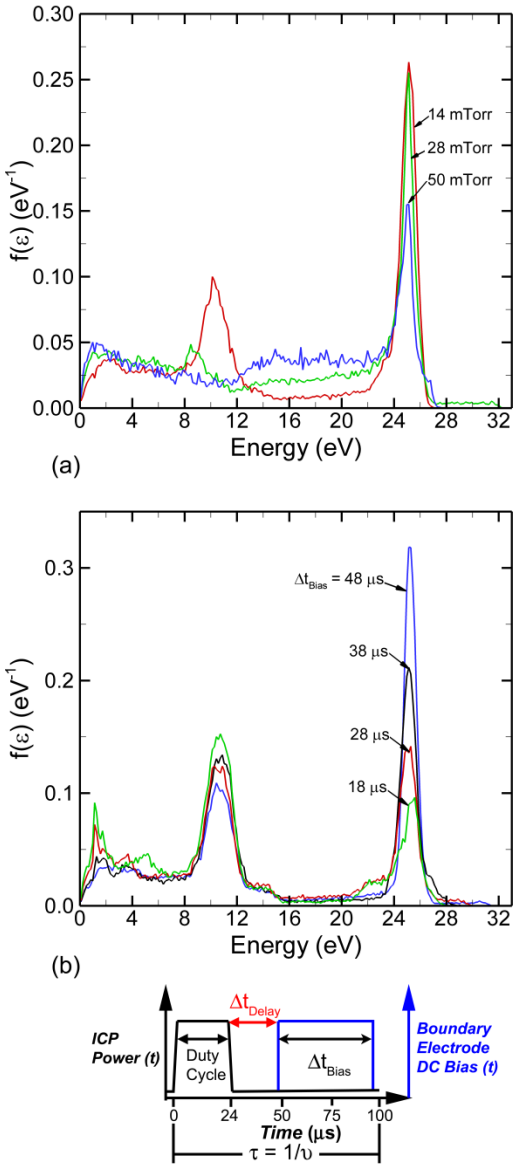

Figure 4.14 Simulated ion energy distributions for pulsed plasma conditions with V_B = 24.4 V applied on the boundary electrode in the afterglow of the ICP at different pressures and bias pulse lengths. Plasma conditions are argon, 120 W pulsed-period-averaged power, 40 sccm, pulse repetition frequency = 10 kHz, duty cycle = 20%. (a) IEDs for a fixed delay time, Δt_{Delay} = 23 μs, and Δt_{Bias} = 50 μs (45-95 μs) at different pressures. (b) IEDs at a fixed pressure of 14 mTorr and fixed dc bias end time of 98 μs. Δt_{Delay} is varied from 28-58 μs which produces Δt_{Bias} = 18 – 48 μs. The high energy peak of the IEDs scale with Δt_{Bias}.

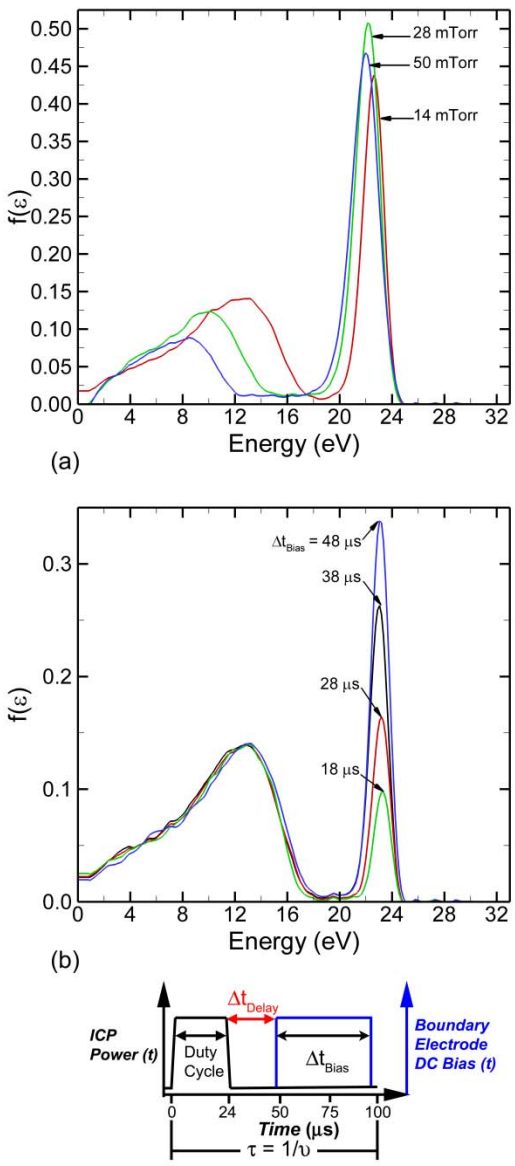

Figure 4.15 Experimental IEDs for pulsed plasma conditions with V_B = 24.4 V applied on the boundary electrode in the afterglow of the ICP at different pressures and bias pulse lengths. Plasma conditions are argon, 120 W pulsed-period-averaged power, 40 sccm, pulse repetition frequency = 10 kHz, duty cycle = 20%. (a) IEDs for a fixed delay time, Δt_{Delay} = 23 μs, and Δt_{Bias} = 50 μs (45-95 μs) at different pressures. (b) IEDs at a fixed pressure of 14 mTorr and fixed dc bias end time of 98 μs. Δt_{Delay} is varied from 28-58 μs which produces Δt_{Bias} = 18 – 48 μs.

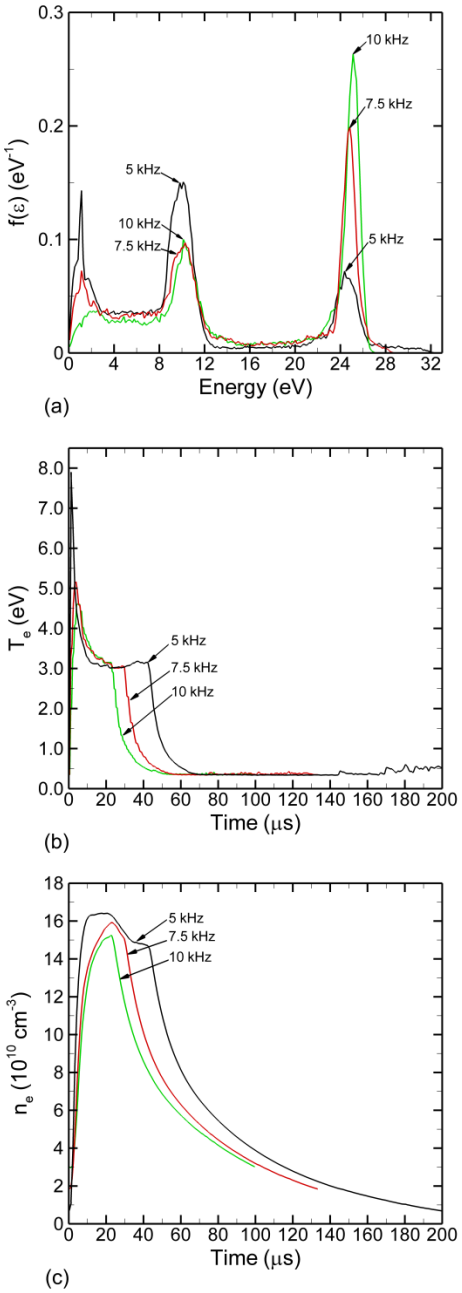

Figure 4.16 Properties for a pulsed plasma for different pulse repetition frequencies with V_B = 24.4 V applied on the boundary electrode in the afterglow of the ICP. Plasma conditions are argon, 120 W pulsed-period-averaged power, 14 mTorr, 40 sccm, duty cycle = 20%. (a) IEDs, (b) electron temperature (the inset shows early times during the pulse) and (c) electron density. V_B was applied for Δt_{Bias} = 50 μs for all cases, over times of 45-95 μs at 10 kHz, 75-125 μs at 7.5 kHz, and 145-195 μs for 5 kHz.

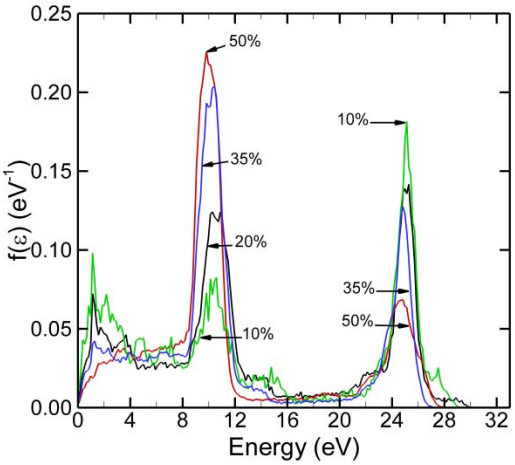

Figure 4.17 Ion energy distributions for a pulsed plasma for different duty cycles with V_B = 24.4 V applied on the boundary electrode in the afterglow of the ICP. Plasma conditions are argon, 120 W pulsed-period-averaged power, 14 mTorr, 40 sccm, pulse repetition frequency = 10 kHz. The bias was applied during a time period Δt_{Bias} = 28 μs (70-98 μs) for all cases. With increasing duty cycle, a larger proportion of ions are collected with energies corresponding to the peak in plasma potential during the ICP pulse.

4.6 References

1. S. -B. Wang and A. E. Wendt, J. Vac. Sci. Technol. A **19,** 2425 (2001).
2. S. D. Athavale and D. J. Economou, J. Vac. Sci. Technol. A **13**, 966 (1995).
3. M. Schaepkens, G. S. Oehrlein, and J. M. Cook, J. Vac. Sci. Technol. B **18**, 848 (2000).
4. M. J. Barela, H. M. Anderson, and G. S. Oehrlein, J. Vac. Sci. Technol. A **23,** 408 (2005).
5. S. Samukawa and T. Mieno, Plasma Sources Sci. Technol. **5**, 132 (1996).
6. S. Banna, A. Agarwal, K. Tokashiki, H. Cho, S. Rauf, V. Todorow, K. Ramaswamy, K. Collins, P. Stout, J.-Y. Lee, J. Yoon, K. Shin, S. Choi, H. Cho, H.-J. Kim, C. Lee, and D. Lymberopoulos, IEEE Trans. Plasma Sci. **37**, 1730 (2009).
7. Agarwal, P. J. Stout, S. Banna, S. Rauf, K. Tokashiki, J.-Y. Lee, K. Collins, J. Appl. Phys. **106**, 103305 (2009).
8. Agarwal, P. J. Stout, S. Banna, S. Rauf, K. Collins, J. Vac. Sci. Technol. A **29**, 011017 (2011).
9. S. -B. Wang and A. E. Wendt, J. Appl. Phys. **88**, 643 (2000).
10. L. Xu, D. J. Economou, V. M. Donnelly, P. Ruchhoeft, Appl. Phys. Lett. **87**, 041502 (2005).
11. P. Kudlacek, R. F. Rumphorst and M. C. M. van de Sanden, J. Appl. Phys. **106**, 073303 (2009).
12. S. H. Lee, P. K. Tiwari, and J. K. Lee, Plasma Sources Sci. Technol. **18**, 025024 (2009).
13. X. V. Qin, Y.-H. Ting, and A. E. Wendt, Plasma Sources Sci. Technol. 1**9**, 065014 (2010).
14. P. Diomede, D. J. Economou, and V. M. Donnelly, J. Appl. Phys. **109**, 083302 (2011).
15. H. Shin, W. Zhu, L. Xu, V. M. Donnelly, and D. J. Economou, Plasma Sources Sci. Technol. **20**, 055001 (2011).
16. S. Banna, A. Agarwal, G. Cunge, M. Darnon, E. Pargon, and O. Joubert, J. Vac. Sci. Technol. A **30**, 040801 (2012).
17. S. Ashida, M. R. Shim and M. A. Lieberman, J. Vac. Sci. Technol. A 14, 391 (1996).
18. Ramamurthi and D. J Economou, Plasma Source Sci. Technol. **11,** 324 (2002).
19. E Kawamura, V Vahedi, M A Lieberman and C K Birdsall, Plasma Source Sci. Technol. **8**, R45 (1999).

Chapter 5 Selective Control of Ion Energy Distributions Using Ion Mass Ratios in Inductively Coupled Plasmas With a Pulsed dc Substrate

5.1 Introduction

In plasma etch processes, such as the etching of SiO_2, there are multiple feed gases which, when sustaining a plasma, produce multiple ionic species. When a bias is applied to the substrate, the ions of the opposite polarity are accelerated through the sheath onto the substrate surface. The effect of this ion flux hitting the surface in conjunction with the neutral flux creates ion enhanced etching of the substrate. This enhanced etching process is a function of the energy of the ions hitting the surface, with higher energy ions producing an increase in the etching rate. However, there is a threshold energy an ion must first reach in order to start the ion enhanced etching process.[1] The sputtering yield as a function of ion energy taken from Ref. 1 is as follows:

$$Y(E) \approx A\left(E_{ion}^{1/2} - E_{th}^{1/2}\right), \tag{5.1.1}$$

where E_{ion} is the ion energy, E_{th} is the threshold energy, and A is a constant. Both the threshold energy and the constant A are a function of the particular ion and substrate combination. While eq. 5.1.1 is directly applicable to sputtering, it can also be used to approximate etching yield in ion enhanced etching processes as the etch rate is driven by ion energy. The constant A will most likely be larger ion enhanced etching than for physical sputtering to account for the much larger yield for ion enhanced etching. In general, the closer the ratio of the ion mass to the mass of the volatile etch products adsorbed on the substrate

surface is to one, the greater the etching yield as the volatile etch products will be more easily removed due to the larger momentum energy transfer.

Ion mass also plays a role in the type of plasma induced damage that occurs in an etching process. At the same energy, lighter ions bombarding a substrate will tend to penetrate deeper than heavier ions. Even though these lighter ions penetrate deeper into a substrate, they are less likely to knock a substrate atom out of the lattice and introduce vacancies. This is still somewhat dependent on the ratio of ion mass to the mass of the substrate atoms. Lighter ions are also generally easier to remove from the substrate through annealing, allowing lower annealing temperatures. Because of these characteristics, lighter ions are less likely than heavier ions to cause a significant degradation on the performance of devices on the substrate.

It would be beneficial if fast etching of a material could be achieved while reducing the amount of plasma damage to the layer underneath the one being etched. Selective control of the peak energy of IEDs for plasma chemistries containing multiple ionic species could help in achieving this. Ions have inertia, with heavier ions having more inertia than lighter ions. For ions with the same charge, lighter ions should accelerate across the sheath faster than heavier ions. The energy an ion has when it hits the substrate surface is largely equal to the potential drop across the sheath as ions convert the potential energy to kinetic energy as they cross the sheath. There is a finite transit time an ion takes to cross the sheath, which is a function of its mass, with heavier ions having longer transit times. If a dc bias is pulsed for a time duration in between the transit time of two ions, the peak energy reached by each ion would be separated in energy as the ion with the longer transit time would not have time to convert the full potential of the dc bias into kinetic energy.

Pulsing the dc bias in a cw plasma creates a double peaked IED on a time averaged basis. In a cw plasma without bias, the sheath potential is constant and the IED is single peaked, meaning it has a single maximum. This maximum will be at approximately the sheath potential. The dc bias increases the potential drop across the sheath and causes ions to bombard the substrate at higher energies than when the bias is off. This creates a second maximum in the IED at approximately the sheath potential with the bias on. The sheath potential and the corresponding peak in the IED when the bias is off is determined by the ICP operating conditions, such as power and pressure. The dc bias should have no effect on the energy at which that peak is located, because by definition it is the IED peak corresponding to when the dc bias is off. What is being proposed is to control the energy at which the second IED peak, generated by the dc bias, is located for a particular ion based on the ratio of the bias on time to the sheath transit time of that ion. The difference in sheath transit time between ions is largely a function of the difference in mass ratio, which is controlled by choice of gas mixture.

For a fixed gas mixture, the difference in energy between the maxima of the IEDs during the bias, which will be referred to in this chapter as the energy selectivity or just selectivity, is controlled by selection of the length of time the bias is applied. If the dc bias is applied for a time longer than the transit time of all ions, then the ions should strike the substrate with approximately the same energy regardless of mass and the energy of the IED peak when the dc bias is on should be the same regardless of mass. Thus, the selectivity can ideally be controlled from no selectivity to very large selectivity. Whether this selectivity control can be achieved and to what degree selectivity control can be achieved will be investigated in this chapter.

The use of dc biases to control IEDs has been investigated in several papers.[2-5] Xu *et al.* experimentally investigated applying a constant dc bias on an acceleration ring surrounding

the discharge region of a pulsed Ar capacitively coupled plasma (CCP).[2] The dc bias was used to raise the plasma potential and push ions out of the plasma. They found that the plasma potential in the afterglow was essentially equal to the dc bias and they were able to extract a nearly monoenergetic ion beam in the afterglow centered at dc bias potential. Diomede *et al.* computationally investigated applying tailored dc bias waveforms in the afterglow of a pulsed Ar CCP, to control IEDs.[3] They found that applying dc bias voltages in the afterglow raised the plasma potential to approximately equal to the dc bias potential. They applied two dc voltages in a "staircase" profile, which resulted in multi-peaked IEDs with peaks resulting from pulsed operation without bias joined by additional peaks at the dc bias potentials applied in the afterglow. They were able to control the relative height of these peaks through control of the time each bias was applied. If one voltage was applied longer than the other, then the peak at that bias potential was larger in magnitude.

Shin *et al.* experimentally investigated the effect of applying dc biases on a boundary electrode in contact with the plasma in an Ar ICP, both in cw as well as pulsed operation. They found that positive dc bias raised the plasma potential and shifted the IEDs by approximately the dc bias voltage. In pulsed operation this allowed for narrow IED peaks at a user selectable energy in the afterglow due to the low afterglow potential without bias. The relative height of these narrow afterglow IED peaks could be controlled by the length of time the bias was applied in the afterglow. Computational modeling of the system of Shin *et al.* was done by this author and compared to their experimental results.[5] The results of this study are the subject of Chapter 4. The same trends were observed in both the experiment and the model.

In this chapter we will discuss the results of a computational simulation of an ICP system where a pulsed dc bias of -100 V is applied to the substrate at different duty cycles and PRFs.

The ICP power is applied in continuous wave (cw) format. Results are for plasmas sustained in either argon/hydrogen (Ar/H_2 = 75/25) or xenon/hydrogen (Xe/H_2 = 75/25). These gas mixtures are chosen due to the large differences in mass between their heaviest and lightest ions. This allows the best opportunity to investigate IED control based on ion mass ratio for ideal conditions. The species in Ar/H_2 consist of Ar (ground state), Ar^*, Ar^{**}, Ar^{***}, Ar^+, ArH^+, H_2 (ground state), $H_2(v = 1 - 5)$, H_2^*, H_2^+, H_3^+, H (ground state), H^*, H^+, H^- and electrons. Ar^* represents the combined metastable states of the $Ar(3p^54s)$ manifold [$Ar(1s_5)$, $Ar(1s_3)$] and Ar^{**} represents the combined radiative states [$Ar(1s_4)$, $Ar(1s_2)$]. Ar^{***} is a lumped state representing $Ar(3p^54p)$ and higher states in the excited state manifold. Radiation trapping of the Ar^{**} state is included. The vibrational states of molecular hydrogen are individually represented from state 1 through state 5. H_2^* represents the combined electronic states of H_2. H^* represents electronic excitation of atomic nitrogen. H^- represents atomic hydrogen with an attached electron. The species in Xe/H_2 consist of Xe (ground state), Xe^*, Xe^{**}, Xe^{***}, Xe^+, as well as the same hydrogen states found in Ar/H_2. Xe^*, Xe^{**}, and Xe^{***} represent electronic excitation to the Xe(6s), Xe(6p), and Xe(6s') states, respectively.

5.2 Description of the Reactor and Experiment

A schematic of the ICP reactor used in the computational investigation is shown in Fig. 5.1. The plasma is sustained in a 25 cm diameter reactor, 16.5 cm tall with a 3-turn planar coil on top of a dielectric window. Gas is injected through a cylindrical nozzle at the top underneath the center coil of the ICP and pumped annularly at the bottom. Computed plasma parameters (electron temperature (T_e), electron density (n_e), and plasma potential (Φ_P)), densities and axial fluxes of the heaviest and lightest positive ions, and IEDs are discussed below for Ar/H_2 and Xe/H_2. IEDs in Ar/H_2 gas mixtures have been investigated previously,[5-7] but not in this

context. In most cases for the Ar/H_2 and Xe/H_2 gas mixtures the ICP is operated in continuous wave (cw) mode at a power of 30 W, at an rf frequency of 10 MHz, with the dc bias on the substrate pulsed at a pulse repetition frequency (PRF) of 500 kHz. There are some cases for both gas mixtures where either the power is set to 300 W or the PRF of the bias is set to 1 MHz. Duty cycles for the dc bias are either 20% or 40%, and the pressure is either 10 mTorr or 100 mTorr.

5.3 Plasma Parameters and IEDs in Ar/H_2 Gas Mixtures

5.3.1 Plasma parameters

2d spatial profiles of the electron density (n_e) and plasma potential (Φ_P) are shown in Fig. 5.2. Snapshots are taken during both the on and off period of the -100 V pulsed dc substrate bias, with a PRF of 500 kHz, while the ICP is operated in cw mode at a power of 30 W and a pressure of 10 mTorr. The applied dc bias on the substrate does not affect the electron density and temperature in the bulk plasma. This is due to the size of the chamber and the low dc power deposition of around 5 W compared to the 30 W of ICP power. This is calculated in the model from the substrate current and voltage during the bias on period. When the large negative dc bias is applied on the substrate, electrons are repelled away from the substrate out of the sheath and into the bulk plasma as a cathode fall forms. The large negative bias causes the sheath width to double from ≈0.4 cm to ≈0.8 cm.

It is not completely clear why the potential drops so significantly in the bulk plasma but a possible explanation is as follows. On a reactor averaged basis, the H^- ions make up ≈34% of the negative charge. The negative ions are concentrated in the upper half of the chamber near the top dielectric. When the -100 V dc bias is applied to the substrate, electrons within the cathode fall region are repelled by the bias toward the bulk plasma almost instantly. The negative bias drives a dc current, carried by electrons, through the plasma from the biased electrode toward

ground. This drives current toward the dielectric window at the top of the chamber in the form of an electron flux, which charges the dielectric. At the biased electrode, positive ions carry current to the electrode. The small electric field in the bulk plasma before the bias is applied is not enough to sustain this current and so a potential gradient develops in the bulk plasma. This happens very fast, within a 100 ns.

The negative ions are confined to the plasma by the ambipolar potential. The negative potential of these ions will tend to reduce the flux of positive ions to the sheaths. To counter this effect, and allow enough positive ion current to maintain current continuity to reach the biased electrode, the larger initial potential gradient in the bulk plasma is maintained during the bias. The negative ions also will generate an attractive force that reduces positive ion flux to the dielectric, which will cause the dielectric to become negatively charged. This in turn reduces the potential in the bulk plasma near the dielectric window. This would reduce the electric field in the bulk below what is needed to maintain the dc current and so the entire bulk plasma potential has to drop. This process is repeated throughout the pulse as the plasma tries to maintain current continuity. Because of this drop in plasma potential throughout the bulk plasma, the potential drop across the sheath during the bias on period is not the full 100 V but ≈92 V.

2d spatial profiles of the density of the lightest and heaviest ions in the system, H^+ and ArH^+ respectively, under the same conditions are shown in Fig. 5.3. Images are shown of the density profile during both the on and off period of the pulsed dc substrate bias while the ICP is operated in cw mode. The ArH^+ ions have an order of magnitude higher density than H^+ throughout the plasma. The peak densities for the two ions are $\approx 8.5 \times 10^8$ cm^{-3} and $\approx 4.4 \times 10^7$ cm^{-3} respectively. The most likely reason for the relatively low H^+ ion density is the low ICP power of 30 W, which leads to a low dissociation rate of the neutral hydrogen gas. The density

profiles of the ions do not change, except near the sheath edge. The density does not change in the bulk of the plasma because the dc bias power is small compared to the ICP power (<1 W) and is applied for short bursts of time so the substrate bias power is not enough to ignite the plasma. The application of a large dc bias accelerates ions in the sheath and near the sheath edge toward the substrate. The lighter hydrogen ions are able to be accelerated fast enough to be swept across the sheath to the substrate when the bias is on. The sheath transit times for H^+, H_2^+, and H_3^+ ions are ≈105 ns, ≈153 ns, and ≈183 ns respectively. This results in a noticeable change in density near the sheath edge during the pulsing of the dc bias since the dc bias length is (≈400 ns FWHM and ≈300 ns at peak voltage) at a duty cycle of 20%. The heavier Ar^+ and ArH^+ ions, with masses 40 and 41 times that of H^+, are accelerated across the sheath at a rate 40-41 times slower than H^+ and have sheath transit times of ≈661 ns for Ar^+ and ≈649 ns for ArH^+. Heavier ions in the sheath are thus not able to respond to the pulsing of the dc bias fast enough for the density to change noticeably even near the sheath edge.

2d spatial profiles of the axial flux of the lightest and heaviest ions in the system, H^+ and ArH^+ respectively, are shown in Fig. 5.4. The fluxes of the ions to the substrate change by less than a factor of 2 with a -100 V bias applied to the substrate. On average, ions enter the sheath at approximately an average thermal speed but are accelerated by the sheath potential and so their effective velocity in the sheath is greater than their thermal velocity entering the sheath. For example, H^+ has an axial velocity entering the sheath of $\approx 2.8 \times 10^6$ cm/s at 10 mTorr. The sheath potential with no bias applied is ≈9.5 V and the corresponding sheath transit time is ≈101 ns. When the dc bias is applied, the sheath width doubles and the axial velocity of H^+ at the new sheath edge is $\approx 1.85 \times 10^6$ cm/s. With a sheath potential of ≈92 V, the sheath transit time is ≈105 ns. The sheath transit time with the bias applied is computed to be larger than with no bias

applied, which is not expected to be the case as the sheath electric field is larger. However, the transit time is being calculated from the sheath edge, which is twice as far from the substrate with a bias applied leading to the slightly longer transit time. Since the sheath transit time is almost the same while the sheath width doubles, the effective velocity in the sheath must have increased by a factor of ≈2. If the density of ions in the sheath remains the same, then the flux should also increase by a factor of 2. However, the bias does not affect the speed at which ions enter the sheath, so the rate at which ions are leaving the sheath is faster than the rate at which they are entering. The effect of bias on the speed at which ions enter the presheath is ignored. This reduces the density of ions in the sheath during the bias pulse and reduces the increase in the axial flux of H^+ to less than a factor of two during the pulse. This same principle holds true for ArH^+.

5.3.2 Ion energy distributions

The effect of very short duration dc bias pulses on the time averaged IEDs hitting the substrate is examined to see if a separation in the maxima in the IEDs of the ions can be observed. IEDs for the five ions formed in the ArH_2 discharge at two pressures and two duty cycles are shown in Fig. 5.5 for an ICP power of 30 W and a bias PRF of 500 kHz. In these cases a -100 V dc bias is applied in pulsed mode to the substrate and the selectivity of the IEDs between the heaviest (ArH^+) and lightest (H^+) ions are determined. In this case the selectivity between two ionic species is defined as the difference in energy between the high energy peaks of the two ions.

In this gas mixture it is observed that even though there is a factor of 40 difference in the masses of the ArH^+ and H^+ ions, the selectivity between them is less than 8 eV under all conditions. At a 20% duty cycle, the selectivity is ≈7.7 eV and ≈3.4 eV for a pressure of 10

mTorr and 100 mTorr, respectively. At a 40% duty cycle, the selectivity is ≈3.3 eV and ≈1.5 eV for a pressure of 10 mTorr and 100 mTorr respectively. Going from 10 mTorr to 100 mTorr in pressure causes the selectivity to decrease by approximately 55% and also causes the IEDs of all the ions to shift down in energy. This is most likely due to shorter mean free paths at higher pressure leading to increased charge exchange collisions between the ions. At 10 mTorr, calculated mean free paths (MFPs) at the sheath edge for H^+ and ArH^+, based on their respective dominant charge exchange collision, are: ≈289 cm for H^+ and ≈9.1 cm for ArH^+. At 100 mTorr the calculated MFPs are: ≈12.9 cm for H^+ and ≈0.46 cm for ArH^+.

At 10 mTorr, the axial speed of H^+ entering the sheath is approximately 1.85×10^6 cm/s and the axial speed of ArH^+ is approximately 3.6×10^5 cm/s. In general, the rate at which the potential changes with position in the sheath increases with distance into the sheath from the sheath edge. This results in the electric field and ion acceleration in the sheath also increasing with distance into the sheath from the sheath edge. This is not the case in the model. In the model, the majority of the plasma potential is dropped across the first computational mesh cell above the substrate. The potential is interpolated to vary linearly across the mesh cell. Thus in the model, the acceleration, a, of an ion from the sheath potential is approximately equal to

$$q\left|V_{sheath}\right|/m_{ion}w_{sheath}\,, \tag{5.3.1}$$

where q is the elementary electric charge, $\left|V_{sheath}\right|$ is the voltage dropped across the sheath, ≈85 V in this case, m_{ion} is the mass of the ion, and w_{sheath} is the sheath width during the bias, which is found to be ≈0.5 cm. Assuming collisionless transport through the sheath, which should be acceptable considering the calculated MFPs, the transit time for an ion through the sheath, t_{tr}, can be estimated by solving eq. 5.3.2 for the distance traveled by an object under constant acceleration

$$w_{sheath} = x_0 + v_0 t_{tr} + 0.5 a t_{tr}^2, \quad (5.3.2)$$

where x_0 is the initial position and equal to 0, and v_0 is the initial velocity equal to the average thermal velocity. By solving equation 5.3.2 for t_{tr}, the transit time for H^+ and ArH^+ is found to be ≈105 ns and ≈649 ns, respectively, during the applied bias period.

At 100 mTorr, the axial speed of H^+ entering the sheath is approximately 8.86 x 10^5 cm/s and the axial speed of ArH^+ is approximately 1.43 x 10^5 cm/s. By again solving equation 5.3.2 for t_{tr}, the transit time for H^+ and ArH^+ is found to be ≈113 ns and ≈720 ns respectively during the applied bias period. The MFP of ArH^+ at 100 mTorr, at ≈0.46 cm is slightly less than the sheath width, 0.8 cm, but since most likely only one collision would occur during transport through the sheath, assuming one actually occurs, it is believed a reasonable estimate for t_{tr} can be given assuming collisionless sheath transport. If charge exchange collisions in the sheath have a significant impact on ArH^+ transport then the IED peak energy will be much less than observed at 100 mTorr of pressure. Assuming that ArH^+ undergoes one charge exchange collision with H_2 after traveling 0.46 cm in the sheath, then a new H_3^+ ion would be created. It would only travel .34 cm before hitting the substrate. With an electric field of ≈125 V/cm with a -100 V dc bias, the new H_3^+ ion would hit the substrate with an energy of ≈42 eV. Since there is no peak in the H_3^+ IED at that energy, there must not be a significant amount of charge exchange collisions in the sheath.

The transit time for H^+ ions through the sheath is shorter than the duration of the applied bias regardless of duty cycle, and thus they are able to bombard the substrate at an energy approximately equal to the applied bias potential, which is dropped across the sheath. The transit time of ArH^+ ions is longer than the duration of the applied bias with a 20% duty cycle (≈400 ns FWHM and ≈300 ns at peak voltage), but shorter than the duration of the applied bias at 40%

duty cycle (≈800 ns FWHM and ≈700 ns at peak voltage). Since the ArH^+ ions take longer than the applied bias time to traverse the sheath, at 20% duty cycle, they see an average sheath potential lower than the dc bias potential and do not gain as much energy. This explains what is observed in Fig. 5.5 in that an increase in duty cycle at the same pressure, which means longer pulse on times for the dc bias, leads to a reduction in selectivity between H^+ and ArH^+ of ≈55%.

The ratio of the transit time of ArH^+ to the pulse on time decreases as the pulse on time increases. When the ratio of transit time across the sheath to dc bias length for an ion is less than or equal to one, then the ion should be able to gain the full sheath potential excluding collisions. If this is the case for a pair of ions, then the maximum in the IED during the bias should ideally be at the same energy for both ions. This leads to a selectivity of 0 eV based on the definition of selectivity given earlier. At 100 mTorr increased collision rates reduce the ion temperature at the sheath edge, which changes the IED of the ions entering the sheath. Assuming a Maxwellian distribution of ions entering the sheath, the energy at which the peak in the IED occurs, as well as the high energy tail of the IED will be reduced. This leads to a downshifted IED at the substrate for the same applied bias. The slightly longer sheath transit time for ArH^+ would also cause those ions to see a lower average sheath potential than at 10 mTorr for the 20% duty cycle case.

IEDs for the five ions formed in the ArH_2 discharge at 10 mTorr and 100 mTorr are shown in Fig. 5.6 for an ICP power of 30 W, a bias duty cycle of 20% and a bias PRF of 1MHz. The selectivity between H^+ and ArH^+ now increases by ≈29.0 eV to ≈36.7 eV at 10 mTorr and by ≈36.9 eV to ≈40.3 eV at 100 mTorr. These results show that for the same duty cycle and pressure shorter bias periods allow for greater selectivity between IED high energy peaks using mass ratios. Increasing the PRF to 1MHz reduces the dc bias duration time by a factor of 2 in

the FWHM and by a factor of 3 in the duration time of the peak voltage (≈200 ns FWHM and ≈100 ns at peak voltage). The sheath transit time of H^+ remains less than the applied bias time at both pressures while the sheath transit time for ArH^+ is now significantly longer than the applied bias time. This is the source of the increase in selectivity at a PRF of 1 MHz. The duty cycle is kept at 20% to show that it is the absolute bias duration time that matters most, not duty cycle, in determining selectivity. This is because the ratio of the ion sheath transit time to bias on time for an ion is the determining factor in its ability to gain the full energy of the applied dc bias potential.

The values of these ratios for a pair of ions, and whether one or both has a value greater than or equal to one, determines the selectivity between those ions. IEDs at 10 mTorr and 100 mTorr showing the effect of ICP power are shown in Fig. 5.7 for an ICP power of 30 W and 300 W, with a bias duty cycle of 20% and a bias PRF of 500 kHz. The IEDs show the same general shape and trends for 300 W as for 30 W. The IED peaks extend to slightly higher energies at 300 W. The selectivity at 10 mTorr is reduced from ≈7.7 eV at 30 W to ≈4.3 eV at 300 W. The selectivity at 100 mTorr is reduced from ≈3.4 eV at 30 W to ≈0 eV at 300 W.

At 300 W, the reactor averaged negative ion density is only a small fraction (<1%) of the total negative charge density and the bulk plasma potential does not drop with applied bias. At 10 mTorr, this creates a sheath potential of ≈109.5 V which reduces the sheath transit time of ArH^+ to ≈615 ns. Even with this large sheath potential, the sheath transit time is slightly more than the FWHM time of ≈400 ns and more than the peak bias time of ≈300 ns. The sheath potential is also increased at 100 mTorr, which reduces the transit time and reduces selectivity. IEDs at 10 mTorr and 100 mTorr showing the effect of ICP power at a PRF of 1 MHz are shown in Fig. 5.8 for an ICP power of 30 W and 300 W, with a bias duty cycle of 20%. The IEDs show

the same general shape and trends for 300 W as for 30 W. The IED high energy peaks extend to higher energies at 300 W. The selectivity at 10 mTorr stays the same at ≈36.7 eV at both powers. The selectivity at 100 mTorr increases slightly from ≈40.3 eV at 30 W to ≈41.8 eV at 300 W. These results show that if the bias on time is chosen correctly then high selectivity does not require low ICP power. This makes this technique more suitable for industrial applications, although the short bias times mean the high energy IED peak is much lower in magnitude than the low energy peak.

Also of note, selectivities are based on the difference in energy between the high energy peaks, with the energies of the peaks considered to be the energy of the middle of the peak. This does not take into account the energy width of the peaks, which means there could still be a significant overlap in the IED peaks even if the selectivity is 10s of eV. This can be a problem in plasma etching processes. Having a broad IED can lead to increased plasma induced damage from a larger flux of ions at energies higher than desired for a particular process.

5.4 Plasma Parameters and IEDs in Xe/H_2 Gas Mixtures

5.4.1 Plasma parameters

2d spatial profiles of the electron density (n_e), and plasma potential (Φ_P) are shown in Fig. 5.9. The snapshots are taken during the on and off period of the pulsed dc substrate bias, with a PRF of 500 kHz, while the ICP is operated in cw mode at a power of 30 W and a pressure of 10 mTorr. The applied dc bias on the substrate does not affect the electron density in the bulk plasma the same as in Ar/H_2. When the large negative dc bias is applied on the substrate, electrons are repelled away from the substrate out of the sheath and into the bulk plasma, which reduces n_e near the substrate just as in Ar/H_2. On a reactor averaged basis, the positive hydrogen ions make up ≈0.2% of the positive charge and H^- ions make up ≈2.1% of the negative charge.

The distribution of these fairly mobile ions, which can quickly respond to the applied bias, no longer significantly affects the bulk plasma potential and the potential drop across the sheath is approximately the full bias voltage, ≈100 V.

2d spatial profiles of the density of the lightest and heaviest ions in the system, H^+ and Xe^+ respectively, under the same conditions are shown in Fig. 5.10. The figure includes the profiles during both the on and off period of the pulsed dc substrate bias. As was the case in the Ar/H_2 gas mixture, the density profiles of the ions do not change except near the sheath edge. The application of a large dc bias accelerates ions in the sheath and near the sheath edge toward the substrate. The lighter hydrogen ions are able to be accelerated fast enough to be swept across the sheath to the substrate when the bias is on. This results in a noticeable change in density near the sheath edge during the pulsing of the dc bias. Xe^+ ions are much heavier than even ArH^+, with a mass 130 times that of H^+, and over 3 times that of ArH^+. The Xe^+ ions are accelerated across the sheath at a rate 130 times slower than H^+ and are not able to respond to the pulsing of the dc bias fast enough for the density to change noticeably even near the sheath edge.

2d spatial profiles of the axial flux of the lightest and heaviest ions in the system, H^+ and Xe^+ respectively, under the same conditions are shown in Fig. 5.11. The change in flux with bias is the same as in the Ar/H_2 gas mixture, with the flux of the ions to the substrate changing by less than a factor of 2 with a -100 V bias applied to the substrate. The reasons for this are the same as in Ar/H_2. On average, ions enter the sheath at some average thermal speed, but are accelerated by the sheath potential and so their effective velocity in the sheath is greater than their thermal velocity entering the sheath. When the dc bias is on, the effective velocity is increased; however, the bias does not affect the speed at which ions enter the sheath. Therefore, the rate at which ions are leaving the sheath is faster than the rate at which they are entering. This reduces the density

of ions in the sheath during the bias pulse and reduces the increase in the axial flux of H^+ to less than a factor of two during the pulse. This holds true for Xe^+ as well. As in Ar/H_2, the effect of bias on the speed at which ions enter the pre-sheath is ignored and the sheath width doubles with bias from ≈0.4 cm to ≈0.8 cm.

5.4.2 Ion energy distributions

IEDs for the ions formed in the XeH_2 discharge at two pressures and two duty cycles are shown in Fig. 5.12 for an ICP power of 30 W and a bias PRF of 500 kHz. In these cases, as was the case in the Ar/H_2 gas mixture, a -100 V dc bias is applied in pulsed mode to the substrate and the selectivity of the IEDs between the heaviest (Xe^+) and lightest (H^+) ions are determined.

In this gas mixture it is observed that the factor of 130 difference in the masses of the Xe^+ and H^+ ions, allows for a significantly greater selectivity to be observed than in Ar/H_2. At a 20% duty cycle, the selectivity is ≈34.5 eV and ≈42 eV for a pressure of 10 mTorr and 100 mTorr respectively. At a 40% duty cycle, the selectivity is ≈1.5 eV and ≈2.1 eV for a pressure of 10 mTorr and 100 mTorr respectively. These results emphasize the importance of the difference in the ratio of ion transit time to the bias duration time between two ions in determining the selectivity between the ions. At 40% duty cycle, the bias is applied so long that the ion transit time for all ions are essentially less than or equal to the duration of the applied bias. Even though Xe^+ ions are over three times heavier than ArH^+ ions, they can still transit through the sheath fast enough to gain roughly the full bias potential.

Going from 10 mTorr to 100 mTorr in pressure causes the selectivity to actually increase by approximately 22% and 40% for a duty cycle of 20% and 40% respectively. This is in contrast to what was observed in Ar/H_2. This is due to the fact that increasing pressure again causes the IEDs of all the ions to shift down in energy; however, the Xe^+ IED shifts down

slightly more than the IEDs for the hydrogen ions. This shifting in energy is believed to be due to shorter mean free paths at higher pressure leading to increased charge exchange collisions between the ions just as in Ar/H_2. At 10 mTorr, calculated mean free paths (MFPs) at the sheath edge for H^+ and Xe^+, based on their respective dominant charge exchange collision, are: ≈270 cm for H^+ and ≈7.3 cm for Xe^+. At 100 mTorr, the calculated MFPs are: ≈11.1 cm for H^+ and ≈.29 cm for Xe^+.

At 10 mTorr, the axial speed of H^+ entering the sheath is approximately 1.84×10^6 cm/s and the axial speed of Xe^+ is approximately 1.32×10^5 cm/s. Solving equation 5.3.2 for t_{tr}, the transit time for H^+ is found to be ≈98 ns and the transit time for Xe^+ is found to be ≈1.14 μs. As was the case in Ar/H_2, the transit time for H^+ ions through the sheath is shorter than the duration of the applied bias regardless of duty cycle, and thus they are able to bombard the substrate at an energy approximately equal to the applied bias potential dropped across the sheath (plus their initial kinetic energy entering the sheath). The transit time of Xe^+ ions is significantly longer than the duration of the applied bias with for both a 20% duty cycle (≈400 ns FWHM and ≈300 ns at peak voltage) and a 40% duty cycle (≈800 ns FWHM and ≈700 ns at peak voltage).

Since the Xe^+ ions take longer than the applied bias time to traverse the sheath, at 20% duty cycle, they see an average sheath potential lower than the dc bias potential and do not gain as much energy. The slower ion transit time of Xe^+ ions as compared to ArH^+ ions mean the average sheath potential the Xe^+ ions see as they traverse the sheath is even less than what the ArH^+ ions see. Thus, based on the increased mass ratio of Xe^+ to H^+ compared to the mass ratio of ArH^+ to H^+, there is higher selectivity between the IED peaks.

At 100 mTorr, the transit time for H^+ and Xe^+ is found to be ≈111 ns and ≈1.27 μs, respectively, during the applied bias period. The MFP of Xe^+ at 100 mTorr of ≈0.29 cm is less

than the sheath width, 0.8 cm, and it is possible that collisions occur in the sheath. However, it can still be used to demonstrate how the ratio of sheath transit time to applied bias time for Xe^+ affects the IED and selectivity.

IEDs for the ions formed in the XeH_2 discharge at 10 mTorr and 100 mTorr and a duty cycle of 20%, are shown in Fig. 5.13 for an ICP power of 30 W and a bias PRF of 1MHz. The selectivity between H^+ and Xe^+ increases by ≈36.9 eV of eV to ≈71.4 eV at 10 mTorr and by ≈33.4eV to ≈75.4 eV at 100 mTorr. These results again show that for the same duty cycle and pressure, shorter bias periods allow for greater selectivity between IED high energy peaks using mass ratios. It also emphasizes that it is the absolute bias duration time that matters most, not duty cycle, in determining selectivity.

IEDs at 10 mTorr and 100 mTorr showing the effect of ICP power are shown in Fig. 5.14 for an ICP power of 30 W and 300 W, with a bias duty cycle of 20% and a bias PRF of 500 kHz. The IEDs show the same general shape and trends for 300 W as for 30 W. The IED peaks extend to slightly higher energies at 300 W. The larger ICP power leads to an increase in the temperature of Xe^+ ions, which leads to an increased flux of higher energy ions and a broader IED entering the sheath. The selectivity at 10 mTorr is increased from ≈34.5 eV at 30 W to ≈39 eV at 300 W although the peak is so broadened at 300 W that this value may not be accurate. The selectivity at 100 mTorr is reduced from ≈42 eV at 30 W to ≈40.8 eV at 300 W. This again may be due to the increased number of high energy Xe^+ ions broadening the peak. IEDs at 10 mTorr and 100 mTorr showing the effect of ICP power at a PRF of 1 MHz are shown in Fig. 5.15 for an ICP power of 30 W and 300 W, with a bias duty cycle of 20%. The IEDs show the same general shape and trends for 300 W as for 30 W. The IED peaks stay at roughly the same energy. Both the high and low energy IED peaks decrease in magnitude going from 30 W to 300

W; however, only the high energy peaks broaden in energy. The selectivity at 10 mTorr increases slightly from ≈71.4 eV at 30 W to ≈72.7eV at 300 W powers. The selectivity at 100 mTorr increases slightly from ≈75.4 eV at 30 W to ≈77.1 eV at 300 W. Again note that the definition of selectivity found in this chapter does not take into account the Full Width Half Maximum (FWHM) of the peaks, meaning there could still be a significant overlap in the IED peaks even if the selectivity is several eV.

5.5 Concluding Remarks

In conclusion, results from computational investigations suggest that the use of short dc bias pulses on the substrate can be used to control IEDs on the substrate in systems with multiple ionic species based on the mass difference between the ions. The energy selectivity, which is defined as the separation in energy between the high energy peaks of two ions, can be controlled by the selection of the bias duration time. The source of this energy selectivity is the difference in sheath transit times of ions, based on their mass differences. When the ratio of transit time across the sheath to dc bias length for an ion is less than or equal to one, then the ion should be able to gain the full sheath potential, excluding collisions. The values of these ratios for a pair of ions, and whether one or both has a value greater than or equal to one, determines the selectivity between those ions. If two ions both have a ratio less than or equal to one, then the selectivity between them should ideally be 0 eV. This ignores any differences in energy before entering the sheath which should be small.

If an applied bias time is chosen that is longer than the sheath transit time of one ion and shorter than the transit time of another, a difference in energy between the bias generated peaks of the two ions will develop. The ion with the longer sheath transit time will have a bias generated peak at a lower energy than the ion with the shorter sheath transit time. In an Ar/H_2

mixture, the sheath transit time for the heaviest ion, ArH^+, is slightly over 400 ns at 10 mTorr and 100 mTorr, while the transit time for the lightest ion, H^+, is under 100ns at both pressures. When the bias duration time is only slightly less than ArH^+ sheath transit time, ≈400 ns FWHM and ≈300 ns at peak voltage, the selectivity between it and the lightest ion, H^+, is less than 8 eV. When the bias duration time is reduced, ≈200 ns FWHM and ≈100 ns at peak voltage, the selectivity increases to over 35 eV. A similar effect is seen in Xe/H_2 only with generally much larger selectivities due to the much larger mass difference between H^+ and Xe^+.

In practical etching applications, such as the etching of SiO_2 on Si, the difference in the threshold energies for ion enhanced etching is on the order of approximately 10 eV. Thus, a target selectivity for this work should be >10 eV. The definition of selectivity used in this work does not take into account the spread in energy of the peaks and as such there might be significant overlap in the peaks, even when the selectivity is significant (>10 eV). The effect of charge exchange collisions in the sheath could also have a great influence on IED selectivity. Even for bias on times longer than the sheath transit time of a pair of ions, if one ion undergoes collisions and the other does not, the ion that underwent a collision would not strike the substrate with the full bias potential while the other ion would. This would increase the selectivity between the ions.

5.6 Figures

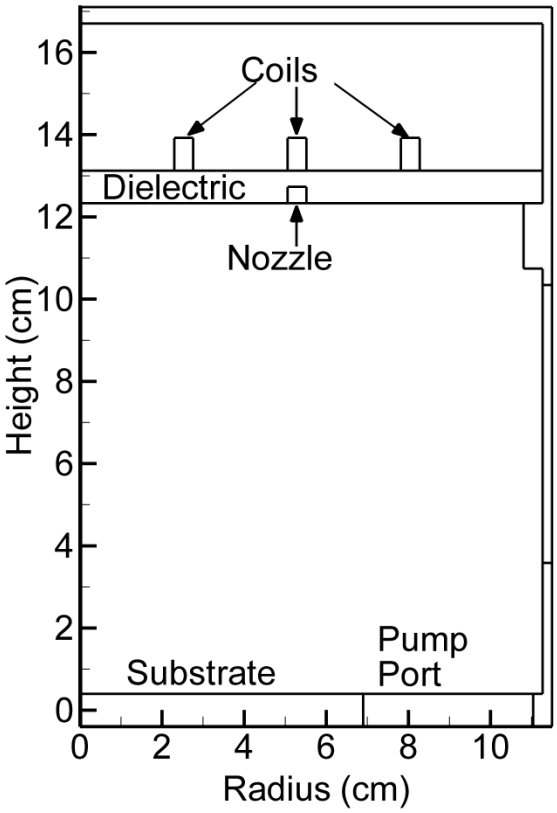

Figure 5.1 Schematic of model Inductively Coupled Plasma (ICP) reactor.

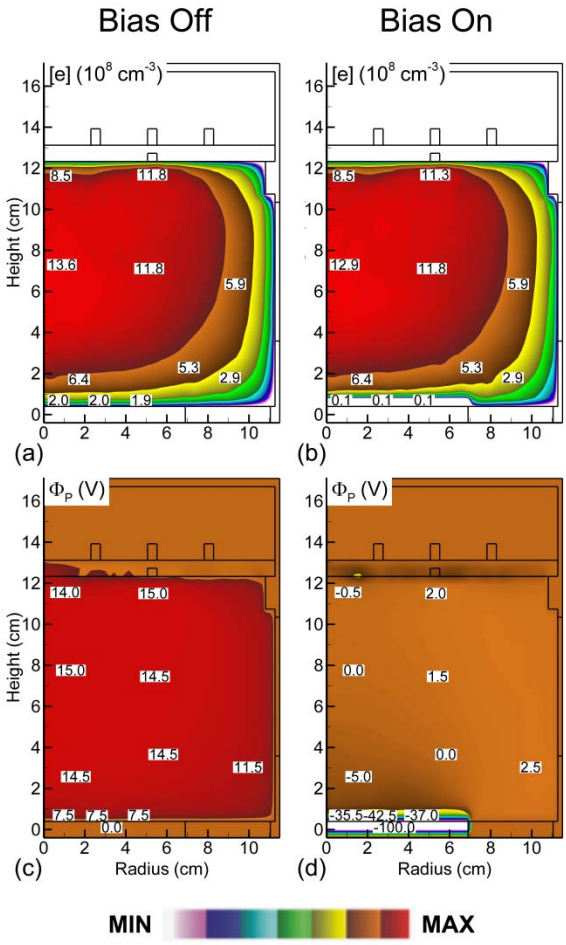

Figure 5.2 Plasma parameters taken directly before a dc bias pulse is applied to the substrate and at the end of a dc bias pulse. The plasma conditions are Ar/H_2 (75/25), 30 W (cw) power, 10 mTorr, 100 sccm. The pulsed dc bias conditions are pulse repetition frequency = 500 kHz and 20% duty cycle. (a) Electron density before pulse. (b) Electron density at end of pulse. (c) Plasma potential before pulse. (d) Plasma potential at end of pulse.

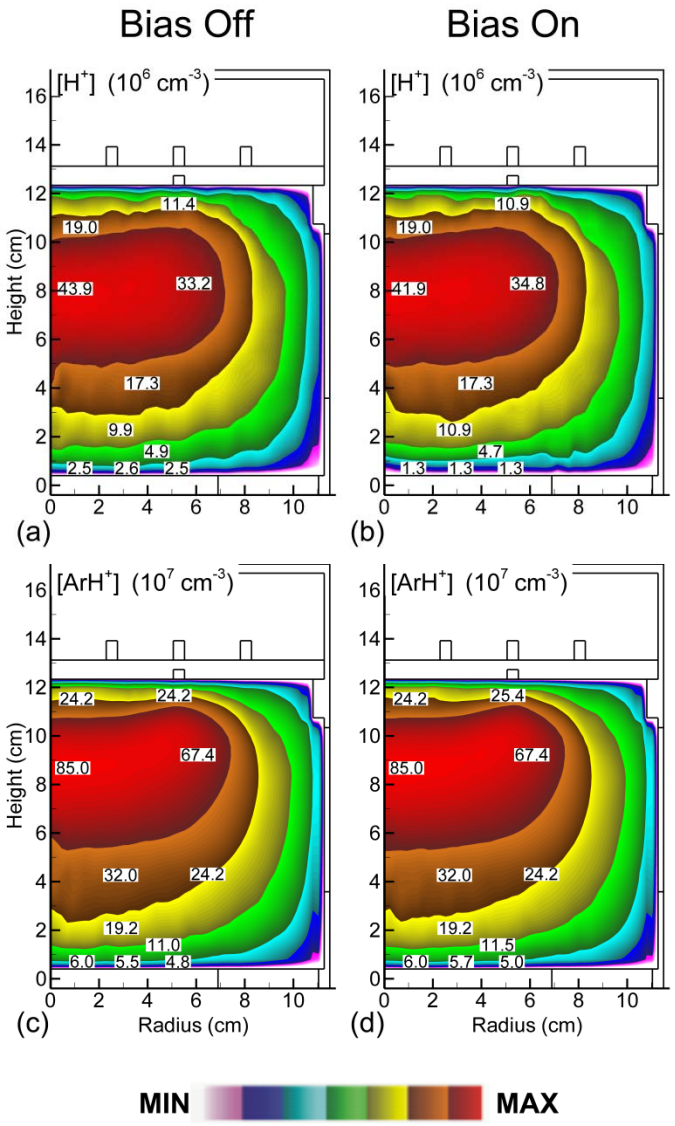

Figure 5.3 Density of H^+ and ArH^+ taken directly before a dc bias pulse is applied to the substrate and at the end of the dc bias pulse. The plasma conditions are Ar/H_2 (75/25), 30 W (cw) power, 10 mTorr, 100 sccm. The pulsed dc bias conditions are pulse repetition frequency = 500 kHz and 20% duty cycle. (a) H^+ density before pulse. (b) H^+ density at end of pulse. (c) ArH^+ density before pulse. (d) ArH^+ density at end of pulse.

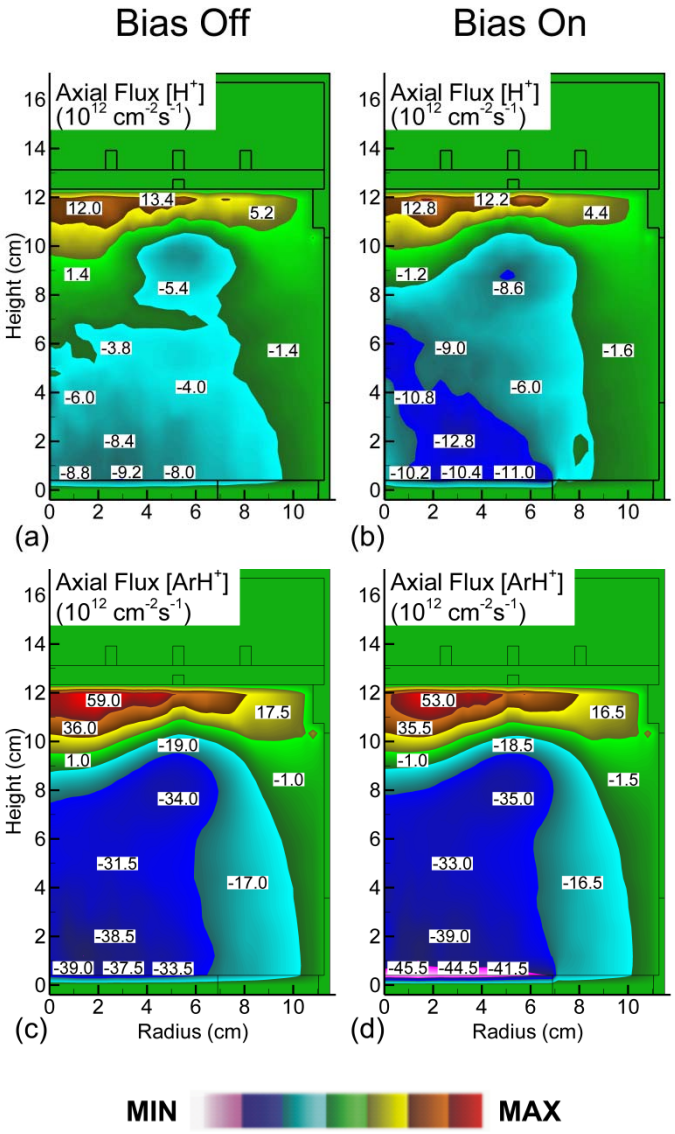

Figure 5.4 Axial flux of H^+ and ArH^+ taken directly before a dc bias pulse is applied to the substrate and at the end of the dc bias pulse. The plasma conditions are Ar/H_2 (75/25), 30 W (cw) power, 10 mTorr, 100 sccm. The pulsed dc bias conditions are pulse repetition frequency = 500 kHz and 20% duty cycle. (a) Axial flux of H^+ before pulse. (b) Axial flux of H^+ at end of pulse. (c) Axial flux of ArH^+ before pulse. (d) Axial flux of ArH^+ at end of pulse.

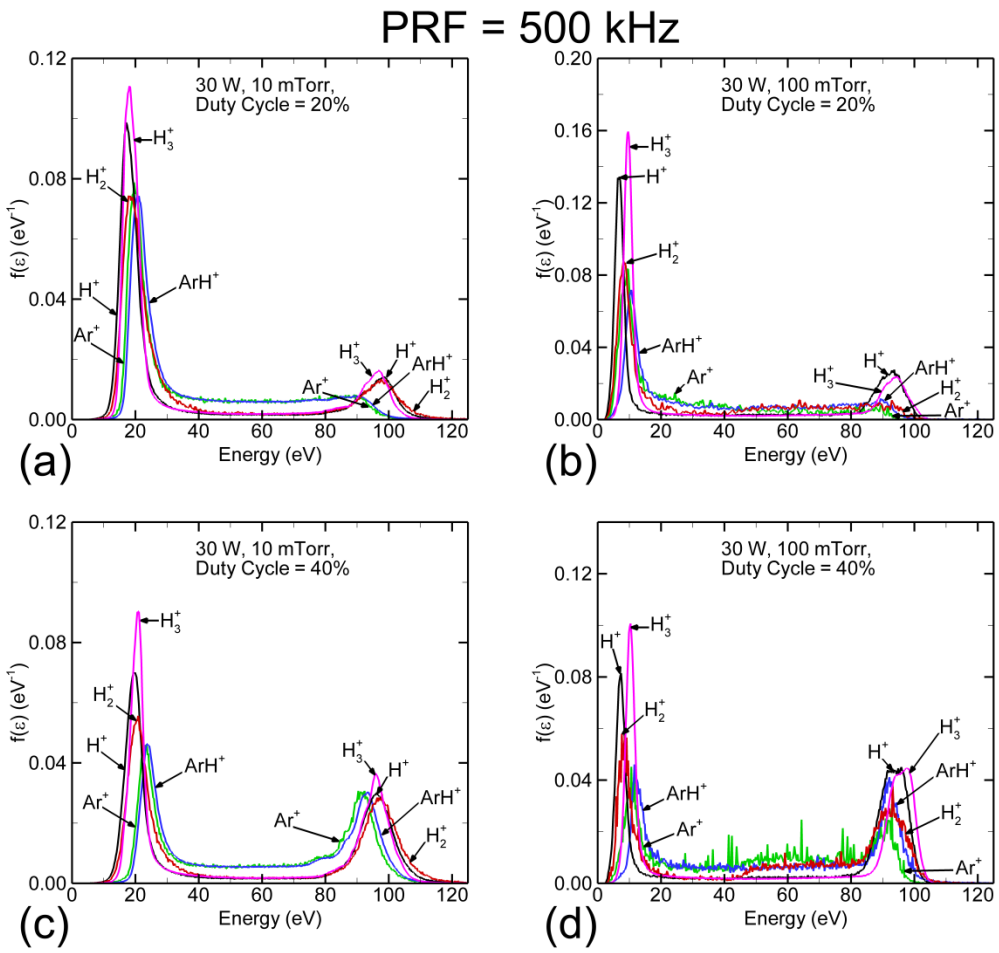

Figure 5.5 Ion energy distributions on the substrate for two pressures and two bias duty cycles. The plasma conditions are Ar/H_2 (75/25), 30 W (cw) power and 100 sccm. The pulsed dc bias conditions are pulse repetition frequency = 500 kHz. (a) Pressure = 10 mTorr, Duty Cycle = 20%. (b) Pressure = 100 mTorr, Duty Cycle = 20%. (c) Pressure = 10 mTorr, Duty Cycle = 40%. (d) Pressure = 100 mTorr, Duty Cycle = 40%.

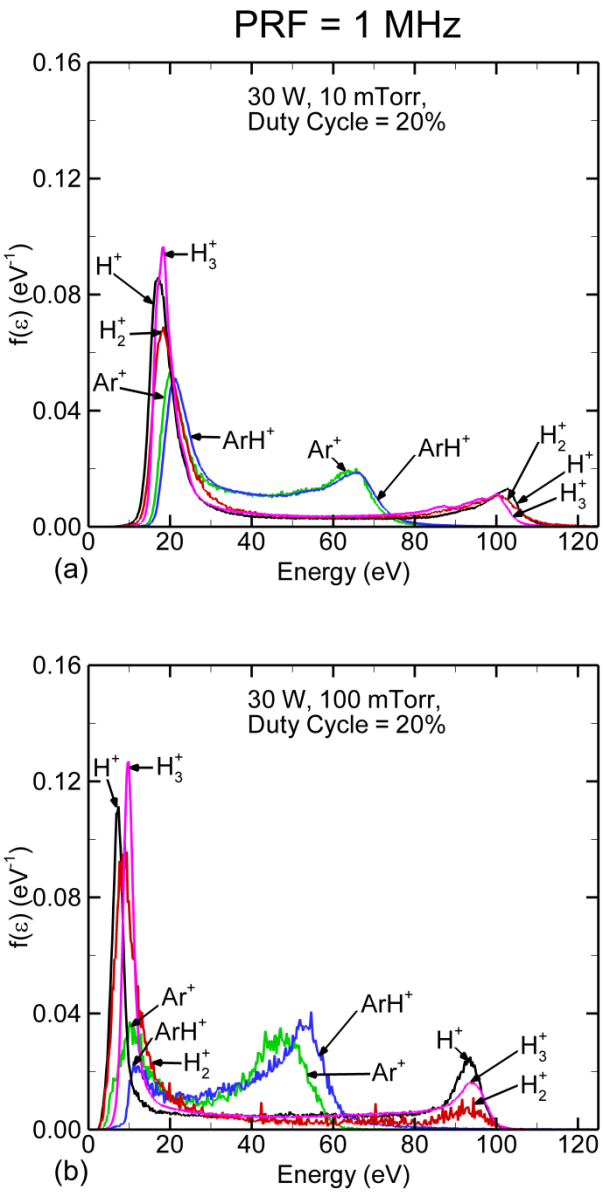

Figure 5.6 Ion energy distributions on the substrate for two pressures. The plasma conditions are Ar/H_2 (75/25), 30 W (cw) power and 100 sccm. The pulsed dc bias conditions are pulse repetition frequency = 1 MHz and 20% duty cycle. (a) Pressure = 10 mTorr. (b) Pressure = 100 mTorr.

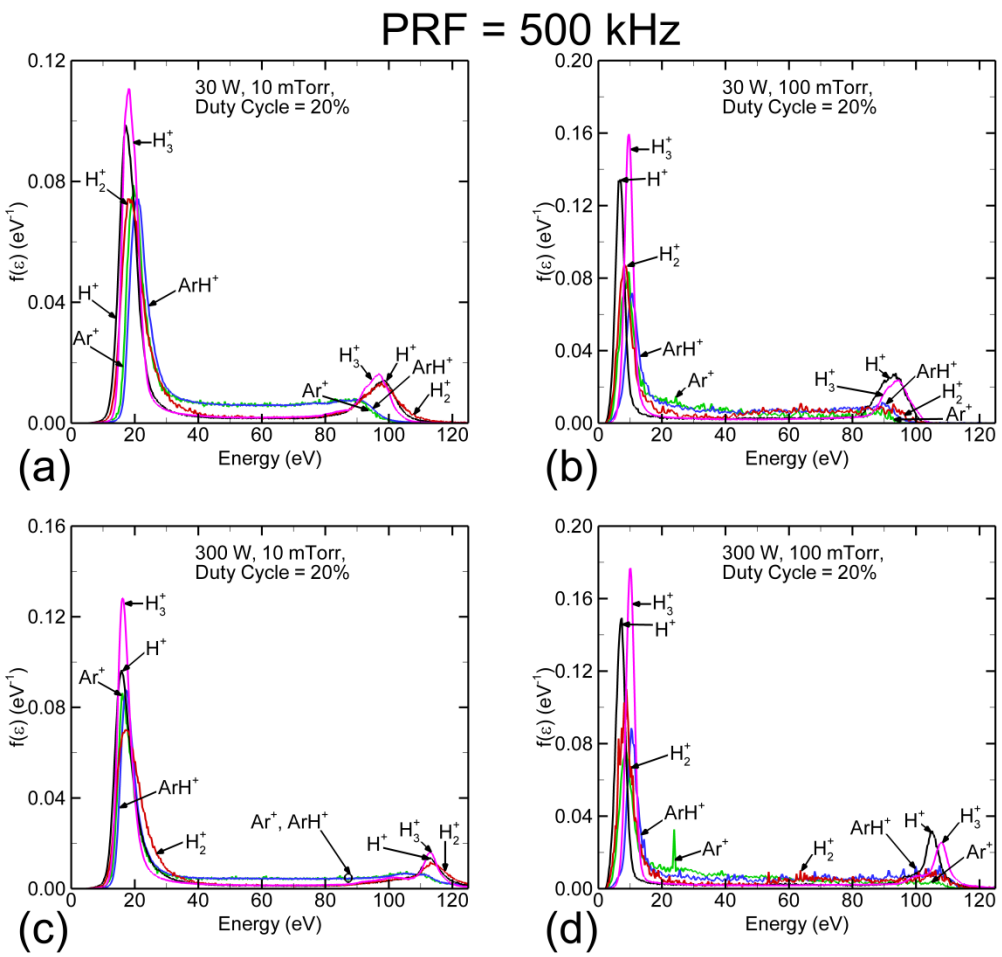

Figure 5.7 Ion energy distributions on the substrate for two pressures and two ICP powers. The plasma conditions are Ar/H_2 (75/25) at 100 sccm. The pulsed dc bias conditions are pulse repetition frequency = 500 kHz and duty cycle = 20%. (a) Pressure = 10 mTorr, Power = 30 W. (b) Pressure = 100 mTorr, Power = 30 W. (c) Pressure = 10 mTorr, Power = 300 W. (d) Pressure = 100 mTorr, Power = 300 W.

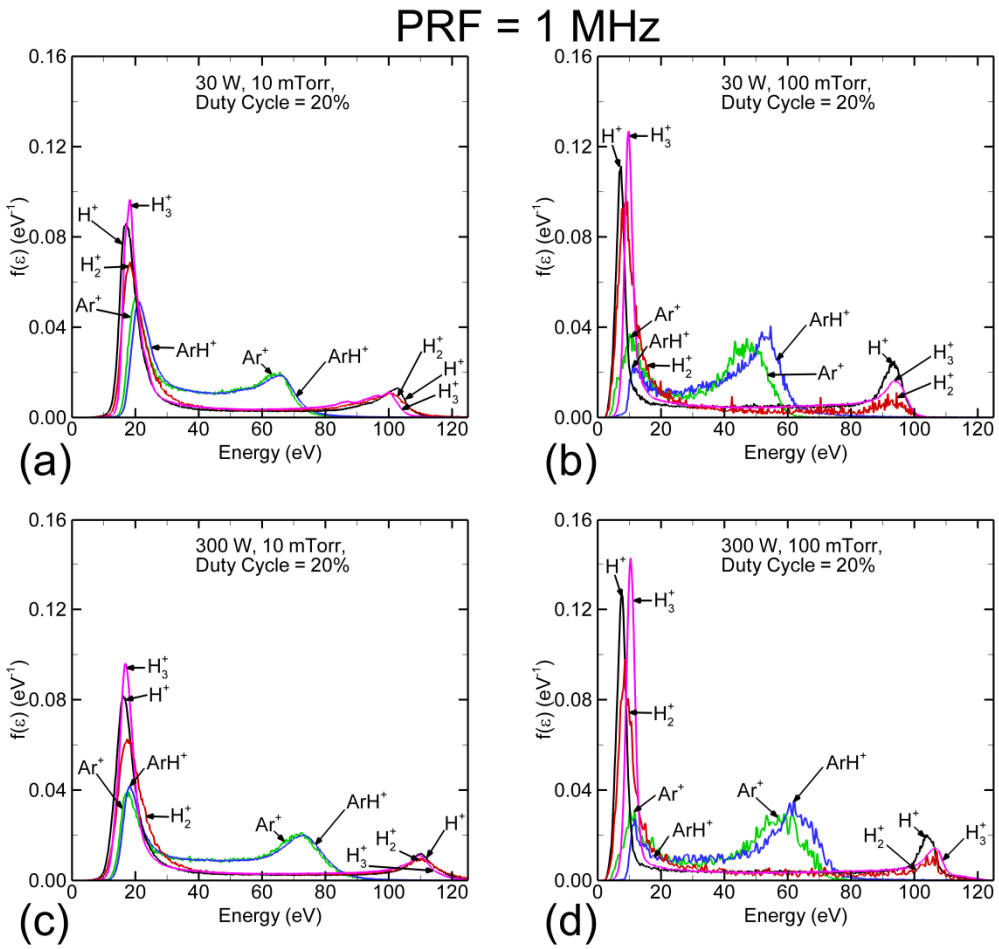

Figure 5.8 Ion energy distributions on the substrate for two pressures and two ICP powers. The plasma conditions are Ar/H_2 (75/25) at 100 sccm. The pulsed dc bias conditions are pulse repetition frequency = 1 MHz and duty cycle = 20%. (a) Pressure = 10 mTorr, Power = 30 W. (b) Pressure = 100 mTorr, Power = 30 W. (c) Pressure = 10 mTorr, Power = 300 W. (d) Pressure = 100 mTorr, Power = 300 W.

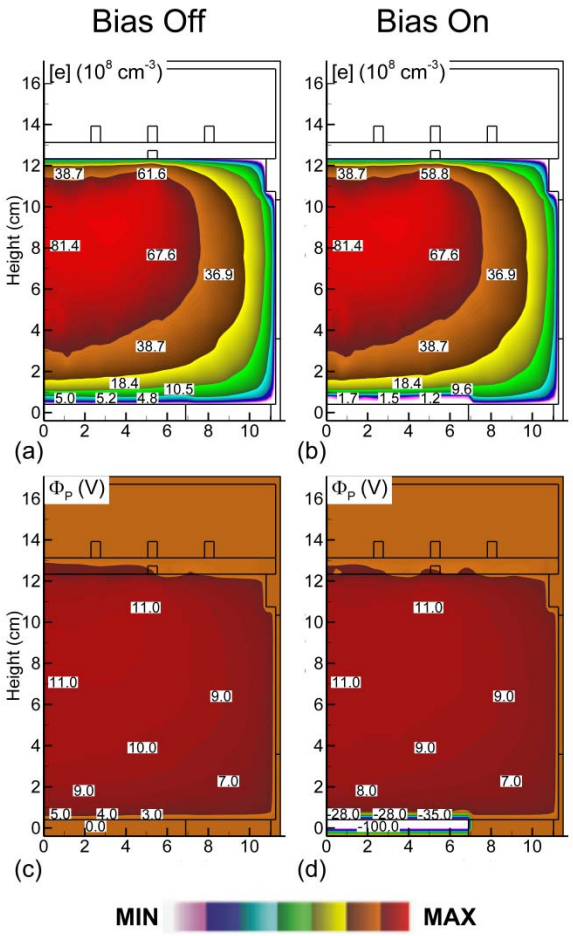

Figure 5.9 Plasma parameters taken directly before a dc bias pulse is applied to the substrate and at the end of a dc bias pulse. The plasma conditions are Xe/H_2 (75/25), 30 W (cw) power, 10 mTorr, 100 sccm. The pulsed dc bias conditions are pulse repetition frequency = 500 kHz and 20% duty cycle. (a) Electron density before pulse. (b) Electron density at end of pulse. (c) Plasma potential before pulse. (d) Plasma potential at end of pulse.

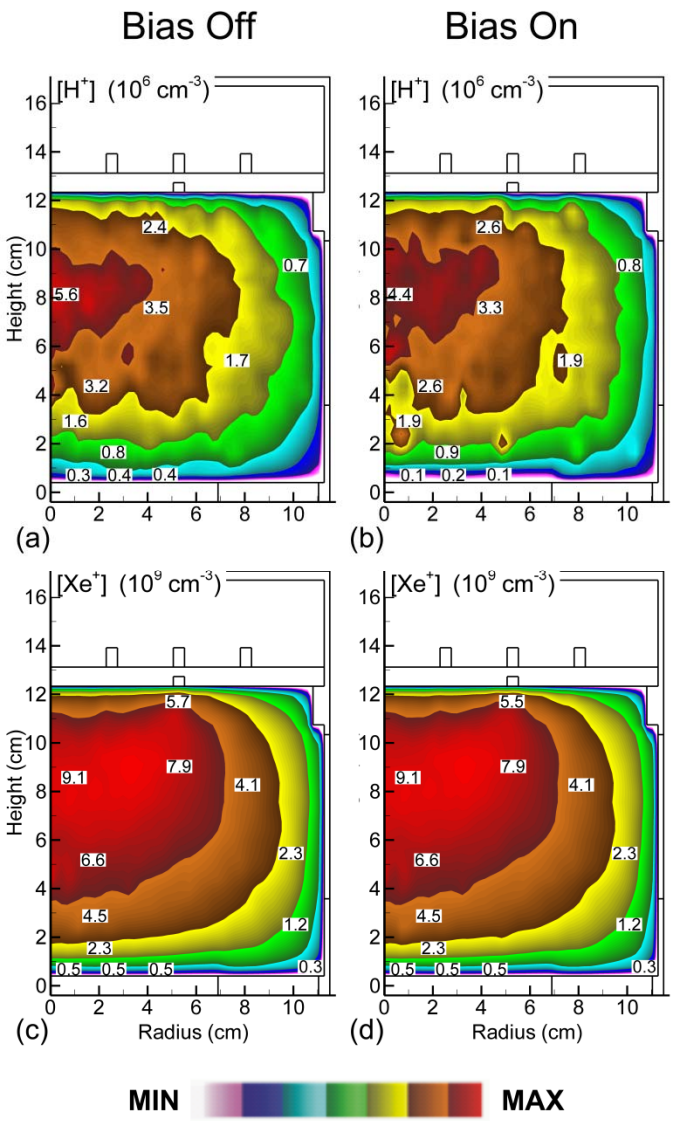

Figure 5.10 Density of H^+ and Xe^+ taken directly before a dc bias pulse is applied to the substrate and at the end of the dc bias pulse. The plasma conditions are Ar/H_2 (75/25), 30 W (cw) power, 10 mTorr, 100 sccm. The pulsed dc bias conditions are pulse repetition frequency = 500 kHz and 20% duty cycle. (a) H^+ density before pulse. (b) H^+ density at end of pulse. (c) Xe^+ density before pulse. (d) Xe^+ density at end of pulse.

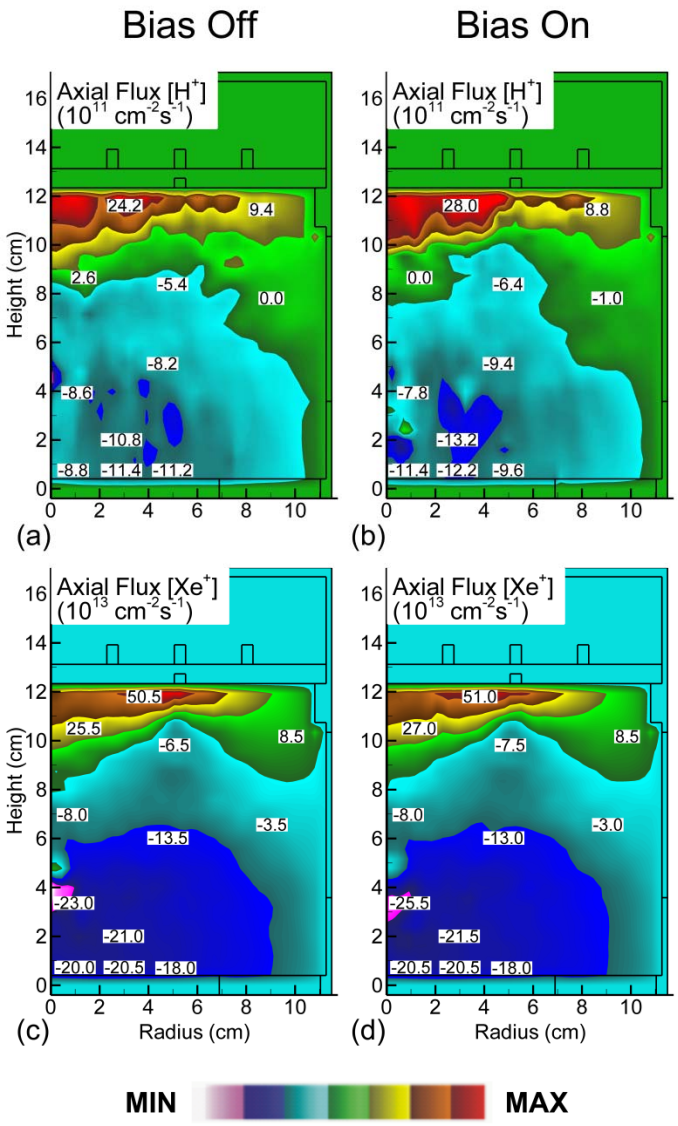

Figure 5.11 Axial flux of H^+ and Xe^+ taken directly before a dc bias pulse is applied to the substrate and at the end of the dc bias pulse. The plasma conditions are Ar/H_2 (75/25), 30 W (cw) power, 10 mTorr, 100 sccm. The pulsed dc bias conditions are pulse repetition frequency = 500 kHz and 20% duty cycle. (a) Axial flux of H^+ before pulse. (b) Axial flux of H^+ at end of pulse. (c) Axial flux of Xe^+ before pulse. (d) Axial flux of Xe^+ at end of pulse.

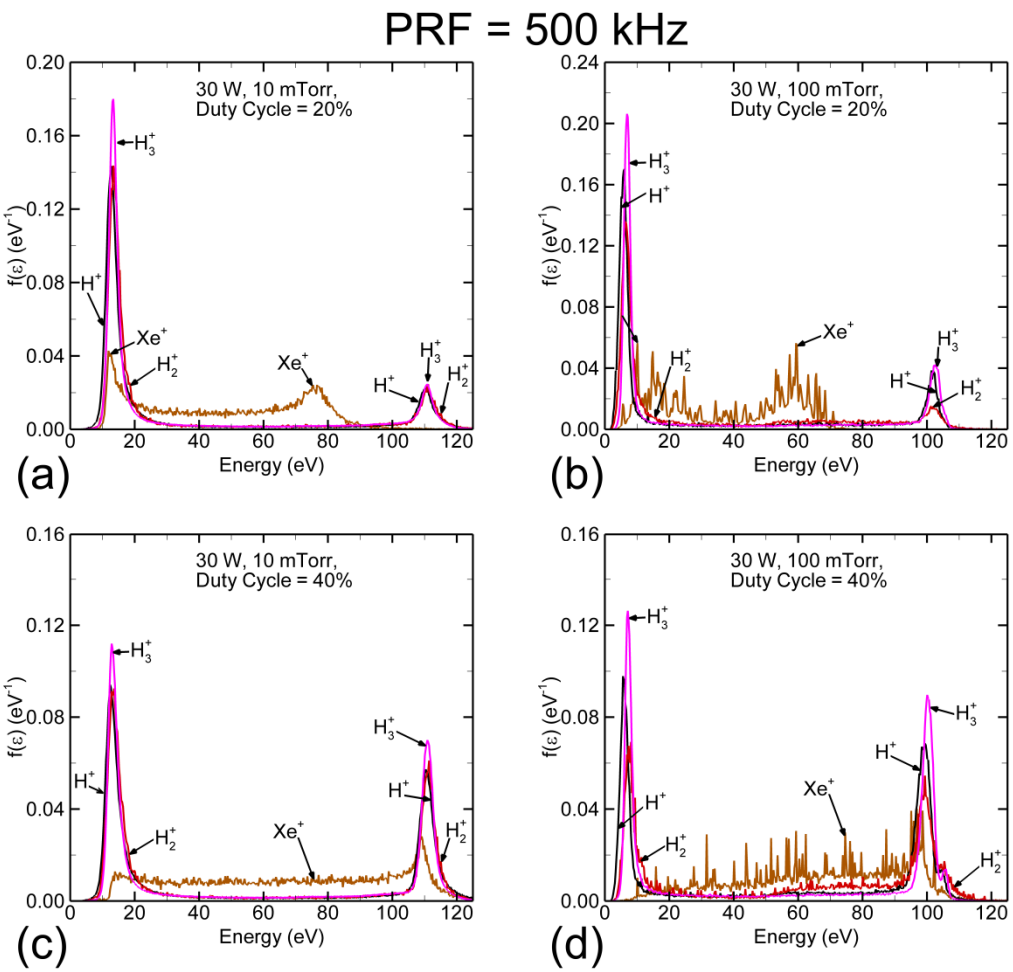

Figure 5.12 Ion energy distributions on the substrate for two pressures and two bias duty cycles. The plasma conditions are Xe/H_2 (75/25), 30 W (cw) power and 100 sccm. The pulsed dc bias conditions are pulse repetition frequency = 500 kHz. (a) Pressure = 10 mTorr, Duty Cycle = 20%. (b) Pressure = 100 mTorr, Duty Cycle = 20%. (c) Pressure = 10 mTorr, Duty Cycle = 40%. (d) Pressure = 100 mTorr, Duty Cycle = 40%.

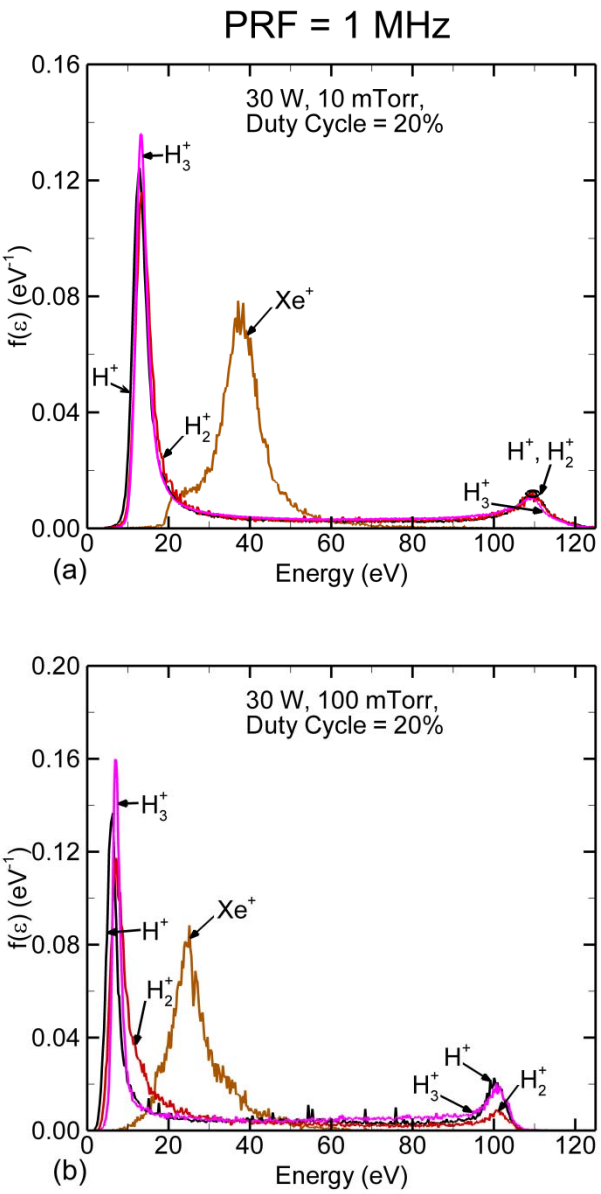

Figure 5.13 Ion energy distributions on the substrate for two pressures. The plasma conditions are Xe/H_2 (75/25), 30 W (cw) power and 100 sccm. The pulsed dc bias conditions are pulse repetition frequency = 1 MHz and 20% duty cycle. (a) Pressure = 10 mTorr. (b) Pressure = 100 mTorr.

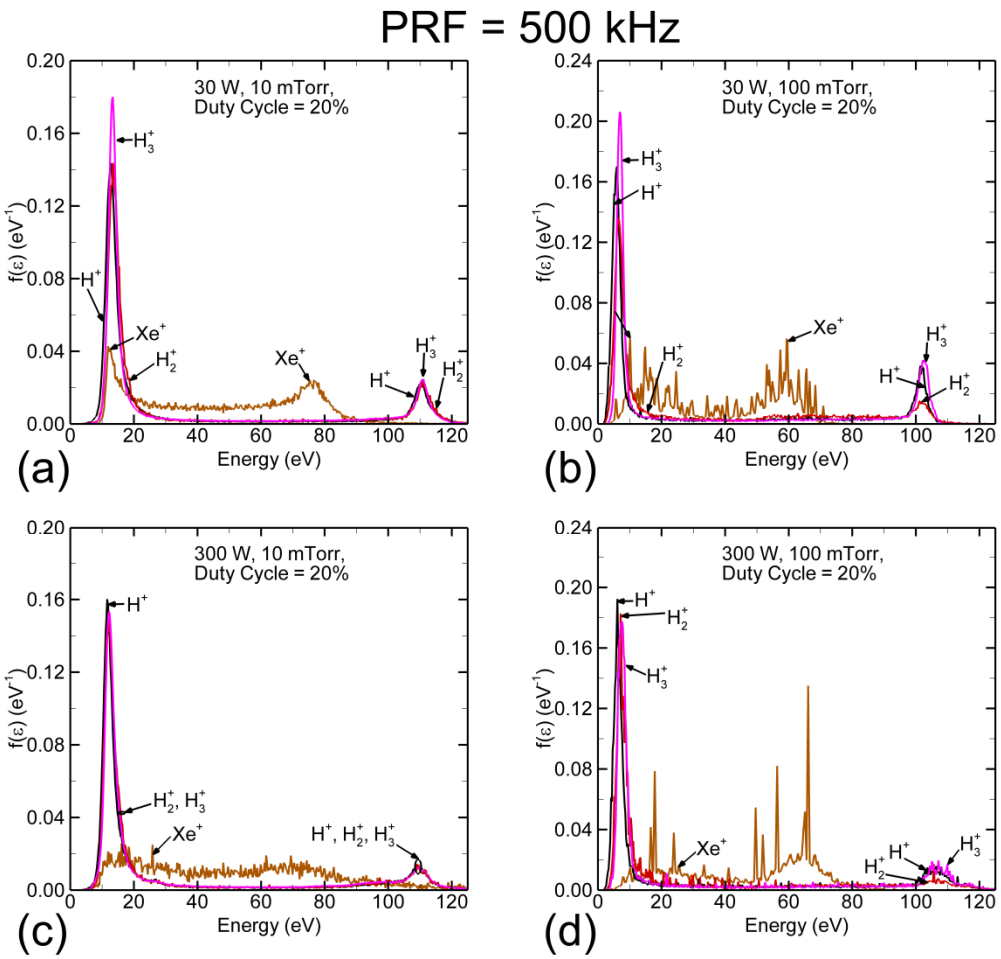

Figure 5.14 Ion energy distributions on the substrate for two pressures and two ICP powers. The plasma conditions are Xe/H_2 (75/25) at 100 sccm. The pulsed dc bias conditions are pulse repetition frequency = 500 kHz and duty cycle = 20%. (a) Pressure = 10 mTorr, Power = 30 W. (b) Pressure = 100 mTorr, Power = 30 W. (c) Pressure = 10 mTorr, Power = 300 W. (d) Pressure = 100 mTorr, Power = 300 W.

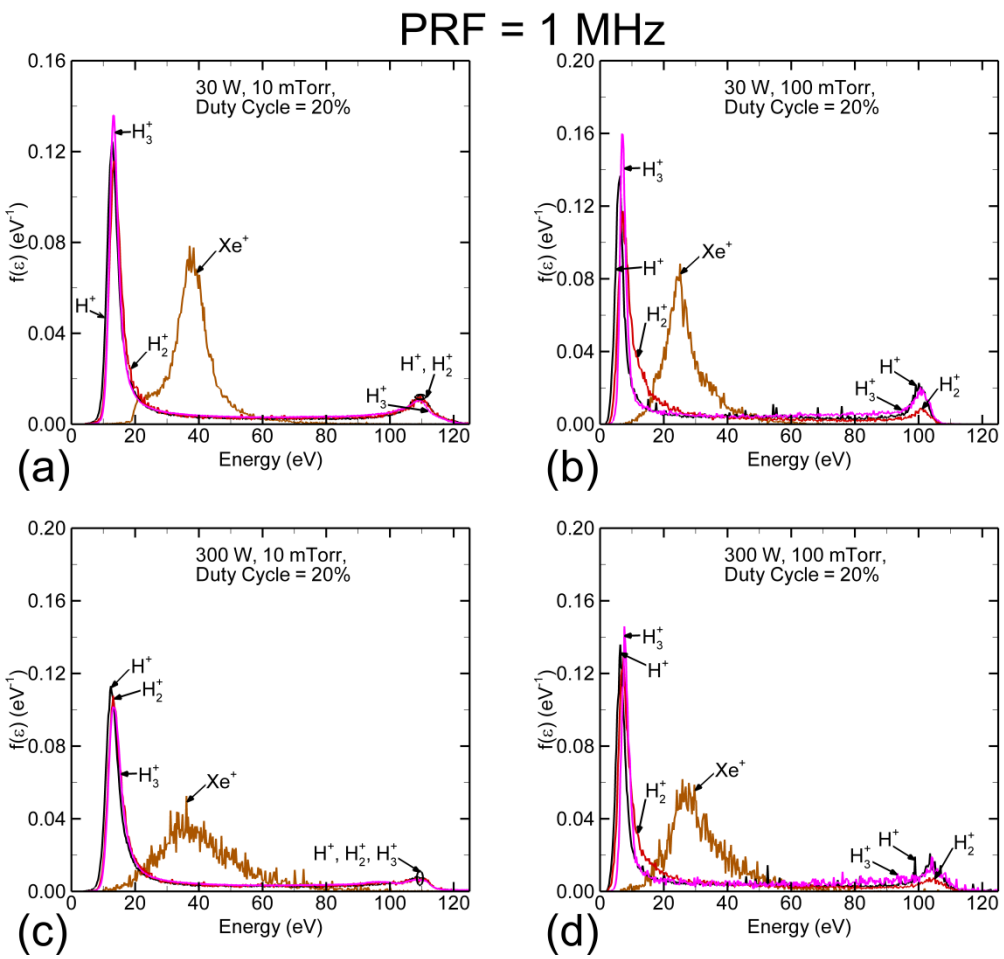

Figure 5.15 Ion energy distributions on the substrate for two pressures and two ICP powers. The plasma conditions are Xe/H_2 (75/25) at 100 sccm. The pulsed dc bias conditions are pulse repetition frequency = 1 MHz and duty cycle = 20%. (a) Pressure = 10 mTorr, Power = 30 W. (b) Pressure = 100 mTorr, Power = 30 W. (c) Pressure = 10 mTorr, Power = 300 W. (d) Pressure = 100 mTorr, Power = 300 W.

5.7 References

1. J. P. Chang, J. C. Arnold, G. C. H. Zau, H.-S. Shin, and H. H. Sawin, J. Vac. Sci. Technol. A **15**, 1853 (1997).

2. L. Xu, D. J. Economou, V. M. Donnelly, P. Ruchhoeft, Appl. Phys. Lett. **87**, 041502 (2005).

3. P. Diomede, D. J. Economou, and V. M. Donnelly, J. Appl. Phys. **109**, 083302 (2011).

4. H. Shin, W. Zhu, L. Xu, V. M. Donnelly, and D. J. Economou, Plasma Sources Sci. Technol. **20**, 055001 (2011).

5. M. D. Logue, H. Shin, W. Zhu, L. Xu, V. M. Donnelly, D. J. Economou, and M. J. Kushner, Plasma Sources Sci. Technol. **21**, 065009 (2012).

6. A. Manenschijn, G. C. A. M. Janssen, E. van der Drift, and S. Radelaar, J. Appl. Phys. **69**, 1253 (1991).

7. J. T. Gudmundsson, Plasma Sources Sci. Technol. **8**, 58 (1999).

8. S. B. Radovanov, J. K. Olthoff, R. J. Van Brunt, and S. Djurovi, J. Appl. Phys. **78**, 746 (1995).

Chapter 6 Control of Electron Energy Distributions in Inductively Coupled Plasmas Using Tandem Sources

6.1 Introduction

Low temperature, low gas pressure plasmas are used for a variety of applications such as gas discharge lighting and plasma materials processing.[1] In these plasmas, many chemical reaction processes are initiated by electrons whose energy determines the rate at which these processes occur.[1] These processes generate reactive species (radicals, ions, photons) in the plasma and the balance between the rate coefficients of the reactions, and thus the generation rates of the different reactive species, can be controlled through control of the electron energy distribution (EED).[2] In the semiconductor manufacturing industry, one area of plasma materials processing where control of the flux of reactive species to surfaces is of major importance is in the area of plasma etching. The ability to meet future demands to reduce feature sizes on semiconductor wafers requires tight control of plasma properties.[3] These plasma properties include electron temperature (T_e), dissociation rate, and plasma density, among other properties.[3] Better control of these parameters can be achieved through better control of the EED.

Control of plasma properties and EEDs in plasma processing systems has been investigated for a variety of methods. These methods include pressure[4-7], pulsing[8-10], remote sources[11, 12], and tandem sources[13-15]. The use of remote and tandem sources is especially intriguing, as this may allow for ways to control the EED dynamically beyond what could be achieved with pulsed operation.

Kato *et al*. investigated the effect of applying a bias on a mesh grid used to separate two experimental regions, a source and diffusion region, on plasma parameters in the regions.[11] Applying a negative bias on the grid reduced T_e and increased the electron density (n_e) in the diffusion region far from the grid. The negative bias only allows high energy electrons through the grid, which undergo ionizing collisions, increasing n_e. The electrons produced far in the diffusion region do not have to maintain the discharge in region 1, so they do not have to be accelerated and T_e remains low. The bias voltage at which T_e in the diffusion region starts to decrease is a function of the grid spacing.

Hong *et al*. also investigated the effect of applying a bias on a grid used to separate a source region and a diffusion region, on plasma parameters and EEDs.[12] The source used is an inductively coupled plasma (ICP) source and the background gas is argon. Plasma parameters and EEDs in the source region were not affected by bias, except for plasma potential (Φ_P), which was increased when positive bias was applied. In the diffusion region, n_e and the plasma potential (Φ_P) generally decreased as the bias became more negative. Applying a negative bias past a threshold value reduced T_e in the diffusion region. The threshold value was found to depend on the grid spacing, the same as in the work of Kato *et al.* [11]. In particular, the area ratio of the sheath free region in between the wires of the grid and the total area in between wires of the grid, was found to be an indicator of how much T_e was cooled. The measured EEDs reflect the lowering of T_e as the grid bias becomes more and more negative. The EEDs become narrower with a larger peak at low energy.

Haas *et al*. investigated the effect of the injection of an electron beam into an argon capacitively coupled plasma (CCP) on plasma parameters and EEDs.[13] The authors developed a computational model of a CCP system and compared their results to experimental data

obtained by a Langmuir probe. They found that the introduction of a high energy electron beam modified the rate coefficients for excitation and ionization and the collisional energy loss per electron-ion pair created, such that the rate of ionization was much larger than that of excitation. This resulted in an increase in electron density, which in turn lowered the electron temperature and modified the EED. The increase in electron density was primarily through the increase in density of low energy electrons. The increased number of low energy electrons lowers the average electron energy in the EED, and thus lowers the electron temperature. The EED without the electron beam injection was essentially Maxwellian, with a temperature slightly above 2 eV. With the injection, the EED remained Maxwellian but with a temperature of less than 1 eV. Haas and Braithwaite theoretically investigated the effect of the injection of high energy electrons into the tail of the EED on plasma properties in an Ar ICP.[14] They found, as was the case in the CCP reactor, that injection of high energy electrons modified the rate coefficients for excitation, ionization, and collisional energy loss per electron-ion pair created, which increased electron density and reduced electron temperature.

Uhm *et al*. investigated plasma parameters and EEDs in a dual ICP system where the ICPs are connected in parallel and a series variable capacitor is connected to the main ICP.[15] They found that there was a dip in plasma potential midway between the two sources, which acted as a potential hill to electrons. This caused the low energy portions of the EEDs in the two regions to be different, as the low energy electrons did not have enough energy to overcome the potential hill and travel between the sources. The high energy portions of the EEDs in the two regions were almost the same.

In this chapter, a computational investigation of plasma parameters [T_e, Φ_P, n_e, and electron source function (S_e)] and EEDs in the lower, primary ICP region of a tandem-ICP (T-

ICP) system is presented. The two ICP regions are separated by a biasable grid. The test system models the reactor and experimental data from the research groups of Professor Vincent Donnelly and Professor Demetre Economou at the University of Houston. It is observed that the upper secondary ICP has little effect on the plasma properties and EEDs in the lower ICP region when both ICPs are operated in continuous wave (cw) mode. When the lower ICP is pulsed with the upper ICP on in cw mode, the upper ICP is able to affect T_e and the EED in the plasma afterglow of the lower ICP. The tail of the EED is lifted in the afterglow from the influx of high energy electrons from the upper ICP, which also causes T_e to increase in the afterglow of the plasma. Applying a large positive bias to a boundary electrode on the top of the system, while the upper ICP is on in cw mode and the lower ICP is pulsed, creates a local ionization region at the gas inlet, which is in the boundary electrode. This local ionization region acts as another source of flux of high energy electrons from the upper ICP region and enhances the effects seen without a bias applied to the boundary electrode.

All results are for plasmas sustained in argon. The species consist of Ar (ground state), Ar*, Ar**, Ar***, Ar^+ and electrons. Ar* represents the combined metastable states of the $Ar(3p^54s)$ manifold [$Ar(1s_5)$, $Ar(1s_3)$] and Ar** represents the combined radiative states [$Ar(1s_4)$, $Ar(1s_2)$]. Ar*** is a lumped state representing $Ar(3p^54p)$ and higher states in the excited state manifold. Radiation trapping of the Ar** state is included.

6.2 Description of the Reactor and Experiment

A schematic of the tandem ICP system used in the computational investigation is shown in Fig. 6.1, which is the representation of the experimental device shown in Fig. 6.2. The lower, primary plasma is sustained in an 8 cm diameter dielectric tube with a 3-turn spiral coil powered at 10 MHz. (The experiments were done at 13.56 MHz.) The upper, secondary plasma is

sustained in a 9 cm diameter dielectric tube with a 12-turn spiral coil powered at 10 MHz. (The experiments were done with an 11.5 turn coil at 13.56 MHz.) A Faraday shield is employed in the experiment for both ICPs to reduce capacitive coupling and insure operation in the H-mode. In the model, a Faraday shield is also employed for both ICPs to suppress capacitive coupling from the coils. There is a boundary electrode at the top of the chamber, which is the metal lid of the chamber, as well as a biasable mesh grid separating the two ICP regions. The grid is always grounded.

In the model, gas is injected on axis from a cylindrical inlet at the top and pumped away at the bottom. In the experiment, gas is injected through a cylindrical inlet that passes through the top of the boundary electrode but opens into the chamber through the inner side of the electrode. Kapton tape is used over most of the inner surface of the boundary electrode in the experiment as it was discovered that higher biases could not be achieved without this. A dielectric layer covering most of the boundary electrode, representing the kapton tape, is included in the model.

There is also a grounded donut shaped stage in the lower plasma region, which can be used for etching experiments. The stage has a two inch outer diameter and a one inch inner diameter. Electron energy probability functions (EEPFs) are measured experimentally using a Langmuir probe that can be moved in the axial direction along the center axis of the chamber at a radius of 0 cm. Model computed EEDs, referred to as $f_e(\varepsilon)$, are sometimes converted into EEPFs, typically when comparing against experimental data, by multiplying $f_e(\varepsilon)$ by the electron density (n_e). Results for plasma parameters are also discussed.

6.3 Control of EEPFs and Plasma Parameters with a Tandem Source

6.3.1 EEDs and plasma parameters with cw excitation

n_e, T_e, and S_e, at 500 W upper ICP power and 90 W lower ICP power, 10 mTorr of pressure, no bias applied to the boundary electrode (V_B = 0 V) , a grounded grid, and a grounded stage are shown in Fig. 6.3. When the ICPs are operated under cw conditions, the characteristics of the two ICPs are determined by the power from their respective coils. S_e shows that the dominant ionization regions are well separated; however the high thermal conductivity of the plasmas spread T_e between the source regions. There is some mixing between the two ICPs through the grid, as evidenced by the electron density profile.

In an ICP, power is coupled into the plasma through induced electric fields within a skin depth layer near the boundary of the plasma.[16] In the tandem-ICP system, the skin depth of the electromagnetic field is near the coils in the radial dimension and within the upper and lower bounds of the coil in the axial dimension. The deposited power falls off exponentially outside these bounds. The skin depth in the lower ICP is ≈2 cm and the skin depth in the upper ICP is ≈0.8 cm. With an exponential decay in power with distance and a height separation between the bottom of the upper ICP and the top of the lower ICP of ≈12 cm, almost no power deposited by one ICP makes it to the other ICP region except through an exchange of energetic electrons. These electrons gain energy in the skin depth and then transfer that energy through the plasma by collisions. The power density deposited by the lower ICP within its region at a radius of 0.6 cm, at the height of the top edge of the lower coils, height = 16.8 cm, is $\approx 5.4 \times 10^7$ times greater than the power density deposited by the upper ICP. The power density deposited by the lower ICP in the upper region at a radius of 0.6 cm, at the height of the bottom edge of the upper coils, height = 30.5 cm, is $\approx 4.9 \times 10^8$ times less than the power density deposited by the upper ICP.

Computed and experimental electron energy probability functions (EEPFs) in the lower ICP region at two heights are shown in Fig. 6.4. The EEPFs are computed for three operating conditions: lower plasma on only at 90 W, upper plasma on only at 500 W, and both plasmas on at the same powers as when operated alone. The EEPFs are taken near the center of the reactor in the lower ICP region at an equivalent position between the model and experiment. The axial position is height = 10.8 cm in the model and height = 210 mm in the experiment. The radial position is radius = 0.6 cm in the model and radius = 0 cm in the experiment.

The radial position at which the EEPFs are taken are different in the model and experiment, due to the fact that radius = 0 cm represents the edge of the computational mesh where statistics are less accurate. The EEPFs in the model are calculated from an average of the EEPFs in the specified mesh cell as well as the EEPFs from a specified number of adjacent mesh cells. At radius = 0 cm, there are no mesh cells on one side of the mesh cell that contains the specified point. This increases statistical noise. The axial position is different as in the experiment there is a third chamber below the lower ICP region that basically acts as a gas diffusion region where height = 0 cm is defined. The turbo pump is connected to this region. In the model, this third chamber region is not included and the pump is connected at the position where the third chamber starts in the experiment.

When the lower ICP is on, the EEPFs are essentially the same whether or not the upper source is on. This reflects the observed behavior of Fig. 6.3 in that the plasma properties in the two ICP regions are predominantly a function of the local power deposition. This is especially true for the position at which these EEPFs are being taken, as this location is very far from the upper ICP source. This can also be observed by looking at the EEPF when only the upper ICP is on, it is ≈2-3 orders of magnitude lower at all energies, than EEPFs when the lower plasma is on.

The computed EEPFs when the lower ICP is on appear to have a three temperature distribution. This is not seen experimentally at the equivalent height of 10.8 cm, but is seen at the equivalent height of 14.8 cm. The reasons for this discrepancy are unknown at this time. There is also a roll-off in the EEPF at very low energies, which is not seen in the model. This may be due to low collection efficiency of the Langmuir probe at very low energies. A three temperature distribution in Ar ICPs at 10 mTorr has been observed before by Godyak et al. [17]. The low energy portion of the distribution is a result of low energy electrons in the center of the plasma being trapped by the ambipolar potential and being prevented from reaching the skin depth where most electron heating occurs. It is the electrons in the middle temperature regime that are able to make it to the skin depth, where they can be heated by the ICP power, leading to a larger temperature. Above the threshold energy for the start of inelastic collisions electrons lose energy to inelastic collisions, which leads to a lower temperature and a lowering of the tail of the EEPF.

This can be seen for example in the case when both ICPs are on at a height of 10.8 cm, Fig. 6.4a. The ranges in energy that correspond to the three temperature regimes are approximately: ε = 0-4.0 eV, ε = 4.0-12.0 eV, and ε > 12.0 eV. The temperatures in these regimes are ≈2.3 eV, ≈3.9 eV, and ≈2.2 eV, respectively. Similar behavior is observed at a height of 14.8 cm. The temperature range above ε = 12 eV corresponds to energy range above the first inelastic collision threshold of Ar, which is electronic excitation with a threshold energy of 11.6 eV. The start of inelastic collisional processes causes the tail of the EEPF to lower as higher energy electrons are depleted from the system.

The computed EEPF when just the upper plasma is on appears to be three temperature at a height of 10.8 cm and two temperature at a height of 14.8 cm. The reasons for this remain

unclear, although the densities in the lower ICP are very low with just the upper ICP on, which could result in some noise in the computed EEPFs. The experimentally measured EEPF at the equivalent height of 10.8 cm appears flat across the entire energy range, but this is believed to be an erroneous measurement. The shape and magnitude of the experimentally measured EEPF, when just the upper ICP is on, at the equivalent height of 14.8 cm, has a closer agreement between the model and experiment. There is a large roll-off in the experimental EEPF at low energies, which is unexplained but believed to be a measurement error due to the low electron density. Overall there is good agreement between the model and experiment with respect to the shapes and magnitudes of the EEPFs.

Computed $f_e(\varepsilon)$ in the lower ICP region at two heights for two boundary electrode bias voltages, V_B = 0 V and V_B = 60 V, are shown in Fig. 6.5. The plasma potential profile in the T-ICP for the two V_B is shown in Fig. 6.6. Both ICPs are on, with the upper ICP at 500 W and the lower ICP at 90 W. At a height of 10.8 cm, applying a 60 V boundary electrode voltage lowers the tail of $f_e(\varepsilon)$ above $\varepsilon \approx 3.0$ eV slightly. V_B raises the plasma potential in both the upper and lower ICP regions. The raised plasma potential in the lower ICP traps more electrons near the center of the lower ICP at a height of 13.0 cm, which reduces the number of high energy electrons that reach the height of 10.8 cm. The potential difference between height = 13.0 cm and height = 10.8 cm at a radius of 0.6 cm goes from ≈1.5 V to ≈1.7 V. The density of low energy electrons is unchanged because that is largely dominated by the local power deposition from the coils.

At a height of 18.8 cm, there are believed to be two main factors that contribute to the shape of $f_e(\varepsilon)$ when V_B = 60 V as opposed to when V_B = 0 V. The first factor that contributes to the observed shape of $f_e(\varepsilon)$ when V_B = 60 V, is that when a +60 V bias is applied to the boundary

electrode, which the gas inlet nozzle passes through, a local ionization region develops at the gas inlet. n_e, T_e, and S_e for the case with both ICPs on, with the upper ICP at 500 W and the lower ICP at 90 W, and V_B = 60 V, are shown in Fig. 6.7. The positive bias on the boundary electrode increases electron current flow to the electrode. The smaller effective area of the boundary electrode in contact with the plasma causes the current density to go up, which requires a higher E/N to sustain. The E/N near the gas inlet at a radius of 0.6 cm and a height of 54.5 cm for V_B = 0 V is ≈154 Td and at V_B = 60 V is ≈3,941 Td. This significantly higher E/N increases T_e and produces local ionization at the gas inlet nozzle.

From the profile of T_e in Fig. 6.7 it is seen that T_e near the gas inlet can be several eV higher than in the plasma regions generated from the two ICP sources. Peak T_e from the local ionization region at the gas inlet is ≈5.8 eV while the peak T_e in the plasma produced by the upper ICP coils is ≈3.8 eV. The local ionization region near the gas inlet produces a flux of high energy electrons that goes through the upper ICP region to the lower region. This is in addition to the flux of high energy electrons generated by the upper ICP itself. At V_B = 60 V the tail of the $f_e(\varepsilon)$ is raised as a greater number of hot electrons flow from the upper ICP region to the lower region.

The second factor that contributes to the observed shape of $f_e(\varepsilon)$ when V_B = 60 V, is that the dc bias draws an electron current toward the gas inlet. This increases the flux of electrons toward the inlet from the center of the lower ICP plasma. This increases the density of electrons at a height of 18.8 cm for V_B = 60 V compared to V_B = 0 V. The density increases from ≈6.3 x 10^{10} cm^{-3} to ≈8.1 × 10^{10} cm^{-3}.

Photos of the gas inlet nozzle at the top of the experimental tandem ICP system, when both ICPs are on, with the upper ICP at 500 W and the lower ICP at 90 W, are shown in Fig. 6.8

for two bias voltage, V_B = 0 V and V_B = 80 V. The photos clearly show the development of a local ionization region with the application of a large positive bias on the boundary electrode. There is a threshold bias for this local ionization process to be observed, which is ≈40-45 V in our simulations.

6.3.2 EEPFs and plasmas with pulsed plasmas

An additional means to control EEPFs and plasma parameters is achieved through pulsing of the ICP power with and without applying a dc bias. In a pulsed ICP the electron density diffuses away in the afterglow when the ICP power is off, with higher energy electrons being removed from the system the fastest, through diffusion cooling. Diffusion cooling is the increased loss rate of higher energy electrons by diffusion, which lowers the average electron energy. The density of high energy electrons in the afterglow drops very rapidly to essentially zero, causing a rapid drop in T_e and the tail of $f_e(\varepsilon)$ to rapidly fall. The density of high energy electrons in the pulsed ICP can be supplemented by a flux of high energy electrons from a remote source. This will then raise the tail of $f_e(\varepsilon)$ and increase T_e. When pulsing the lower ICP, the upper ICP working in tandem can provide the flux of high energy electrons needed to raise the tail of $f_e(\varepsilon)$ and increase T_e in the afterglow of the pulsed lower ICP.

Computed and experimental results for T_e and n_e as a function of time during one pulse cycle for three different tandem ICP operating conditions are shown in Fig. 6.9. In all cases the lower ICP is pulsed with a pulsed-period-averaged (PPA) power of 100 W, pulse repetition frequency (PRF) of 10 kHz and a duty cycle of 20%. The lower ICP power has a 5 μs rise and fall time in the model, while the experimental rise and fall time is believed to be ≈1-2 μs. In one case just the lower ICP is on, the second case has both ICPs on with the top ICP operated in cw mode with 500 W of power and V_B = 0 V, and the third case is the same as the second except V_B

= 60 V. The results are taken near the center of the reactor in the lower ICP region at an equivalent position between the model and experiment. The axial position is at a height of 10.8 cm in the model and a height of 210 mm in the experiment. The radial position is radius = 0.6 cm in the model and radius = 0 cm in the experiment.

When the ICP power is turned on, there is an initial overshoot of T_e, followed by a decay to a quasi-steady state value. At the start of the pulse, the ICP power is initially being dissipated by fewer electrons than at the end of the power pulse due to diffusion losses during the power-off portion of the pulse. Thus T_e increases above its quasi-steady state value until ionization is able to reduce the power dissipation per electron.[18] When the ICP power is turned off, T_e monotonically asymptotes to a minimum value before the start of the next power pulse in the case when just the lower ICP is on. In the cases where the top ICP power is on, T_e increases in the afterglow in the lower ICP from the steady flux of high temperature electrons from the upper ICP. This flux is constant. However, the influence of the flux is only seen in the afterglow. In the afterglow of the pulsed ICP, n_e has decreased enough that the small flux of high energy electrons from the upper ICP can have a non-negligible influence on the average electron energy and thus T_e.

There is generally good agreement between the model and the experimental results for T_e although there are some differences. The overshoot and quasi-steady state values of T_e are slightly higher in the model versus the experiment, ≈1.0 eV difference in overshoot values and ≈0.3 eV in the quasi-steady state values. Also, the effect of applying a boundary electrode bias is reversed in the model and experiment, with the increase in T_e at the end of the pulse (compared to the case with just the lower ICP on) becoming larger with bias in the model and becoming smaller with bias in the experiment. In the model, T_e values at the end of the pulse are ≈0.5 eV,

≈0.8 eV, and ≈1.0 eV for the cases of the lower ICP on only, both ICP on and V_B = 0 V, and both ICP on and V_B = 60 V, respectively. In the experiment, T_e values at the end of the pulse are ≈0.21 eV, ≈0.98 eV, and ≈0.65 eV for the cases of the lower ICP on only, both ICP on and V_B = 0 V, and both ICP on and V_B = 60 V, respectively.

The reason for this discrepancy is unknown at this time, although there may be some error in the way T_e is calculated experimentally when T_e is low. The model is also not a completely accurate representation of the experiment, as will be discussed in the conclusions section. Since the increase in T_e is seen in the afterglow because n_e has decayed to a low enough value that the influence of the electron flux from the upper ICP becomes non-negligible, a source of discrepancy in T_e between the model and experiment may be seen from looking at results for n_e.

There is good agreement between the model and experiment in the overall shape of n_e and in the magnitudes of the peak density at the end of the pulse on period. In the model n_e peaks at ≈4.5×10^{11} cm^{-3}, ≈4.0×10^{11} cm^{-3}, and ≈3.95×10^{11} cm^{-3} for the case of lower ICP on only, both ICP on with V_B = 0 V, and both ICP on with V_B = 60 V, respectively. In the experiment, n_e peaks at ≈4.0×10^{11} cm^{-3}, ≈2.2×10^{11} cm^{-3}, and ≈4.0×10^{11} cm^{-3} for the case of lower ICP on only, both ICP on with V_B = 0 V, and both ICP on with V_B = 60 V, respectively. In the model, n_e decays much faster in the afterglow and to much lower values than in the experiment for all cases. One possible reason for this is that in the experiment the pressure is measured further down in the chamber and the pressure in the lower ICP is actually believed to be larger than 10 mTorr. The pressure in the lower ICP in the experiment is estimated to actually be around 14 mTorr. The higher pressure will slightly reduce the rate of diffusion cooling and most likely lead to somewhat higher densities in the afterglow, although this is not believed to be

a major effect.

In the model, having both ICPs on and V_B = 60 V makes very little change on the n_e profile with time, as compared to the case when V_B = 0 V. In the experiment, n_e at the end of the pulse for the cases when both ICPs are on is a factor of two higher for V_B = 60 V compared to V_B = 0 V. This increased density when the bias is applied may reduce the influence of the flux of high energy electrons from the upper ICP, reducing the amount by which T_e is increased in the afterglow in the experiment.

The dynamics of $f_e(\varepsilon)$ during the pulsed cycle for the same three operating conditions as in Fig. 6.9 are shown in Fig. 6.10. These results are taken at the same position as the plots of T_e and n_e in Fig. 6.9. When just the lower ICP is on, $f_e(\varepsilon)$ show the expected temporal behavior of a pulsed, single source ICP. The dynamics of $f_e(\varepsilon)$ during the pulsed cycle reflects that of T_e. When the lower ICP power pulse initially reaches its peak value at t = 5 μs, $f_e(\varepsilon)$ has a maximally extended tail to an energy of ≈30 eV. The tail of $f_e(\varepsilon)$ then lowers as T_e decays to a quasi-steady state value at t = 24 μs, 1 μs before the end of the pulse on period. After the power pulse is turned off the maximum energy of $f_e(\varepsilon)$ reduces rapidly in the afterglow from t = 30 μs to t = 98 μs, as the high energy electrons are preferentially lost. There is little change in $f_e(\varepsilon)$ in the late afterglow between 50 μs and 98 μs, as only the lower energy electrons are left which take longer to diffuse away. This reflects the slow decrease in T_e observed in the afterglow in Fig. 6.9a.

When the upper ICP is on in cw mode at 500 W in tandem with the pulsed, lower ICP, the tail of $f_e(\varepsilon)$ is raised in the afterglow at t ≥ 50 μs. The tail of $f_e(\varepsilon)$ is raised near the end of the afterglow at t = 98 μs, higher than earlier in the afterglow at t = 50 μs. Near the end of the afterglow at t = 98 μs, the electron density generated from the pulsed ICP decays to an even lower value than at t = 50 μs. This allows the influx of high energy electrons from the upper ICP

to have a greater influence on the average electron energy, raising both the average electron energy and the corresponding T_e.

When V_B = 60 V is applied to the boundary electrode with both ICPs on, the tail of $f_e(\varepsilon)$ is raised in the afterglow at t ≥ 50 μs, even more than when V_B = 0 V. The difference in the lifting of the tail of $f_e(\varepsilon)$ with bias increases the further into the afterglow we observe. Again, the later into the afterglow it is, the lower n_e, and the more influence the influx of high energy electrons from the upper ICP has on the tail of $f_e(\varepsilon)$ and T_e. Late in the afterglow, for V_B = 60 V, the tail of $f_e(\varepsilon)$ is lifted more and T_e increases more compared to V_B = 0 V. This occurs because the flux of high energy electrons from the upper ICP is greater for V_B = 60 V versus V_B = 0 V, for reasons mentioned previously.

Computed and experimental EEPFs just before the lower ICP power pulse is turned off (t = 24 μs) and near the end of the afterglow (t = 98 μs) for three different operating conditions are shown in Fig. 6.11. The results are taken near the center of the reactor in the lower ICP region at an equivalent position between the model and experiment. The axial position is at a height of 10.8 cm in the model and a height of 210 mm in the experiment. The radial position is at a radius of 0.6 cm in the model and a radius of 0 cm in the experiment. This is the same position where $f_e(\varepsilon)$ is computed in Fig. 6.10. The same trends are observed in the model and experiment and there is good agreement in both the shape and magnitude of the EEPFs, except for the EEPF at t = 98 μs, when only the lower ICP is on. In this case, the peak density is much lower in the model, which is largely due to the much lower value of n_e in the model at t = 98 μs, when just the lower ICP is on. Looking at the EEPFs for t = 24 μs under all three conditions, it is observed that the upper ICP has little effect on the EEPF when the bottom ICP is on. This matches what is observed in the cases when both ICPs are operated in cw mode. In the afterglow at t = 98 μs,

having the upper ICP on, with or without an applied bias on the boundary electrode, has a significant effect on the EEPF. Having the upper ICP on creates a flux of high energy electrons from the upper ICP to the lower ICP, which raises the tail of the EEPF in the afterglow and causes T_e to increase in the afterglow as well.

6.4 Concluding Remarks

In conclusion, results from computational and experimental investigations suggest that the use of a tandem-ICP with a boundary electrode can provide for some control of $f_e(\varepsilon)$ in a lower, primary ICP through the flux of electrons from an upper, secondary ICP. The flux of electrons from the secondary ICP is not large enough to significantly modify $f_e(\varepsilon)$ when both ICPs are on, but can modify $f_e(\varepsilon)$ in the afterglow when the primary ICP is pulsed. The effect of the influx of electrons from the upper ICP to the lower ICP is to raise the tail of $f_e(\varepsilon)$ in the afterglow, which causes T_e to increase in the afterglow. This was observed both in the model and experimentally.

There are some discrepancies between the model and the experimental data. Some of these discrepancies could be the result of measurement error as well as the inability to exactly model some key parts of the system. For example, in the experiment a rectangular mesh grid is used with a spacing of 2.3 mm. The wires of the grid are in the 100s of μm range. The cylindrically symmetric nature of the model, as well as the length scales of the model, prevent an exact representation of the grid in the model. The range in scale lengths for different parts of the experimental setup does not allow for the mesh spacing to be accurately resolved and as such the mesh spacing is 7.8 mm in the model as opposed to 2.3 mm in the experiment. Since the model is cylindrically symmetric, a rectangular grid cannot be modeled. In fact, the actual wires of the grid cannot be modeled and as such, mesh points spaced 7.8 mm apart are set to have fixed 0 V

potential representing the grounded grid. This produces an effective grid made up of concentric rings.

The position of the gas inlet could also not be accurately modeled due to the cylindrically symmetric nature of the model. In the experiment, the gas inlet is on one side of the boundary electrode, while in the model the gas inlet comes in from the top. These are just some of the possible sources of discrepancy between the model and experiment; however, overall there is good agreement between the model and experiment in both trends and magnitudes.

6.5 Figures

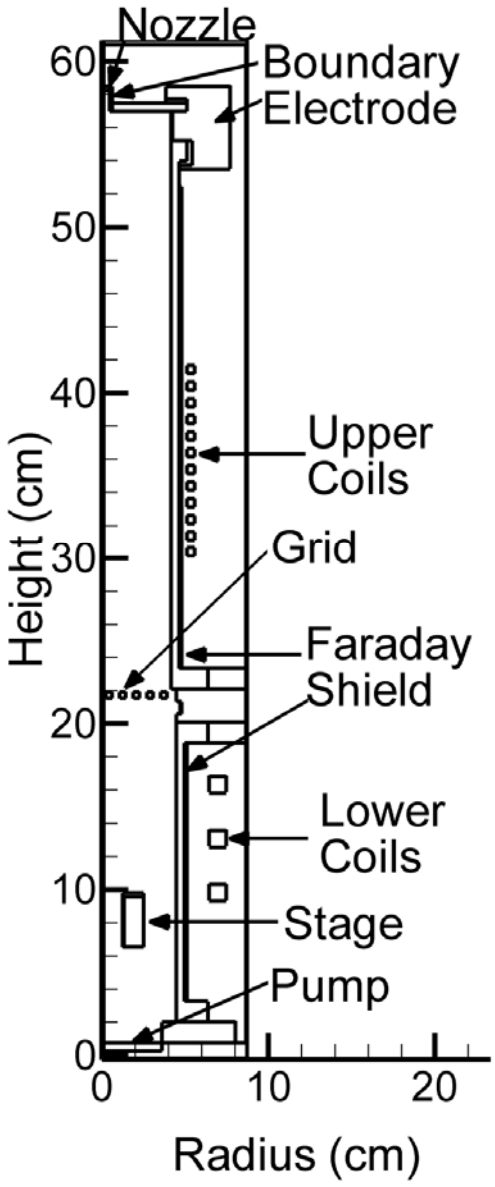

Figure 6.1 Schematic of the model Tandem Inductively Coupled Plasma (T-ICP) reactor.

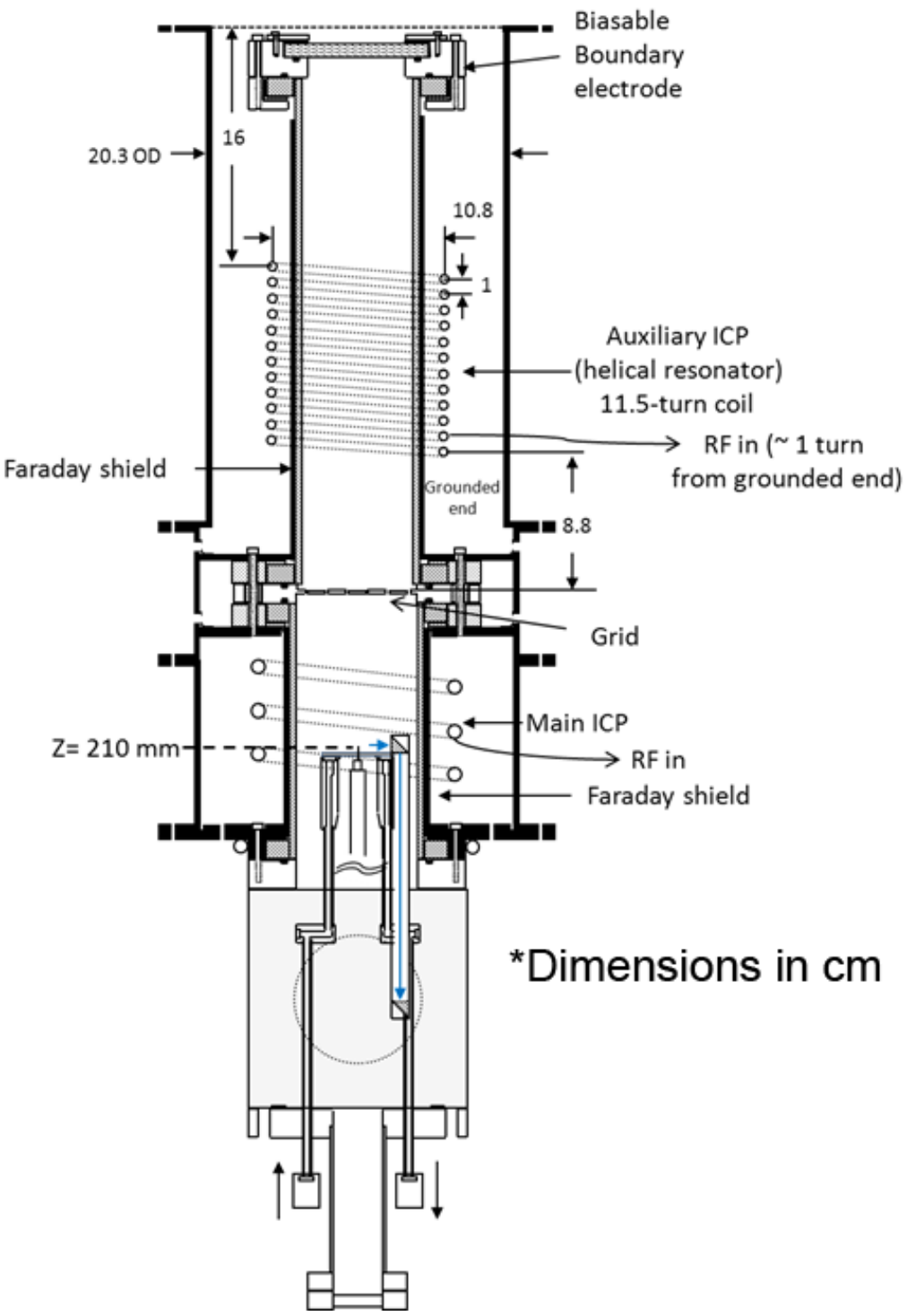

Figure 6.2 Schematic of the experimental Tandem Inductively Coupled Plasma (T-ICP) reactor.

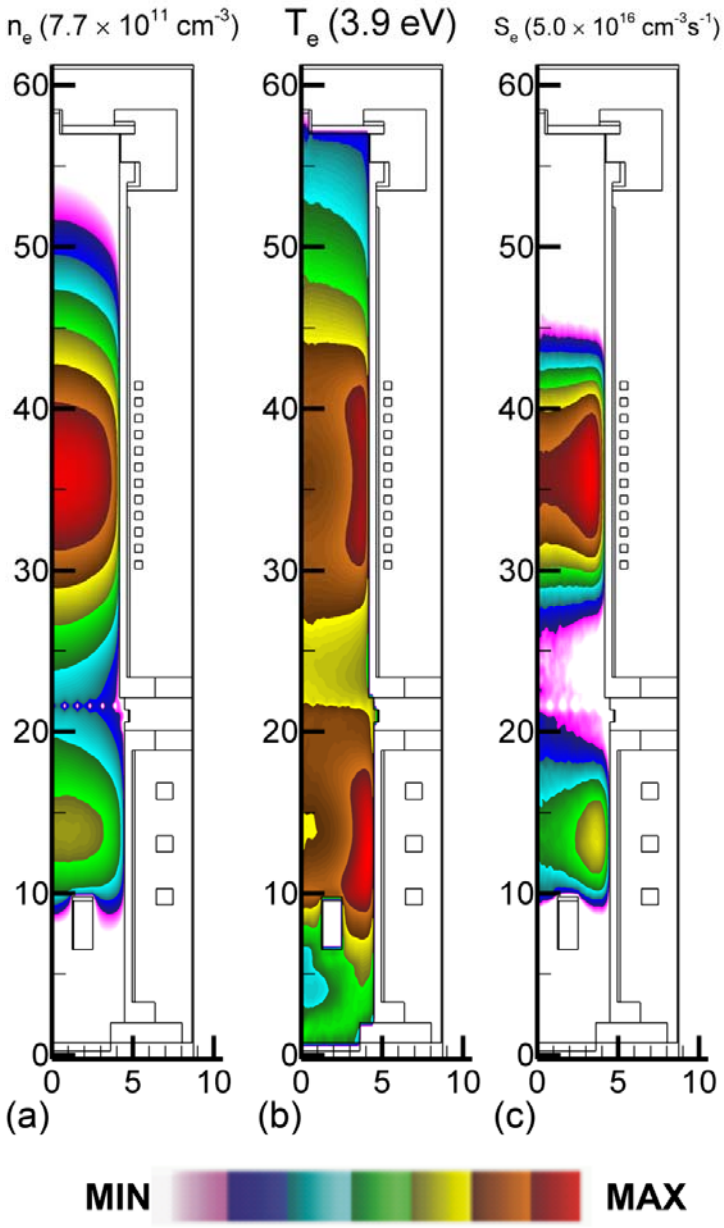

Figure 6.3 Electron density, electron temperature, and electron source function when both ICPs are on. Plasma conditions are argon, Upper ICP: 500 W (cw), Lower ICP: 90 W (cw), V_B = 0 V, 10 mTorr, and 80 sccm. (a) Electron density. (b) Electron temperature. (c) Electron source function.

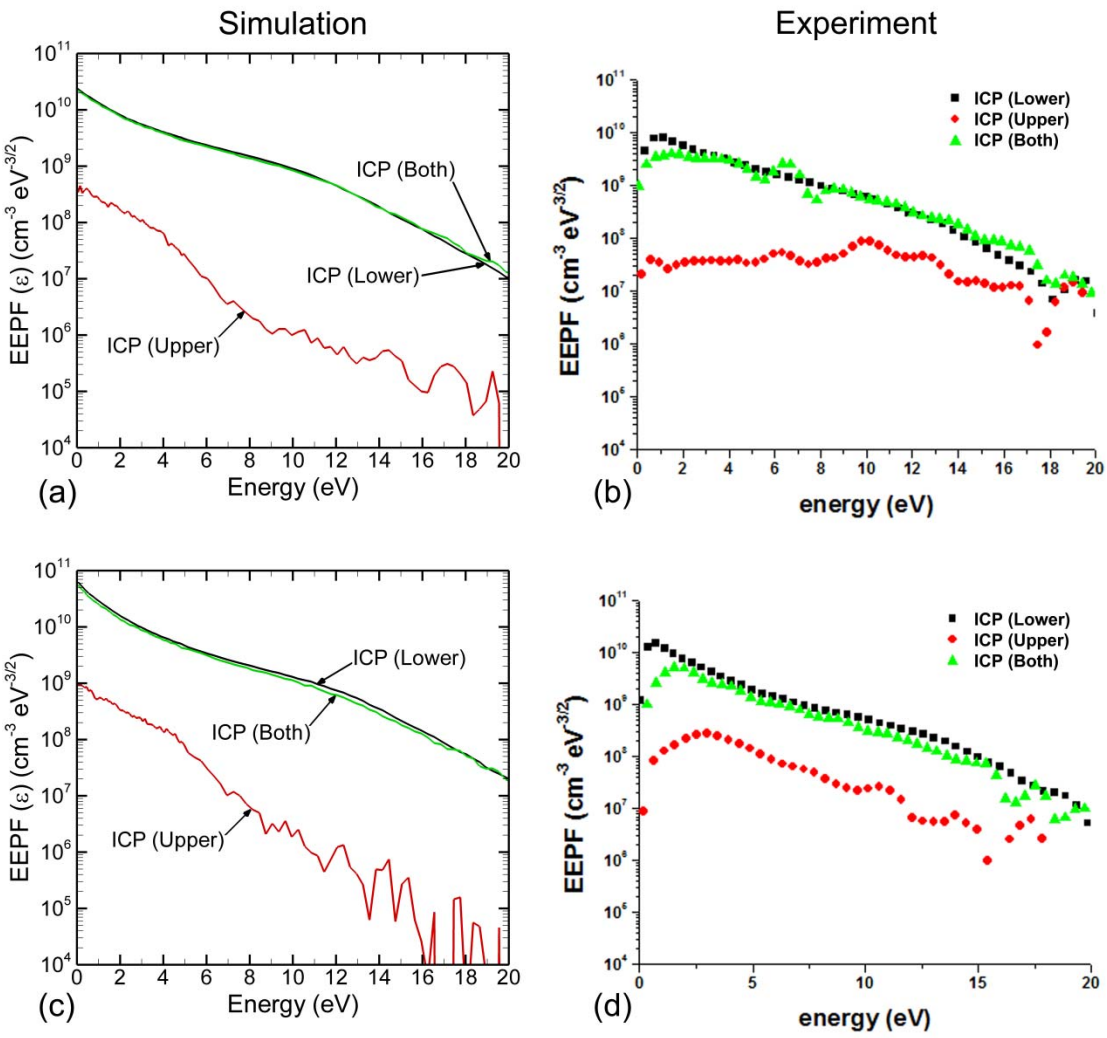

Figure 6.4 EEPFs taken at two positions for three configurations. The three configurations are: lower ICP on only at 90 W (cw); both ICP on with 500 W (cw) on Upper ICP, 90 W (cw) on lower ICP and V_B = 0 V; and both ICP on with 500 W (cw) on Upper ICP, 90 W (cw) on lower ICP and V_B = 60 V. Other plasma conditions are argon, 10 mTorr, and 80 sccm. (a) Simulated EEPFs at (r,z) = (0.6 cm, 10.8 cm). (b) Experimental EEPFs at r = 0 cm and at equivalent height as in (a). (c) Simulated EEPFs at (r,z) = (0.6 cm, 14.8 cm). (d) Experimental EEPFs at r = 0 cm and at equivalent height as in (c).

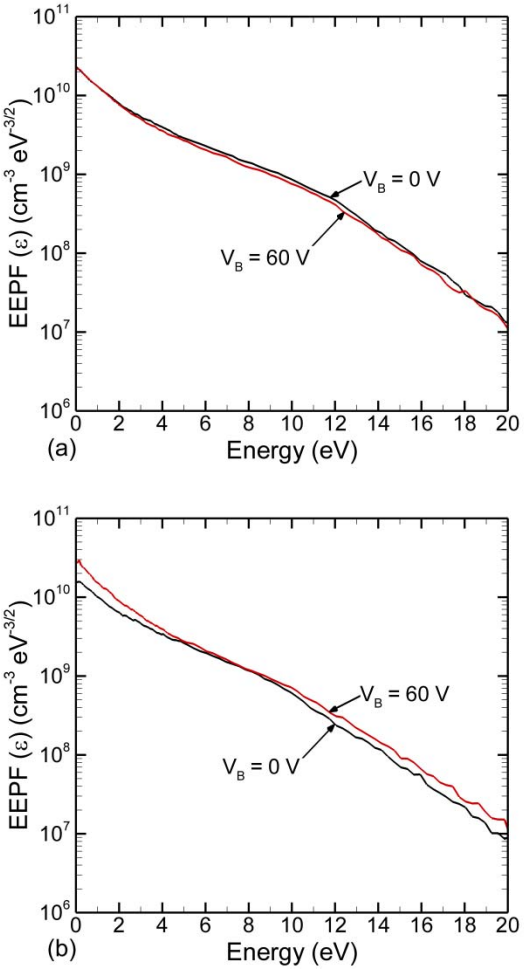

Figure 6.5 Simulated EEPFs taken at two positions for the configurations of: both ICP on with 500 W (cw) on Upper ICP, 90 W (cw) on lower ICP and V_B = 0 V; and both ICP on with 500 W (cw) on Upper ICP, 90 W (cw) on lower ICP and V_B = 60 V. Other plasma conditions are argon, 10 mTorr, and 80 sccm. (a) (r,z) = (0.6 cm, 10.8 cm). (b) (r,z) = (0.6 cm, 14.8 cm).

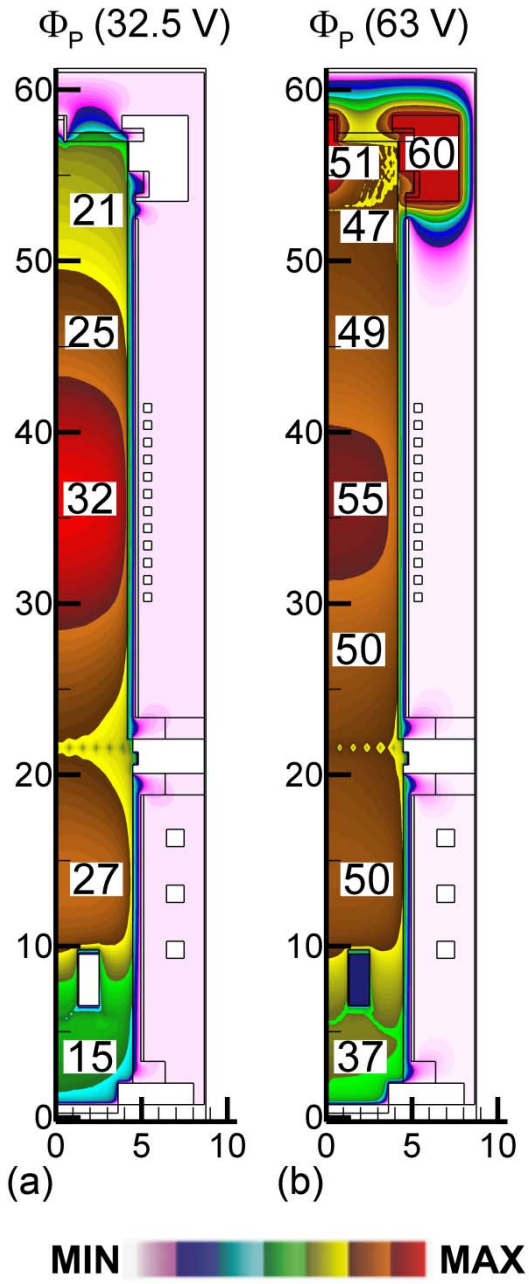

Figure 6.6 Plasma potential for two boundary electrode bias conditions when both ICPs are on. Plasma conditions are argon, Upper ICP: 500 W (cw), Lower ICP: 90 W (cw), 10 mTorr, and 80 sccm. (a) $V_B = 0$ V. (b) $V_B = 60$ V.

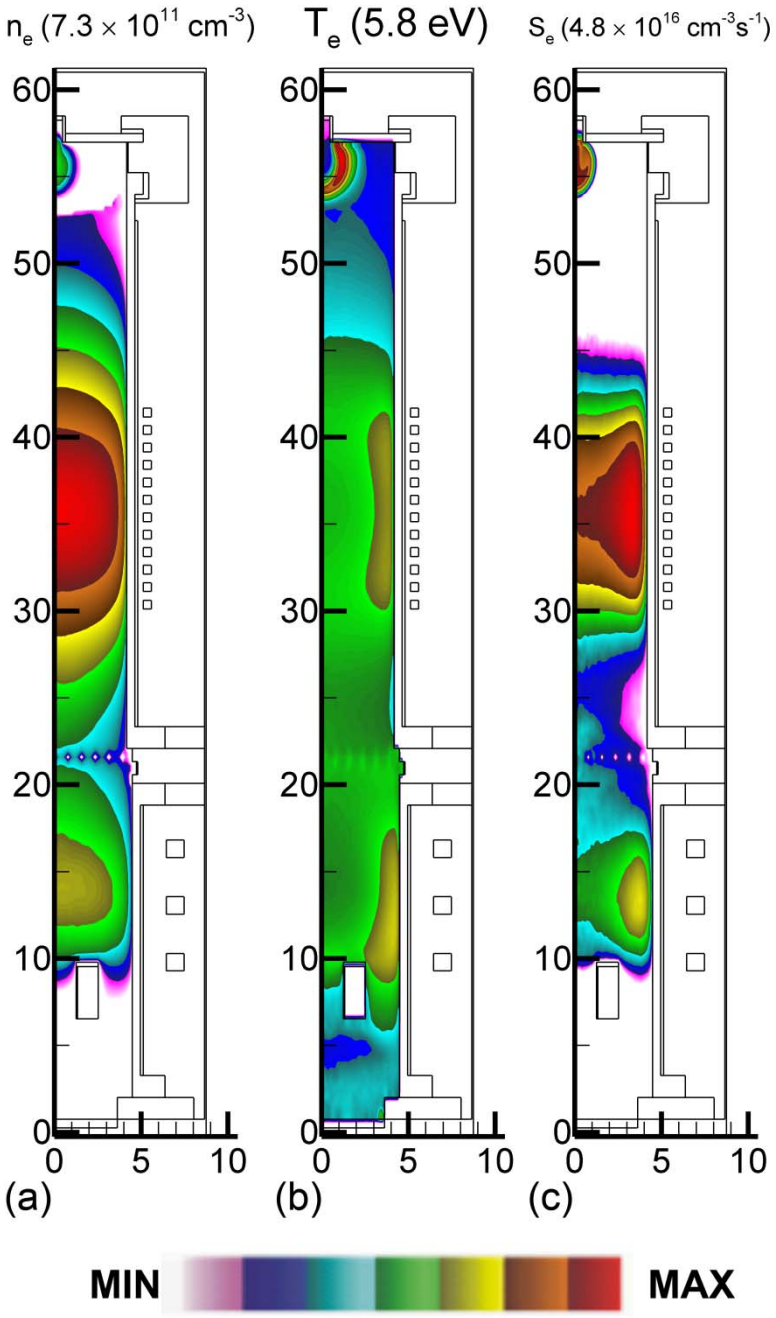

Figure 6.7 Electron density, electron temperature, and electron source function when both ICPs are on. Plasma conditions are argon, Upper ICP: 500 W (cw), Lower ICP: 90 W (cw), V_B = 60 V, 10 mTorr, and 80 sccm. (a) Electron density. (b) Electron temperature. (c) Electron source function.

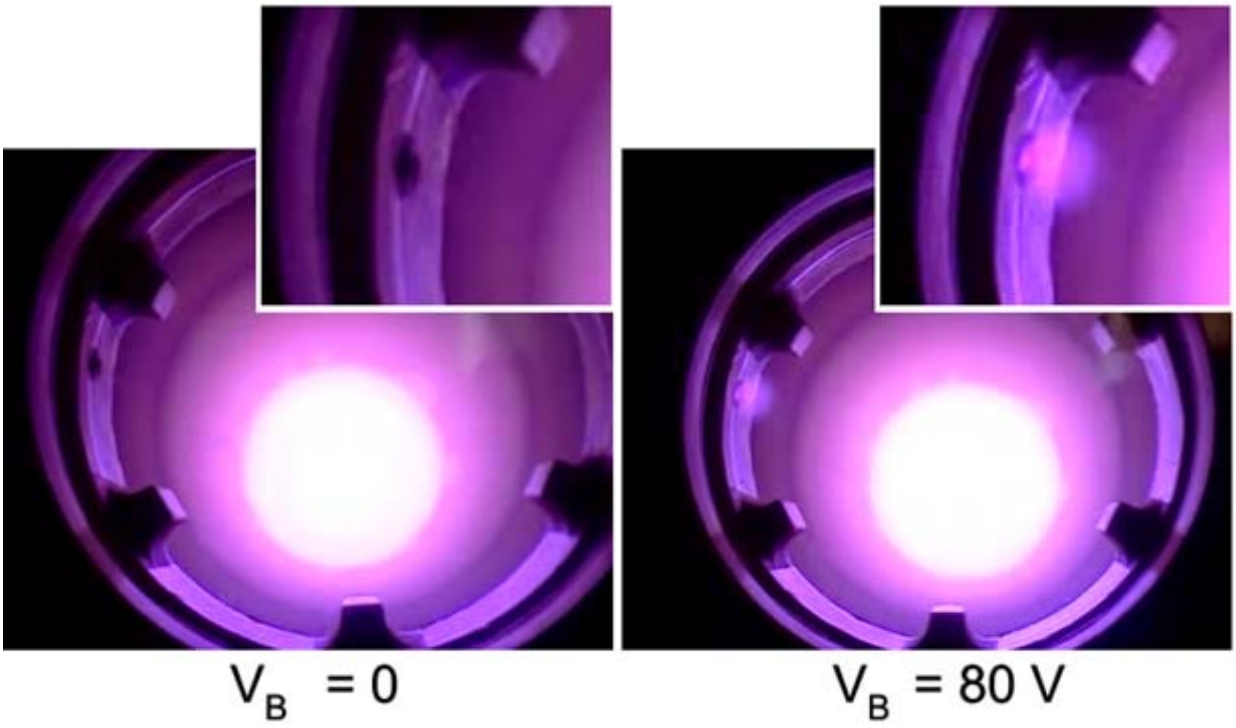

Figure 6.8 Top down view into T-ICP through dielectric window at the top of the reactor for two boundary electrode bias voltages. Insets show zoomed in view of gas inlet in the side of the boundary electrode. Local discharge develops at the gas inlet for large positive values of V_B.

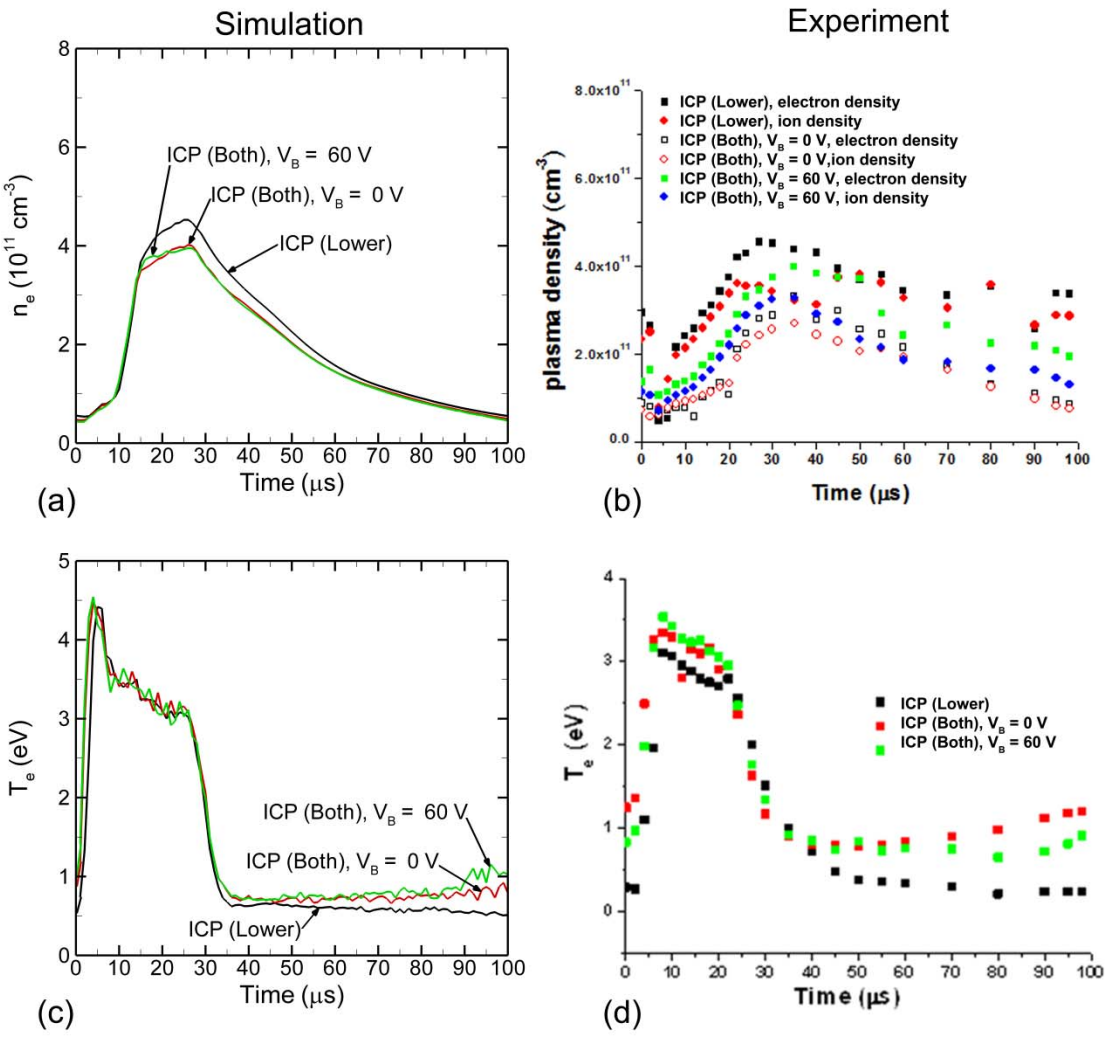

Figure 6.9 Simulated and experimental plasma parameters (T_e and n_e) versus time during one pulse of the lower ICP power, taken at (r,z) = (0.6 cm, 10.8 cm) for three configurations. The three configurations are: lower ICP on only pulsed at 100 W pulse-period-averaged (PPA) power, pulse repetition frequency of 10 kHz, and duty cycle = 20%; both ICP on with 500 W (cw) on Upper ICP, 100 W PPA power on lower ICP and V_B = 0 V; and both ICP on with 500 W (cw) on Upper ICP, 100 W PPA power on lower ICP and V_B = 60 V. Other plasma conditions are argon, 10 mTorr, and 80 sccm. (a) Simulated electron density. (b) Experimental electron density. (c) Simulated electron temperature (d) Experimental electron temperature.

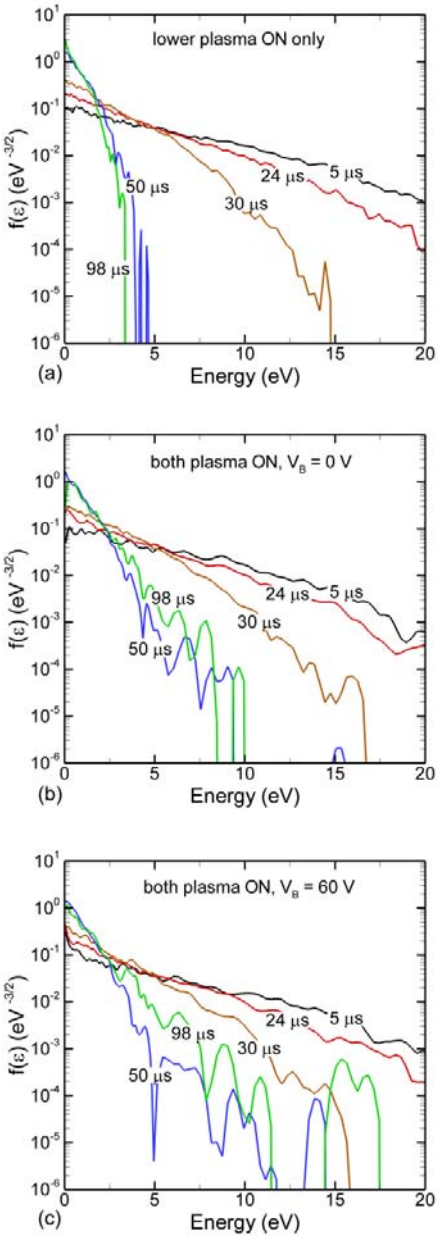

Figure 6.10 $f_e(\varepsilon)$ at different times during the lower ICP pulse period, taken at (r,z) = (0.6 cm, 10.8 cm) for three configurations. Plasma conditions are argon, 10 mTorr, and 80 sccm. (a) Lower ICP on only pulsed at 100 W pulse-period-averaged (PPA) power, pulse repetition frequency of 10 kHz, and duty cycle = 20%. (b) Both ICP on with 500 W (cw) on Upper ICP, lower ICP pulsed at 100 W PPA power, PRF = 10 kHz, duty cycle = 20%, and V_B = 0 V. (c) Both ICP on with 500 W (cw) on Upper ICP, lower ICP pulsed at 100 W PPA power, PRF = 10 kHz, duty cycle = 20%, and V_B = 60 V.

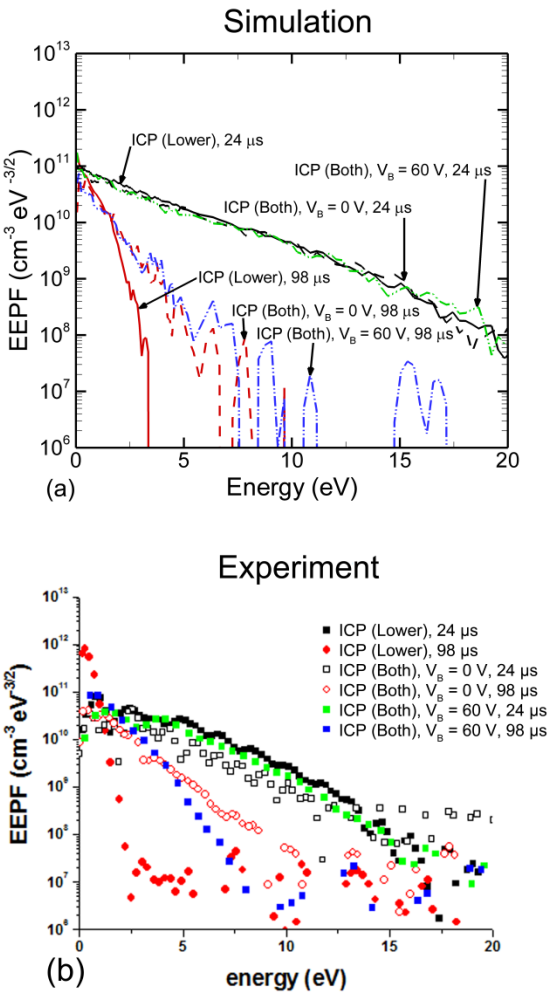

Figure 6.11 Simulated and experimental EEPFs at two times during the lower ICP pulse period, taken at (r,z) = (0.6 cm, 10.8 cm) for three configurations. The three configurations are: Lower ICP on only pulsed at 100 W pulse-period-averaged (PPA) power, pulse repetition frequency of 10 kHz, and duty cycle = 20%; Both ICP on with 500 W (cw) on Upper ICP, lower ICP pulsed at 100 W PPA power, PRF = 10 kHz, duty cycle = 20%, and V_B = 0 V; Both ICP on with 500 W (cw) on Upper ICP, lower ICP pulsed at 100 W PPA power, PRF = 10 kHz, duty cycle = 20%, and V_B = 60 V. Other plasma conditions are argon, 10 mTorr, and 80 sccm. The two time points are near the end of the activeglow period (t = 24 μs) and near the end of the afterglow period (t = 98 μs). (a) Simulation. (b) Experiment.

6.6 References

1. V. A. Godyak, Phys. Plasmas **20**, 101611 (2013).
2. D. J. Economou, Thin Solid Films, **365**, 348 (2000).
3. S. Banna, A. Agarwal, G. Cunge, M. Darnon, E. Pargon, and O. Joubert, J. Vac. Sci. Technol. A **30**, 040801 (2012).
4. U. Kortshagen, I. Pukropski, and M. Zethoff, J. Appl. Phys. **76**, 2048 (1994).
5. H. Singh and D. B. Graves, J. Appl. Phys. **87**, 4098 (2000).
6. T. Kimura and K. Ohe, J. Appl. Phys. **89**, 4240 (2001).
7. V. A. Godyak, R. B. Piejak, and B. M. Alexandrovich, Plasma Sources Sci. Technol. **11**, 525 (2002).
8. M. V. Malyshev and V. M. Donnelly, Plasma Sources Sci. Technol. **9**, 353 (2000).
9. A. Maresca, K. Orlov, and U. Kortshagen, Phys. Rev. E **65**, 056405 (2002)
10. V. A. Godyak, "Nonequilibrium EEDF in Gas Discharge Plasmas", IEEE Trans. Plasma Sci. **34**, 755 (2006).
11. K. Kato, S. Iizuka, and N. Sato, Appl. Phys. Lett. **65,** 816 (1994).
12. J. I. Hong, S. H. Seo, S. S. Kim, N. S. Yoon, C. S. Chang, and H. Y. Chang, Phys. Plasmas **6,** 1017 (1999).
13. F. A. Haas, A. Goodyear, and N. S. J. Braithwaite, Plasma Sources Sci. Technol. **7**, 471 (1998).
14. F. A. Haas and N. S. J. Braithwaite, Appl. Phys. Lett. **74**, 338 (1999).
15. S. Uhm, K.-H. Lee, H. Y. Chang, and C. W. Chung, Phys. Plasmas **11,** 4830 (2004).
16. M. A. Lieberman and A. J. Lichtenberg, Principles of Plasma Discharges and Materials Processing (John Wiley & Sons, Inc., Hoboken, NJ, 2005).
17. V. A. Godyak, R. B. Piejak, and B. M. Alexandrovich, Plasma Sources Sci. Technol. **11**, 525 (2002).
18. S. Ashida, M. R. Shim and M. A. Lieberman, J. Vac. Sci. Technol. A 14, 391 (1996).

Chapter 7 Conclusion and Future Work

7.1 Research Summary

In this thesis, computational investigations into the use of pulsed power and dc biases to control electron and ion energy distributions (EEDs and IEDs) in inductively coupled plasmas (ICPs) were discussed. Results from these investigations were obtained using a 2-D hybrid modeling platform known as the Hybrid Plasma Equipment Model or HPEM. The results of this work can ideally be used for advanced plasma etching techniques in order to control process parameters such as electron temperature, dissociation rate, neutral to ion flux ratio, and ion energy versus ion flux needed for processes below the 22 nm technology node.[1]

The effect of pulsed power on EEDs and source functions in a simple planar ICP reactor was investigated. Source functions were investigated for three plasma species generated through "low" (≈1 eV), "mid" (≈6 eV), and "high" (≈16 eV) threshold energy processes. Duty cycle was found not to have a significant impact on the time averaged source functions, changing by a factor of ≈2 between duty cycles of 10% and 50%. This was also reflected in the computed time averaged EEDs which also saw little change with duty cycle except for a slight lifting of the EED tail as duty cycle increased. The tail of the time averaged EED comes from the high energy electrons generated in the activeglow period of the pulse, which becomes an increasing fraction of the pulse period as duty cycle increases. Increasing pressure had a more significant effect on both the EED and the source functions. Increased collision rates at higher pressures reduced the electron temperature during the activeglow period and lowered the tail of the time averaged EED. Source functions for the low threshold energy process increased more with pressure than mid

threshold energy process, which increased more than the high threshold energy process. If the threshold energy is high enough, and the lowering of the EED tail is large enough, there may be no increase or even a decrease in the time averaged source function of that process with pressure.

The trends seen in the EED and source functions as a function of duty cycle and pressure, are seen at pulse-period-average powers of 75 W and 300 W. The results shown in chapter 3 are for 300 W of power. The EED shapes and trends are the same for 75 W, except the tail of the EED is lower than at 300 W. The lower tail of the EED at 75 W, particularly in the afterglow allowed for increased modulation of the source functions of $N_2(v = 1)$ and $N_2(A)$ over the pulse at 5 mTorr. There was also found to be a significant dependence of height on the time averaged EEDs at higher pressures where collisions significantly reduce the electron mean free path.

Overall the main effect of pulsing of the ICP power on the EED is the modulation of the EED tail. Source functions are also modulated during the pulse, with the amount of modulation increasing as the threshold energy for the process increases. From a time-averaged standpoint, pulsing does not seem to have a significant effect on EEDs and source functions; however, due to the modulation in source functions and the tail of the EED during the pulse, the fluxes of reactive species to the surface of a substrate at a given time can be modulated. This modulation in flux would most likely depend on threshold energy, the lifetime and diffusion rate of the plasma species, and the distance between the substrate and the source.

The effect on IEDs of applying a dc bias on a boundary electrode in an Ar cylindrical ICP system was investigated. The system was modeled after the experimental system of Professor Demetre Economou and Professor Vincent Donnelly at the University of Houston. The applied dc bias had the effect of raising the plasma potential in the ICP without affecting other plasma parameters such as electron temperature and density. This allowed shifting of the IED in energy

without affecting the shape. This only holds true for cases when the dc power being deposited in the system is much less than the ICP power and the plasma density is greater than what it would be for a dc discharge with a self-sustaining E/N equal to the E/N from the dc bias. It was discovered that for electropositive plasma, only positive bias could significantly shift the plasma potential and thus the IED. The plasma potential and the IED were shifted to higher values with positive bias, while negative bias only resulted in a small, capped downshift in the plasma potential and IED. This is due to the requirement of the electropositive plasma to remain positive with respect to ground to trap thermal electrons from escaping the plasma.

Overall, the effect of applying a positive dc bias on a boundary electrode in contact with the plasma was to increase the plasma potential by approximately the dc bias value, shifting the IED during the applied bias time to higher energy. When a pulsed dc bias is applied in the afterglow of the pulsed ICP, the dc bias shifted the narrow afterglow IED peak to be centered in energy at approximately the dc bias voltage. Very precise control of the energy position of this narrow peak becomes possible simply through control of the dc bias voltage. For the time averaged IED, the ratio of the maxima of the IED could be adjusted by the length of time the dc bias is applied.

The use of dc biases to selectively control IEDs in plasmas with multiple ionic species based on their mass ratios was also investigated in a simple planar ICP system. Sheath transit times for ions differ based on their mass. Heavier ions are accelerated slower than lighter ions and so take longer to cross the sheath and reach the substrate. This can result in different IEDs for different ions based on their mass, especially in plasmas with rf biases where the sheath width and potential is constantly being modulated. This effect is controlled through the use of pulsed dc biases. Using a pulsed dc bias, the duration of the dc bias time was controlled to

control the ratio of dc bias time to sheath transit time for the ions. A dc bias applied for a length of time longer than the sheath transit time of the lighter ion but shorter than the transit time of the heavier ion caused the IED peak during the bias period for the heavier ions to be centered at lower energies than the peaks for lighter ions. Since the difference in sheath transit time is a function of the mass ratio, gas chemistries containing ions with large differences in mass were investigated, in this case Ar/H_2 and Xe/H_2. The energy position of the high energy peak of the heavier ions could be downshifted by a significant amount compared to the position of the high energy peak of the lighter ions, depending on the mass ratio between them and the bias duration length. The transit times for the ions, even heavy ones like Xe are very short. Therefore, to get significant difference in the IEDs for light and heavy ions, bias durations need to be very short (100s of ns) and very precise, especially in systems where the mass difference between ions is not that large. Pulsed dc bias duration of 100s of ns are possible today; however, the pulse repetition frequencies needed to get a significant time averaged flux of ions at the applied dc bias voltage are not as easily achievable. This may make this technique impractical for industrial applications.

Finally, the ability to control the EED in a lower ICP chamber using a tandem, upper ICP source separated from the lower ICP by a grounded mesh grid and dc biases on a boundary electrode at the top of the system was investigated. The system was modeled after the experimental system of Professor Demetre Economou and Professor Vincent Donnelly at the University of Houston. When both ICPs were operated in cw mode, the upper ICP had almost no effect on the EED in the lower ICP region. It was only when the lower ICP was pulsed that the influx of high energy electrons from the upper ICP could raise the tail of the EED in the pulse afterglow. This caused an increase in electron temperature in the afterglow as well.

Applying a large positive dc bias on the boundary electrode in the system created a local ionization region at the gas inlet. In the model, this had the effect of providing an additional source of high energy electrons from the upper ICP region to the lower region. This raised the tail of the EED in the afterglow and increased the electron temperature in the afterglow more than without bias. The opposite effect with bias was seen experimentally, with the tail of the EED and the electron temperature not being raised as much when bias was applied as compared to when no bias was applied. This discrepancy is still being investigated but could be some combination of measurement error and limitations in the model.

7.2 Validation and Impact

When trying to decide how much to trust the results of a computational model and how applicable the results are to real world situations, a question that often comes up is how the model is validated. This is a very obvious question as models can generally never capture every aspect of an experiment. In some cases, this may not be an issue as experimental results are dominantly the result of certain key physics, which can be modeled through well-established methods. This may also not be an issue if the goal of the model is to capture trends observed in the experiment and not necessarily duplicate the results exactly, which was the purpose of this work. The model used to obtain the results of this thesis, the HPEM, is a well-established modeling platform that has been used extensively in both academic and industrial settings for just such a purpose and has an excellent track record at accurately capturing experimental physics.

Fortunately, in terms of validation, half of the work of this thesis is based on modeling of actual experimental systems found in the research group of Professor Demetre Economou and Professor Vincent Donnelly at the University of Houston. Several comparisons to experiments

have been made and in general the model has been validated by good agreement between the model and the experiment in both trends and in actual magnitudes.[2] In fact, results of the model were used to discover a source of measurement error in the measured IEDs in the single source boundary electrode ICP system. The retarding field energy analyzer (RFEA) being used to obtain the IEDs was found to have a low collection efficiency of low energy ions, believed to be caused by the large negative bias on one of the grids in the RFEA. The grids may also prevent ions traveling at large angles with respect to the normal of the collection plate, of which low energy ions will represent a large fraction, from reaching the collection plate at the bottom of the RFEA. This caused the IED at low energies to be artificially reduced. The effect of reduced collection angle in the model on the IED at low energies was investigated and this same reduction in the IED was observed. These low energy ions typically have a broad angular distribution and small angular collection efficiency reduces the ability to see the true IED shape at these energies.

Comparing the experimental and calculated IEDs did reveal a source of discrepancy in the model pertaining to the determination of the ion momentum cross section. The way the ion momentum cross section is currently determined for ion transport may not accurately capture the true experimental cross sections as a function of ion energy. In the work on investigating the effect of pulsing on EEDs and source functions in a simple ICP reactor, some comparisons were made to the experimental work of Singh and Graves [3], which showed agreement in the observed trends.

The investigations of this thesis were generally designed to model trends and develop insights and scaling laws that could be used to improve plasma processing applications such as plasma etching. It is believed the results of this thesis successfully achieve this goal. For

example, the results of this thesis on the effects of pulsing on EEDs and source functions can provide insights into how the threshold energy of a process has a significant impact on the ability of pulsing to affect the reaction rate of that process. It also indicates that time averaged values for plasma parameters and EEDs may not be the most appropriate method for determining the effect of pulsing on a particular etch process as there is not significant change over a large duty cycle range. The temporal behavior of the plasma and its effect on these parameters may also need to be taken into account to accurately capture observed etch effects.

The ability to create a narrow IED centered at essentially arbitrary energy can have large implications on plasma etch performance characteristics such as etch selectivity and plasma induced damage. By tuning the IED to be between the etch threshold energies of the material to be etched and the etch stop layer, an essentially infinite selectivity can be achieved. The IED could also be made to have a high energy peak for the majority of the etch, for a faster etch rate, and then the ion energy could be decreased for a slower etch with less plasma induced damage. Using the dc bias to set the ion energy also allows the ion energy and the ion flux, determined largely by the plasma density, to largely be controlled independently. This additional control of the ion flux allows additional control of the neutral versus ion flux as well, which could be used to better control the rate of etching versus deposition on a wafer.

7.3 Future Work

The use of pulsed power and dc biases, both separately and together, for control of EEDs and IEDs has been discussed. There are several ways the work of this thesis could be improved upon in the future, especially when considering the desire to apply these techniques to industrial applications.

7.3.1 Use of common etching gases

Most of the results of this work were obtained in pure argon. This is a good gas for testing and validation purposes; however most industrial etching applications will use more complex gas chemistries. In the future, $Ar/CF_4/O_2$, which is used in the etching of silicon dioxide, could be investigated. Whether the same trends are observed in this gas mixture would help to establish the viability of this research for industrial processes.

7.3.2 Perform etch profile simulations

Since the goal of this work is to improve plasma materials processing applications and in particular plasma etching applications, etch profile simulations would help to visualize possible improvements, or problems, caused by the proposed control methods. This goes hand in hand with using common etching gasses in the model to get a more accurate idea of how this research translates to real industrial applications. Etch profile simulations would also allow us to compare the simulated etch profiles to actual published results as a source of validation.

7.3.3 Investigate effect of pulsing of the upper ICP and boundary electrode in T-ICP

The tandem-ICP was investigated for the conditions of both ICPs operated in cw mode or the lower ICP pulsed, with the upper ICP in cw mode. The boundary electrode bias was either off or on as well. Both ICPs and the dc bias on the boundary electrode can be pulsed independently. This allows for many potential combinations of PRFs and duty cycles to be explored as well as potential timing schemes between the ICPs and the dc bias. This allows for a large parameter space in which to potentially control the EED, far more than could be achieved with just a pulsed single source system.

7.4 References

1. S. Banna, A. Agarwal, G. Cunge, M. Darnon, E. Pargon, and O. Joubert, J. Vac. Sci. Technol. A **30**, 040801 (2012).

2. M. D. Logue, H. Shin, W. Zhu, L. Xu, V. M. Donnelly, D. J. Economou, and M. J. Kushner, Plasma Sources Sci. Technol. **21**, 065009 (2012).

3. H. Singh and D. B. Graves, J. Appl. Phys. **87**, 4098 (2000).